Ship-induced waves interacting with floating membranes

A three-dimensional hydroelastic analysis

MSc Thesis

Khalil Akchikchi

Delft University of Technology

TU Delft

Ship-induced waves interacting with floating membranes

A three-dimensional hydroelastic analysis

submitted by

Khalil Akchikchi

in fulfilment of the requirements for the degree of Master of Science
at the Delft University of Technology,
to be defended publicly on Tuesday December 17, 2024 at 3:00 PM.

Student number:	5421802	
Thesis committee:	Dr. ir. J.O. Colomés Gené (chair),	Offshore Engineering, TU Delft
	Dr. ir. S. Agarwal,	Offshore Engineering, TU Delft
	Dr. ir. R.J. Labeur,	Hydraulic Engineering, TU Delft
Faculty:	Faculty of Civil Engineering and Geosciences	

TU Delft

Acknowledgments

This report marks the completion of my Master's program in Hydraulic and Offshore Structures at the Faculty of Civil Engineering and Geosciences, Delft University of Technology. Reflecting on my entire academic journey, I can say it has been a period of hard work, dedication to overcoming challenges, and personal growth. I am truly pleased to have reached this milestone by completing my thesis, entitled 'Ship-induced waves interacting with floating membranes', and I hope it proves valuable to others. However, before I delve into the findings of my research, I would like to express my gratitude to those who have played an instrumental role in this journey.

First and foremost, I would like to thank Allah for everything I have been blessed with. It is He who bestows upon us joy, strength, motivation, and the ability to think critically about complex matters. All praise be to Allah, the Lord of the Universe.

The first person I wish to thank is the chair of my graduation committee, Oriol Colomés Gené. I greatly enjoyed his finite element modelling and fluid-structure interaction classes during my Master's studies, which inspired me to approach him about the possibility of conducting my thesis within his research group. This ultimately led to the development of this rewarding project. I would also like to express my gratitude to Robert Jan Labeur for his excellent feedback throughout the process, especially for the qualitative discussions we had on analysing intermediate results step-by-step to gradually solve complex problems. My thanks also go to Rui Gomes from Blue21, who attended all of my progress meetings and asked insightful questions that kept me sharp. Finally, I would like to thank my daily supervisor Shagun Agarwal, for his large involvement in this project. His continuous guidance, multidisciplinary knowledge, and genuine interest in this research have been invaluable to my learning experience. I greatly appreciate the time he dedicated to me whenever I had questions or wanted to discuss any aspect of my work.

I would also like to thank all my friends during my studies, whose presence made my time at university enjoyable. Last but not least, I express my deepest gratitude to my parents and sister for their boundless encouragement, care, and unwavering belief in me. Without their support, reaching this stage would not have been possible. I can't thank you enough for everything.

Khalil Akchikchi
Amsterdam, December 2024

Abstract

Thin and large floating structures are increasingly used for a variety of applications, such as floating solar platforms, aquaculture, storage facilities, and even housing. For example, in the Netherlands, where thin plate-shaped floating solar platforms are being deployed in near-shore regions due to their benefits, such as uninterrupted solar irradiance and land conservation. With these deployments, it becomes essential to assess the risk posed to these structures by wave forcing in near-shore environments. Due to the large size of these flexible structures, the potential large impact of long ship-generated waves can be a key scenario of concern.

This thesis explores this scenario using a hybrid model, which couples a weakly nonlinear 2D finite element-based Boussinesq wave-generation model (FEBOUSS) with a 3D linear monolithic fluid-structure interaction (FSI) model. A key contribution of this work is the implementation of a novel, one-way partitioned fluid-fluid coupling algorithm, which efficiently transfers wave-information from the FEBOUSS model to the FSI model. The coupling is achieved by (1) enforcing the normal wave particle velocity from FEBOUSS as a boundary condition at the vertical inlet of the FSI model, and (2) using a damping zone that not only absorbs reflected waves from the membrane but also gradually enforces wave-elevation and normal wave particle velocity at a subsection of the free surface boundary of the FSI model. The accuracy of the coupling algorithm can be adjusted by refining the partition of feeding particles in the overlapping zone while simultaneously controlling the length of the damping zone. This approach ensures both computational efficiency, in terms of total simulation time and data storage requirements, as well as high physical accuracy at the coupling interface. The scenario of ship-induced waves entering a narrow harbour housing a floating structure is demonstrated, focusing on how the velocity of the moving vessel, represented non-dimensionally by the depth-Froude number, influences the hydroelastic response of the membrane. The analysis revealed that for all tested depth-Froude numbers, the membrane initially follows the long ship-induced waves, with subsequent responses that may be either (significantly) amplified or dampened with respect to the incoming waves, depending on the specific case under consideration.

The work presented in this thesis makes a significant contribution to offshore engineering literature by introducing a novel fluid-fluid coupling algorithm that can be extended to even more complex scenarios. Both the FEBOUSS wave-generation model and the FSI model are highly versatile, making them suitable for studying a broad range of fluid-structure interaction problems. Future research could explore the effects of variable bathymetry, irregularly shaped floating structures, and other relevant factors, expanding the scope of this study to include a broader range of physical phenomena.

Contents

List of Figures

List of Tables

Nomenclature

List of abbreviations

Abbreviation	Definition
1D	One-dimensional
2D	Two-dimensional
3D	Three-dimensional
CFL	Courant-Friedrichs-Lewy condition
FEBOUSS	Finite element Boussinesq model
FE	Finite element
FEM	Finite element method
FFT	Fast Fourier transform
FSI	Fluid-structure interaction
MLS	Moving least squares
VLFS	Very large floating structure

List of Latin symbols

Symbol	Definition
A_r	Relative amplitude error parameter
B	Bilinear form
B_s	Beam ship
c	Shallow water wave celerity
d	Instantaneous total water depth
D	Draught function
D_s	Draught ship
f	Wave frequency
f_l	Linear wave frequency
f_p	Peak wave frequency
Fr_d	Depth-Froude number
g	Gravitational acceleration
h	Still-water depth
H_{max}	Maximum waveheight
H_Ω	Height FSI model
k	Wavenumber
L	Linear form
L_a	Length sponge layer FEBOUSS model
L_d	Length damping zone FSI model
L_{fs}	Length free surface
L_m	Length membrane
L_s	Length ship
L_x	Width FEBOUSS model
L_y	Length FEBOUSS model
L_Ω	Length FSI model
m_ρ	Mass parameter membrane
$\mathbf{n}$	Outward pointing normal vector
p	Wave-induced pressure

P	Depth-integrated velocity in x-direction
P_d	Statistical error parameter
Q	Depth-integrated velocity in y-direction
t	Time variable
$\tilde{t}$	Non-dimensionalised time
T	Wave period
t_{sim}	Total simulation duration
T_ρ	Pre-tension parameter
u	Weight function
u_{in}	Normal velocity at FSI inlet boundary
u_{out}	Normal velocity at FSI outlet boundary
v	Weight function
v_s	Velocity moving ship
w	Weight function
w_{in}	Depth-resolved vertical velocity
$w_{in,0}$	Vertical velocity at free surface
W_Ω	Width FSI model
W_{fs}	Width free surface
W_m	Width membrane
x	Horizontal axis
x_s	x-coordinate center ship
y	Horizontal axis
y_s	y-coordinate center ship
z	Vertical axis

List of Greek symbols

Symbol	Definition
α_h	Stabilisation factor time-integration scheme
β_h	Parameter for controlling influence weight function
Δt	Time-step
Γ_b	Bottom boundary
Γ_{d1}	Inlet damping zone boundary
Γ_{d2}	Outlet damping zone boundary
Γ_{fs}	Free surface boundary
Γ_{in}	Inlet boundary
Γ_m	Fluid-membrane interface
Γ_{out}	Outlet boundary
η	Membrane deflection
θ_s	Heading ship
κ	Free surface-elevation
κ_{max}	Maximum surface-elevation
κ_{min}	Minimum surface-elevation
κ_{ref}	Reference surface-elevation
κ_0	Wave-amplitude
$\hat{\kappa}$	Enforced free surface-elevation
λ	Wavelength
Λ_m	Membrane edges
μ_0	Relaxation parameter
μ_1, μ_2	Relaxation functions
Π	Source pressure term
ρ	Fluid density
τ	Viscous damping

ϕ	Velocity potential
$\hat{\phi}$	Enforced velocity potential
ω	Angular frequency
ω_n^{dry}	Dry natural frequency
Ω	Fluid domain
Ω_{d1}	Inlet damping zone
Ω_{d2}	Outlet damping zone

1 Introduction

The concept of floating offshore structures is gaining considerable attention for various innovative applications, such as floating airports, floating bridges, and even floating cities. Unlike traditional ships and offshore platforms, these novel structures are, in some cases, envisioned to span several kilometers, which presents entirely new challenges in their structural design. Despite growing interest, much remains unexplored in the existing literature regarding several complex phenomena critical to the design of these structures. This thesis focuses on one such topic: the structural behaviour of thin, plate-shaped floating membranes when excited by waves generated by moving vessels in waterways. This chapter will first outline the societal relevance of these structures, followed by a detailed definition of the research problem, objectives, and methodology used to address the main research questions of this work.

1.1. Background

The world is currently experiencing a significant increase in urban population. By 2030, one-third of the global population is estimated to be living in an urban area, with at least half a million inhabitants each, according to recent studies by the United Nations [28]. Upon examination of geospatial data, it becomes apparent that many metropolises are situated near coastlines or rivers due to the historical advantages of water transportation for commerce, as well as the availability of fresh water resources. Over time, this has resulted in densely populated regions with often insufficient space to accommodate all societal needs on land. Another major challenge society faces nowadays is the various severe consequences of climate change in different parts of the world. More and more regions are facing extreme, years-long droughts, increased flood risks due to rising sea levels, tropical storms, and more frequent heatwaves. Given the fact that certain regions will become uninhabitable in the future, due to these effects of climate change on the environment, more people may feel compelled to move from rural areas to urban centers. This migration contributes to the already significant burden on big cities.

As approximately 71 percent of the Earth's surface is covered by water, people have extensively made use of traditional land reclamation methods until now to gain new land from oceans, seas, riverbeds, and lakes in an artificial manner. This method of creating new land has encountered criticism from various sources over the past couple of years [16]. It turns out that current land reclamation methods are only applicable in areas with relatively shallow waters, are prone to earthquakes, require long construction times, are affected by sea-level rise due to global warming, and can negatively affect the environment, such as sea current, water quality, and marine ecosystem. Clearly, relying solely on traditional land reclamation methods to solve global problems does not fully provide a sustainable solution for the future, especially in today's context of civil engineering, where sustainability is an increasingly important consideration. At this point, considering the application of an alternative and innovative technology, namely big floating structures resting on the water surface, could provide promising solutions to the environmental challenges over currently employed traditional land reclamation methods [34].

A specific category of structures that rest on the water surface and are widely studied nowadays is known as very large floating structures (VLFS). These structures, fully supported by their own

buoyancy, can be broadly categorised into the semi-submersible type and the pontoon type. The semi-submersible type features a platform elevated above sea level through the use of columns and is particularly suitable for deployment in locations characterised by rough waters. The pontoon type[1] on the other hand, resembling a thin plate-shaped platform, is intended for deployment in relatively calm waters, such as a bay, lagoon, or harbour. The pontoon type VLFS are characterised by large horizontal dimensions with respect to the draught of the structure. To prevent VLFS from drifting sideways during critical sea states, they are typically secured to the seabed using a mooring system.

The concept of VLFS, as known today, was introduced around 1920 as a design proposal for a seadrome for aircraft to land and take off from, as well as to provide parking areas [34]. This concept was used on a large scale by the US Navy during the Second World War. By the 1970s, Japanese researchers had made significant progress towards developing the concept of floating airports [33]. In 1995, they constructed the Mega-Float runway in Tokyo Bay, which measured 1000 meters in length, with a width ranging from 60 to 120 meters, and a thickness of 3 meters, as shown in Figure 1.1.

Figure 1.1: Large artificial floating island: mega-Float runway in Tokyo Bay in Japan, 1995 [7].

To address various environmental challenges, such as land scarcity and increasingly stringent global climate change policies, floating structures have regained significant interest across a wide range of applications over the past two decades [34]. Technological developments for the design of floating renewable energy systems, floating energy storage facilities, floating breakwaters, floating airports, floating bridges, and even floating modular cities have recently attracted the attention of a growing audience, leading to innovative and promising concepts.

However, as the technology for floating offshore structures is a relatively new field of research with a broad range of potential applications, several novel structural and hydrodynamic challenges must be addressed before these structures can be successfully implemented. Therefore, this thesis focuses on the coupling of a hybrid model to investigate a unique type of fluid-structure interaction (FSI), which will be explored in detail throughout the remainder of this work.

1.2. Problem statement and novelties

Previous research in offshore engineering literature, involving analytical, numerical, and experimental models, has primarily focused on the interaction between thin, flexible floating structures combined with theoretical linear, regular incoming waves [36]. However, this wave condition scenario is hardly observed in offshore engineering practice. Nevertheless, these studies have identified a wide variety of possible responses, ranging from cases where the floating structure closely follows the local wave-elevation to scenarios dominated solely by rigid body motions. As previously mentioned, the growing interest in floating structures has also led to several novel and practical research inquiries. One such inquiry, which is a main topic of this thesis, examines the behaviour of thin, plate-shaped membranes floating in relatively calm waters, excited by waves generated by nearby passing vessels.

[1] For the remainder of this work, the focus will be solely on pontoon type floating structures.

To provide a real-life perspective on the problem statement of this thesis, Figure 1.2 presents a relevant example that can be encountered worldwide. The satellite images depict a high-traffic region in the Port of Rotterdam, Netherlands, where a floating structure is currently located in the Dokhaven harbour. As shown in Figure 1.2a, this structure is fully exposed to ship-induced waves, as there is no breakwater to mitigate the impact when a ship passes through the Nieuwe Maas, the adjacent navigation channel. A different problem, distinct from the one being studied in this thesis, encountered in hydraulic engineering has highlighted the potentially destructive nature of ship-induced waves propagating towards riverbanks, which have been shown to cause severe erosion over time [13]. These long-period ship-induced waves can travel considerable distances and significantly impact the surrounding areas, as illustrated in Figure 1.2b, which shows a vessel navigating out of the port of Rotterdam and generating a large wake. This consideration could be particularly important for floating structures, especially if only short wind-generated waves are accounted for in their design. Therefore, understanding the effects of ship-induced waves on floating structures may be essential and requires thorough investigation, particularly in high-traffic regions.

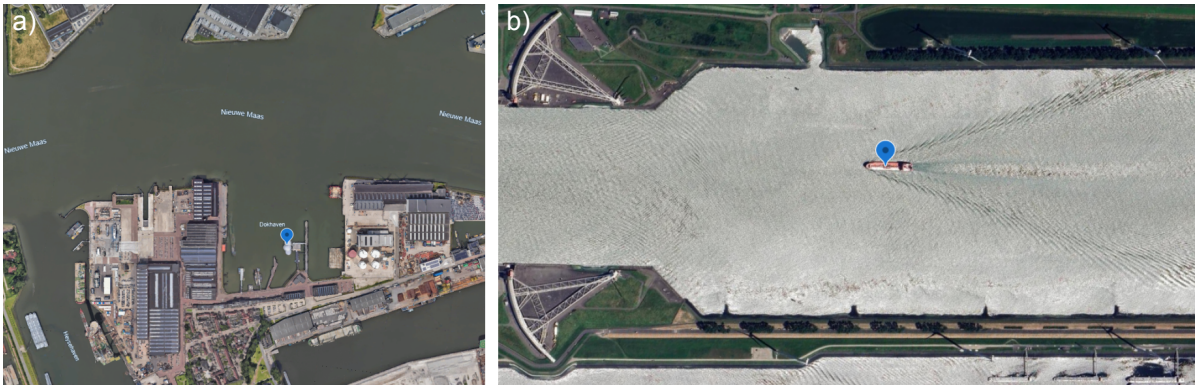

Figure 1.2: a) Floating structure in Dokhaven harbour, located at 51.898° N, 4.423° E, dated May-2023. b) Moving ship, located at 51.951° N, 4.172° E, generating large waves propagating towards river bank when navigating out of the port of Rotterdam, dated June-2024. Satellite images obtained from Google Earth.

Ship-induced waves are characterised by fairly long wavelengths, an irregular wave-train, and a transient nature [3]. In some cases, the length of these waves can be comparable to that of floating structures, which may lead to interesting physical phenomena, such as resonance. This phenomenon is highly undesirable in many applications, as it can result in excessively high deformations and stresses in the structure. In addition to the remarkable characteristics of the incoming waves, the stiffness properties of a thin elastic floating structure significantly influence its response. Due to the large horizontal dimensions and relatively small draught, the overall structural stiffness is relatively low, which may cause the structure to behave like thin elastic plates. This behaviour has been demonstrated in models studying solutions of Poisson-Kirchhoff plate equations coupled with free surface flow [14]. The flexible structural behaviour, governed by incoming wave excitation and structural rigidity, is referred to as hydroelasticity in the field of fluid-structure interaction and will also be investigated here in the context of membranes excited by ship-induced waves.

When studying problems concerning the propagation of ship-induced waves towards a structure, one typically deals with a large simulation domain. In order to avoid a computationally inefficient situation, that leads to excessively long simulation times, employing a hybrid modelling approach can be advantageous [23]. The hybrid model to be used in this study will need to integrate two distinct models, one for wave-generation and another for fluid-structure interaction considerations, into a single, efficient numerical framework. Each distinct model brings its own specific purpose and limitations to this modelling approach. The concept of hybrid modelling has also been gaining popularity lately for simulating different physics in subdomains of a model [5], along with technological developments related to increasing computing power over the past couple of decades. A major concern with this approach, and what remains unclear, is how to effectively implement the coupling at the interface between the two models. Therefore, this thesis also focuses on addressing the coupling of the two distinct models to ensure an effective numerical integration.

To the best of the author's knowledge, this rare type of fluid-structure interaction between ship-induced waves and large thin plate-shaped elastic floating structures, along with the implementation of a coupled hybrid modelling approach, has not been reported by other researchers in contemporary literature.

1.3. Objectives

The primary objective of this research study is to understand the hydroelastic behaviour of thin floating structures in relatively calm waters that are excited by waves generated by a moving ship, utilising a hybrid model. This model will evaluate the potential for resonance and, if it occurs, determine the conditions under which it might arise. To facilitate the achievement of this objective, the second aim of this thesis is to develop an efficient coupling algorithm for the hybrid model through a programming implementation. This algorithm needs to enable an accurate transfer of wave-information from a wave-generation model to a separate FSI model, ensuring minimal loss of accuracy in the representation of underlying physical phenomena.

1.4. Research questions

In line with the objectives of this thesis, which aim to bridge the previously outlined knowledge gap in the field of fluid-structure interaction, five interrelated research questions have been formulated to analyse thin, elastic floating structures excited by ship-induced waves. Therefore, the two primary research questions addressed in this work are outlined as follows:

- **How can an efficient numerical fluid-fluid coupling algorithm be developed to couple a wave-generation model with a fluid-structure interaction model?**
- **How does the variation in ship speed influence the hydroelastic response of a floating membrane exposed to ship-induced waves in relatively calm waters?**

Accordingly, three sub-questions have been posed to address the main research questions. The results for these inquiries will be obtained sequentially, in the order listed below:

- What are the characteristics of ship-induced waves, and how does wave propagation influence the wave conditions?
- What effect does a vessel's movement, at different constant velocities, have on the wave field?
- Can resonance of the floating structure be expected, and if so, under what conditions might it occur?

This thesis defines the scope of the research questions by focusing on the scenario of a vessel moving along a fixed prescribed path within a finite simulation domain at various constant velocities. This scenario is particularly relevant in navigation channels, where vessels must adhere to predetermined navigation paths and maintain specific maximum velocities. The floating structure will be modelled as a finite-dimensional square membrane, although it can represent various geometries and dimensions, providing opportunities for further exploration in future studies.

1.5. Methodology

To effectively study the interaction between ship-induced waves and floating structures within the hybrid modelling framework, it is crucial to select appropriate models, recognise the limitations of each model, and ensure that information is efficiently transferred from one model to another. Currently, numerous models are available for simulating the propagation and transformation of waves, particularly those generated by wind. The same applies to FSI models, of which there are many. The choice of a suitable model depends on the specific problem setting.

Apart from wind-generated waves, Boussinesq-type[2] models have proven capable of simulating the category of waves generated by a moving ship across a large domain with variable bathymetry. Additionally, their ability to capture three-dimensional physics on a two-dimensional scale enhances

[2] Over time, numerous variants of the classical Boussinesq equations (1872) have been developed by various researchers to incorporate specific physics or improve certain wave characteristics [12].

computational efficiency, making them particularly attractive for such simulations. In this thesis, a specific variant, previously extended to simulate ship-induced waves and referred to as FEBOUSS, will be used [3]. This model has been successfully validated in various scenarios against other numerical models and field measurements.

For the hydroelastic analysis of floating membranes, a different three-dimensional FSI model will be employed. This model has demonstrated the ability to couple free surface flow equations with Poisson-Kirchhoff plate equations to simulate the behaviour of VLFS [14]. Additionally, it has been validated across various test cases to analyse the hydroelastic behaviour in problems involving variable bathymetry and arbitrary structural geometries.

In general, significant challenges can arise in developing effective coupling methodologies for problems involving both solid and fluid dynamics simultaneously [19]. Therefore, it is crucial for the hybrid modelling approach that wave-information is accurately transferred from the two-dimensional FEBOUSS model to the three-dimensional FSI model. This type of coupling is commonly referred to as fluid-fluid coupling in literature [23]. Consequently, a new coupling algorithm will be developed and also thoroughly validated for a variety of test cases in this work.

The methodology, including the programming implementation for conducting the hydroelastic analysis, is summarised in the flowchart presented in Figure 1.3.

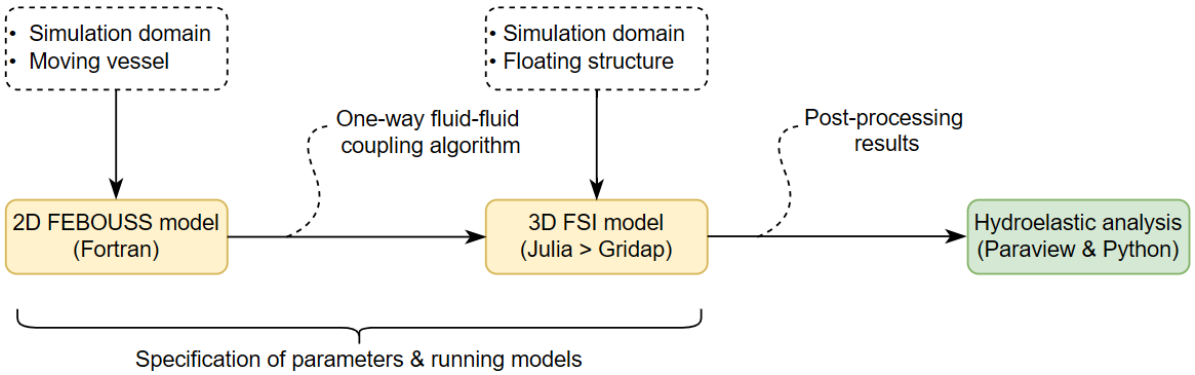

Figure 1.3: Methodology for analysis of ship-induced waves interaction with floating membranes.

The FSI model will be numerically implemented in *Julia* programming language [10], using the free and open-source [8] finite-element library *Gridap*. The *Gridap* library, fully implemented in *Julia*, can be used to solve various types of partial differential equations with different finite element methods. This library offers good computational performance compared to other programming languages, while its major advantage is the ease of implementing the mathematical weak form of a problem in a very similar manner to how it would be written on paper. The results of the FEBOUSS wave-generation quantities will be obtained using *Fortran*, a programming language particularly well-suited for intensive numerical computations. The generation of the domain mesh is also accomplished with *Fortran*. For large computing resources to perform the numerical simulations, the *Delft High Performance Computing Centre (DHPC)* of Delft University of Technology [1] will be utilised. Finally, post-processing of data for all visualisations obtained from finite element modelling will be conducted using *Python* and *Paraview*.

1.6. Thesis outline

This thesis is organised as follows: Chapter 2 details the setup of the hybrid modelling approach, including the governing equations in continuous form, for analysing ship-induced waves interacting with floating membranes. In Chapter 3, the numerical framework for the analysis of the hydroelastic problem is described, outlining the discretised problem to be solved and providing details of the proposed fluid-fluid coupling algorithm. The thesis then presents numerous numerical results regarding fluid-fluid coupling and hydroelastic behaviour in Chapter 4, addressing the research questions posed in Section 1.4. This leads to the conclusion in Chapter 5, summarising the findings and their implications. Finally, Chapter 6 discusses the limitations of this work and provides recommendations for future research.

2

Governing equations

The interaction between an elastic solid body and a surrounding flowing fluid can give rise to a wide variety of physical phenomena. To understand these phenomena, it is essential to appropriately model both the solid and the fluid. This chapter outlines the details, including the mathematical equations of the hybrid model components utilised in this thesis. Specifically, it describes two distinct time-domain models: a weakly nonlinear 2D wave-generation model and a linearised 3D fluid-structure interaction model, which ultimately will be coupled into a single efficient numerical framework in Chapter 3. The hydroelastic behaviour of the floating structure will be analysed using thin linear membrane equations of motion. Finally, the extension of the Boussinesq-type model will be presented to simulate waves generated by a moving vessel.

2.1. Model description

As previously mentioned, hybrid modelling has become an increasingly popular choice for offshore engineering for various reasons. In this study, the overall three-dimensional hybrid model comprises the FEBOUSS wave-generation model, which occupies the largest part of the domain and is capable of handling large, arbitrarily shaped domain boundaries. Within this, a smaller cuboid subdomain representing the FSI model is included, as illustrated in Figure 2.1 for the most generic case.

The FEBOUSS model is computationally very efficient because the governing equations of motion are integrated over the depth, effectively reducing a three-dimensional wave-generation model to a two-dimensional one without significantly compromising accuracy or the underlying physics. Consequently, the computationally more expensive, fully depth-resolved three-dimensional FSI model is required only within the smaller subdomain.

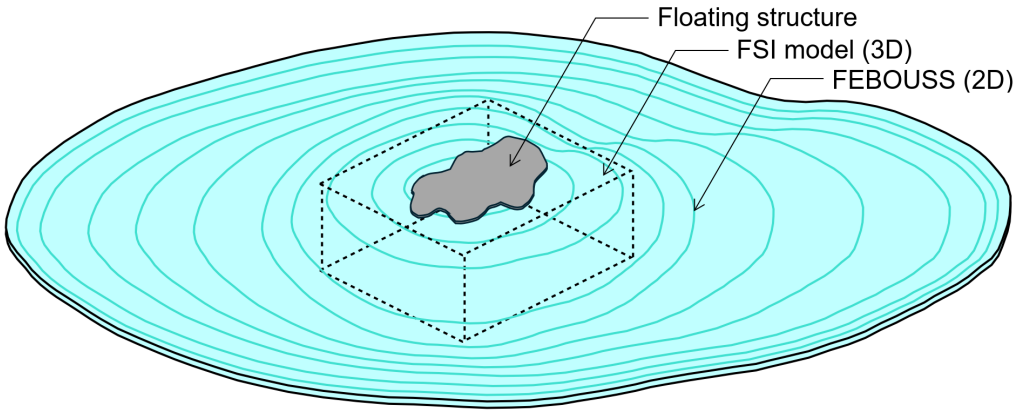

Figure 2.1: Three-dimensional hybrid model composed of FEBOUSS wave-generation model and FSI model.

Local Cartesian coordinate systems will be used for both the wave-generation model and FSI model. In these systems, x and y represent horizontal axes along which the waves can freely propagate, while z denotes the vertical axis, oriented positively upwards with $z = 0$ marking the still-water level. Generally, the FSI model is capable of handling wave input from multiple boundaries simultaneously and can accommodate arbitrarily-shaped floating structures.

More detailed information, including the underlying physical assumptions and equations of motion for both the FSI model and FEBOUSS, can be found in Section 2.2 and 2.3, respectively. These sections present the equations in their continuous form. In Chapter Chapter 3, the discretised problem formulation is introduced, along with the proposed numerical fluid-fluid coupling algorithm that integrates the two models.

2.2. Fluid-structure interaction model

A three-dimensional, time-domain, linearised monolithic finite element FSI model will be employed to study the hydroelastic behaviour of thin plate-shaped structures excited by waves. This model is capable of coupling free surface flow equations governed by linear potential flow theory with two-dimensional linear viscoelastic membrane equations [14][4]. A distinctive feature of this FSI problem is that it leads to a mixed-dimensional mathematical problem formulation. Specifically, this involves a system of partial differential equations defined across domains of different topological dimensions, where the unknown two-dimensional solid field is defined solely at the upper boundary of the 3D fluid domain.

The FSI problem consists of a fluid domain denoted by Ω with a thin floating structure on top, which can cause hydroelastic dispersion and subsequently affect the local flow field around the floating structure. This domain is bounded by the bottom surface Γ_b, the inlet surface Γ_{in}, the outlet surface Γ_{out}, the fluid free surface Γ_{fs}, damping zones Γ_{d1} and Γ_{d2}, and the interface with the thin floating membrane Γ_m. In the case of assuming a rectangular membrane, the edges of the floating structure are denoted by Λ_m. A schematic of this idealised boundary value problem, assuming wave input from only one face, is presented in Figure 2.2a.

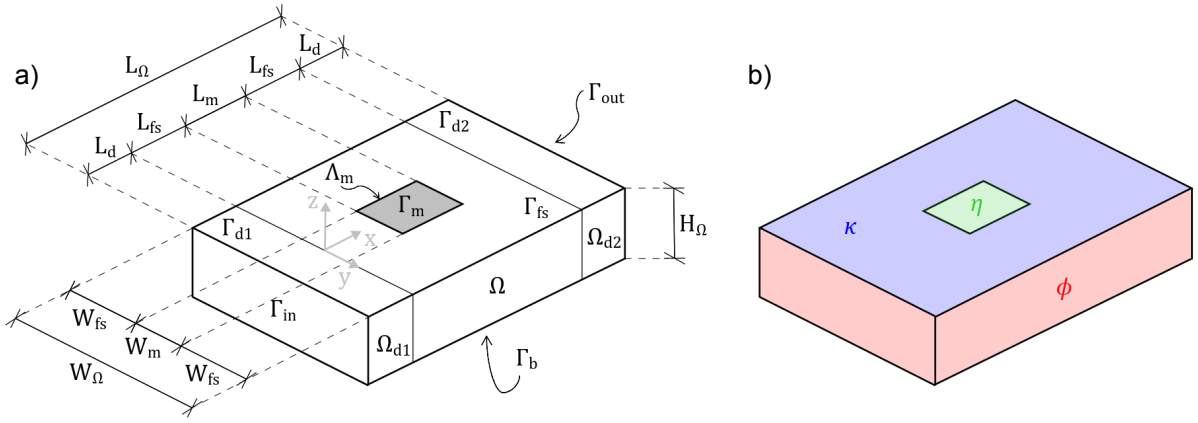

Figure 2.2: a) Schematic of the 3D fluid-structure interaction boundary value problem. b) Representation of the a priori unknown field variables.

The length, width, and height of the FSI model are denoted by L_Ω, W_Ω, and H_Ω, respectively. The length of the membrane is represented by L_m and the width by W_m. The FSI model features two damping zones, each with a length of L_d and a distance of L_{fs} before and after the structure, allowing waves to propagate freely inward and outward from the structure. Additionally, there are spaces for wave propagation adjacent to the membrane, denoted by W_{fs}. Let κ denote the surface-elevation relative to the fluid at rest. Normal vectors pointing outward from any surface will be denoted by $\mathbf{n}$ hereafter. Note that the detailed 3D domain in Figure 2.2a represents the smaller FSI subdomain shown in Figure 2.1, specifically for the case of selecting a rectangular structure and assuming wave input from only one face. The three a priori unknown field variables that the FSI model intends to solve, along with where they are defined, are depicted in Figure 2.2b.

2.2.1. Linear potential flow theory

In order to simplify this complex problem, typical assumptions in offshore engineering are applied to the fluid domain Ω: the fluid is considered inviscid, incompressible, and irrotational. Additionally, the free surface-elevation, is assumed to be small relative to both the wavelength and the water depth, permitting an accurate description by (linear) potential flow theory. Furthermore, the waves generated by the FEBOUSS model, which serve as input to the FSI model, are assumed to have relatively low steepness. It is also assumed that there is no cavitation, meaning there is no detachment of the floating structure from the fluid free surface. Cases involving high nonlinearities, viscous flow effects, or large structural deformations are beyond the scope of this work.

In the fluid domain Ω, for irrotational and inviscid flow with fluid velocity vector denoted by $\mathbf{u}$, a scalar potential field $\phi(x, y, z, t)$ exists such that $\mathbf{u} = \nabla\phi$. Given the incompressibility of the flow, which implies $\nabla \cdot \mathbf{u} = 0$, these conditions combine to yield the governing equation for a potential flow as follows:

$$\Delta\phi = 0 \quad \text{in} \quad \Omega. \tag{2.1}$$

Next, the governing fluid domain equation needs to be supplemented with the appropriate boundary conditions. The kinematic boundary conditions are given by

$$\mathbf{n} \cdot \nabla\phi = 0 \qquad \text{on } \Gamma_b, \tag{2.2a}$$
$$\mathbf{n} \cdot \nabla\phi = u_{in} \qquad \text{on } \Gamma_{in}, \tag{2.2b}$$
$$\mathbf{n} \cdot \nabla\phi = u_{out} \qquad \text{on } \Gamma_{out}, \tag{2.2c}$$
$$\mathbf{n} \cdot \nabla\phi = \dot{\kappa} \qquad \text{on } \Gamma_{fs}. \tag{2.2d}$$

The first boundary condition, Equation 2.2a, physically implies a no-penetration condition through the bottom boundary, meaning that there is no fluid flow through the seabed. Equations 2.2b and 2.2c prescribe the normal velocities u_{in} and u_{out} at the inlet and outlet boundary, respectively. The final kinematic boundary condition, Equation 2.2d, represents the linearised free surface condition. It relates the time derivative of the free surface-elevation, denoted with the upper dot sign, to the flow velocity, expressing that there is no fluid flow across the moving free surface.

The wave-induced pressure in the water at the free surface can be described by the Bernoulli equation, which reads:

$$p = -\rho\dot{\phi} - \rho g\kappa - \frac{1}{2}\rho(\nabla\phi)^2, \tag{2.3}$$

where ρ is the fluid density and g is the gravitational acceleration. By retaining only the linear terms in Equation 2.3, one arrives at the linearised Bernoulli equation as follows:

$$p = -\rho\dot{\phi} - \rho g\kappa. \tag{2.4}$$

The pressure at the free surface is described based on the linearised Bernoulli equation. By assuming that the pressure at the free surface equals the atmospheric pressure, and thus approximating it as zero, the resulting dynamic free surface boundary conditions becomes:

$$\dot{\phi} + g\kappa = 0 \quad \text{on } \Gamma_{fs}. \tag{2.5}$$

With the fluid domain's equations of motion and boundary conditions for the FSI model set, the analysis now shifts to the crucial interface condition between the fluid and the floating membrane.

2.2.2. Hydroelastic membrane theory

A thin elastic floating membrane can be envisioned as a tensioned plate following the classical Euler-Bernoulli beam hypothesis, where plane sections remain plane and normal to the axis of the beam after deformation. Additionally, for a membrane, the bending stiffness is assumed to approach zero. This subsection presents generic equations of motion for viscoelastic[1] floating membranes.

Consider a 2D viscoelastic membrane floating in the (x, y)-plane within a 3D fluid domain. The membrane is subjected to a transverse distributed load per unit area, denoted by $p_m(x, y, t)$, which

[1] The complete viscoelastic equations of motion are presented here to facilitate future research.

arises due to fluid-structure coupling. The equation of motion for studying small transverse vibrations of the floating membrane, denoted by $\eta(x, y, t)$, is expressed in vector form as follows:

$$m\ddot{\eta} - \nabla_h \cdot (T\nabla_h \eta) - \nabla_h \cdot (\tau T \nabla_h \dot{\eta}) = p_m, \tag{2.6}$$

where $\nabla_h(\cdot) = \frac{\partial(\cdot)}{\partial x}\hat{i} + \frac{\partial(\cdot)}{\partial y}\hat{j}$. The parameters to quantify the membrane's properties are: m for the mass per unit area, T for the pre-tension, and τ for viscous damping. In 2D, the mass per unit area is defined as $m = \rho_m h_m$, where ρ_m is the material density and h_m is the height of the membrane's cross-section, assuming a rectangular shape. Given the spatial order of Equation 2.6, only one boundary condition is required per edge, which is represented as a line segment for a 2D membrane. The boundary condition considered here allows the membrane to freely vibrate in the z-direction and is expressed as:

$$\mathbf{n} \cdot \nabla_h \eta = 0 \quad \text{on } \Lambda_m. \tag{2.7}$$

In this work, an inextensible, isotropic, and homogeneous membrane is considered, with no material damping ($\tau = 0$), simplifying Equation 2.6. A uniform static pre-tension T is applied across the membrane, allowing constants to be factored out of the gradients. While these assumptions simplify the model, the equations can also be used for anisotropic membranes, where m, T, and τ vary across the structure.

2.2.3. Fluid-structure coupling

To complete the formulation of the FSI problem, the interface conditions between the fluid and solid must be specified. The fluid free surface under the structure will conform to the deflection of the membrane, adhering to the assumptions of no cavitation and small transverse vibrations. Consequently, the kinematic free surface boundary condition on Γ_m is mathematically expressed by equating $\dot{\eta}$ with the normal flow velocity $\mathbf{n} \cdot \nabla\phi$. Additionally, the dynamic free surface boundary condition under the plate is derived by equating the transverse load p_m on the membrane, from Equation 2.6, with the free surface pressure from the linearised Bernoulli equation. Thus, the resulting kinematic and dynamic coupling boundary conditions at the fluid-structure interface for the overall 3D problem are given as follows:

$$\mathbf{n} \cdot \nabla\phi = \dot{\eta} \qquad \text{on } \Gamma_m, \tag{2.8a}$$

$$m_\rho \ddot{\eta} - \nabla_h \cdot (T_\rho \nabla_h \eta) - \nabla_h \cdot (\tau T_\rho \nabla_h \dot{\eta}) + \dot{\phi} + g\eta = 0 \qquad \text{on } \Gamma_m, \tag{2.8b}$$

where $m_\rho = m/\rho$ denotes the submerged draught of the membrane and $T_\rho = T/\rho$. This concludes the continuous formulation of the mixed-dimensional boundary value problem.

In summary, the governing three-dimensional fluid domain is now described by Equation 2.1, supplemented by boundary conditions outlined in Equation 2.2 and 2.5 for fluid the domain, and Equation 2.8 for the fluid-structure coupling. Additionally, the boundary condition specified in Equation 2.7 is applied to the edges of the membrane. This formulation results in a well-posed problem that can be solved for the unknown field variables. The numerical framework for solving this coupled system of equations is detailed in Section 3.2, preceded by the presentation of the governing equations of the wave-generation model and the proposed fluid-fluid coupling.

2.3. Wave-generation model

The most widely accepted (weakly) nonlinear theory for analysing two-dimensional horizontal wave propagation in the (x, y)-plane is the theory of Boussinesq (1872) [21], which was originally developed for one-dimensional wave propagation over a horizontal bottom and later expanded by numerous researchers. These variants are hence referred to as Boussinesq-type models to clarify the distinction from the original formulation.

The applicability of Boussinesq-type models for long-wave simulations in finite water depths is determined by two critical parameters: the nonlinearity parameter $\epsilon = \kappa_0/h$ for quantifying the wave steepness, where κ_0 represents the wave-amplitude, h is the still water-depth, and the dispersion parameter $\sigma = h/\lambda$ for assessing the relative depth, where λ denotes the wavelength.

2.3.1. Weakly nonlinear potential flow theory

The classical form of the Boussinesq-type equations [30], commonly used for offshore engineering nowadays, was derived using depth-integrated quantities with Euler's equations of motion for an inviscid and incompressible fluid as a starting point, assuming an irrotational flow, weak nonlinearity, and

weak dispersion. As a result, these equations are only valid for small amplitude waves in shallow waters up to $kh \approx 1$, provided that $O(\sigma^2) = O(\epsilon) \ll 1$, where $k = 2\pi/\lambda$ represents the wave-number.

In later studies, the dispersion characteristics and depth restrictions were addressed using long-wave equations, leading to the formulation by Madsen and Sørensen [2] of the Boussinesq equations. This modified formulation, still only valid for small amplitude waves, maintains weak nonlinearity and weak dispersion, but extends its applicability to intermediate depths up to $kh \approx 3$. It is important to note that the work presented here does not apply to breaking waves, nor does it allow for the analysis of viscous flow effects.

The FEBOUSS model, which is based on Madsen and Sørensen's depth-integrated form of the Boussinesq-type equations for slowly varying bathymetries [25], includes an enhancement to simulate ship-induced waves [3]. The continuity equation, along with the depth-integrated conservation of momentum equations in the x and y directions, are presented as follows:

$$\frac{\partial \kappa}{\partial t} + \frac{\partial P}{\partial x} + \frac{\partial Q}{\partial y} = 0, \tag{2.9a}$$

$$\frac{\partial P}{\partial t} + \frac{\partial}{\partial x}\left(\frac{P^2}{d}\right) + \frac{\partial}{\partial y}\left(\frac{PQ}{d}\right) + gd\frac{\partial \kappa}{\partial x} + \Psi_x + \frac{\tau_1}{\rho} + \frac{d}{\rho}\frac{\partial \Pi}{\partial x} = 0, \tag{2.9b}$$

$$\frac{\partial Q}{\partial t} + \frac{\partial}{\partial x}\left(\frac{PQ}{d}\right) + \frac{\partial}{\partial y}\left(\frac{Q^2}{d}\right) + gd\frac{\partial \kappa}{\partial y} + \Psi_y + \frac{\tau_2}{\rho} + \frac{d}{\rho}\frac{\partial \Pi}{\partial y} = 0. \tag{2.9c}$$

Here, g represents the gravitational acceleration, ρ is the water density, κ is the free surface-elevation, h is the still-water depth, and $d = h + \kappa$ is the instantaneous total water depth. Additionally, $P = \int_{-h}^{\kappa} u_x \, dz$ and $Q = \int_{-h}^{\kappa} u_y \, dz$ represent the depth-integrated directional velocity components along the x and y axes, respectively. The setup of the FEBOUSS model, including the a priori unknown field variables at an arbitrary point $S(x, y)$, to be solved, is shown in Figure 2.3.

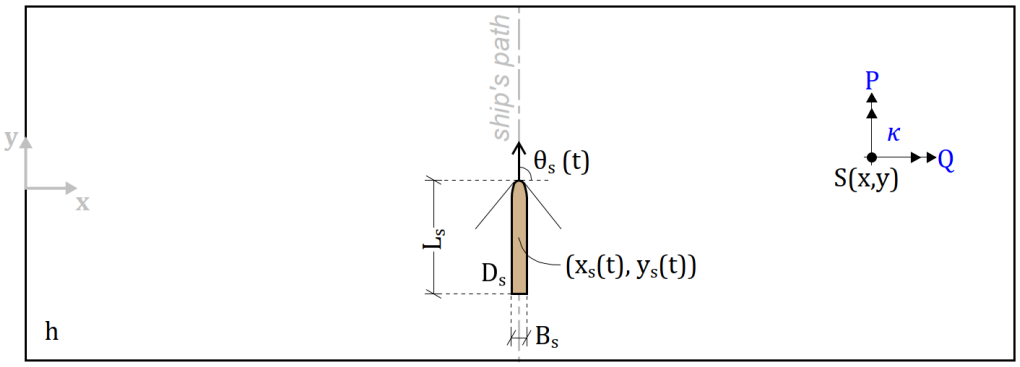

Figure 2.3: Setup FEBOUSS wave-generation model and a representation of the a priori unknown field variables.

The Boussinesq terms, Ψ_x and Ψ_y, in the momentum equations contribute to the dispersion characteristics of the model and are expressed as follows:

$$\Psi_x = -\left(\tilde{B} + \frac{1}{3}\right) h^2 \left(\frac{\partial^3 P}{\partial x^2 \partial t} + \frac{\partial^3 Q}{\partial x \partial y \partial t}\right) - h\frac{\partial h}{\partial x}\left(\frac{1}{3}\frac{\partial^2 P}{\partial x \partial t} + \frac{1}{6}\frac{\partial^2 Q}{\partial y \partial t}\right) - \frac{1}{6}h\frac{\partial h}{\partial y}\frac{\partial^2 Q}{\partial x \partial t} - \tilde{B}gh^2\frac{\partial \tilde{\omega}}{\partial x}, \tag{2.10a}$$

$$\Psi_y = -\left(\tilde{B} + \frac{1}{3}\right) h^2 \left(\frac{\partial^3 P}{\partial x \partial y \partial t} + \frac{\partial^3 Q}{\partial y^2 \partial t}\right) - h\frac{\partial h}{\partial y}\left(\frac{1}{6}\frac{\partial^2 P}{\partial x \partial t} + \frac{1}{3}\frac{\partial^2 Q}{\partial y \partial t}\right) - \frac{1}{6}h\frac{\partial h}{\partial x}\frac{\partial^2 P}{\partial y \partial t} - \tilde{B}gh^2\frac{\partial \tilde{\omega}}{\partial y}, \tag{2.10b}$$

where $\tilde{B}$ is the free parameter for controlling the dispersion characteristics of the model. By conducting comparisons between different wave-generation models, it was concluded that the value of $\tilde{B} = 1/15$ produces the most accurate results [2][25] for the wave celerity up to intermediate water depths of $kh \approx 3$. To avoid complexities associated with higher-order spatial derivatives when applying the finite element method (FEM) [31] to solve the system of equations in space, the auxiliary variable $\tilde{\omega}$ is

introduced in the conservation of momentum equations and is defined as follows:

$$\tilde{\omega} = \frac{\partial}{\partial x}\left(h\frac{\partial \kappa}{\partial x}\right) + \frac{\partial}{\partial y}\left(h\frac{\partial \kappa}{\partial y}\right). \tag{2.11}$$

The terms proportional to τ_1 and τ_2 in the momentum equations represent the shear stress arising from the bottom boundary layer of a channel and are calculated as follows:

$$(\tau_1, \tau_2) = \rho C_b \frac{\sqrt{P^2+Q^2}}{d^2}(P, Q), \tag{2.12}$$

where C_b is the bottom drag, based on Manning's roughness coefficient [15]. Its contribution, however, will not be considered in this study, but is included for potential future research.

The final terms in the momentum equations, which involve gradients with respect to Π, are used to implement a moving pressure field approach for simulating ship-induced waves and will be discussed in more detail in the subsequent subsection.

2.3.2. Extension for simulating ship-induced waves

When a vessel moves through calm waters, it typically generates a wake known as a Kelvin wave pattern. This wake consists of two different classes of waves: transverse waves that propagate roughly perpendicular to the ship's path, and divergent waves that radiate diagonally outwards from the moving disturbance [35]. The entire wake is confined by two cusp lines at an angle commonly referred to as the Kelvin angle. The FEBOUSS model employs a moving pressure field approach to simulate the wake of a three-dimensional moving disturbance. This extension has been incorporated into the conservation of momentum equations through the addition of a source pressure term [3].

Mathematically, the generation of ship-induced waves is achieved by taking spatial derivatives of the surface pressure $\Pi(x, y, t) = \rho g D(x, y, t)$, as demonstrated in the last terms of Equations 2.9b and 2.9c. Physically this represents the hydrostatic pressure resulting from the vessel's local draught $D(x, y, t)$ at a specific time-instant t. The draught function $D(x, y, t) = D_s f(x')g(y')$, designed to accurately model the shape of the ship [18], is defined using two analytical expressions as detailed below:

$$f(x') = \begin{cases} \cos^2\left(\pi\left(\frac{x'-0.5\alpha_1}{1-\alpha_1}\right)\right) & 0.5\alpha_1 < x' \leq 0.5 \\ \cos^2\left(\pi\left(\frac{x'+0.5\alpha_2}{\alpha_2-1}\right)\right) & -0.5 \leq x' < -0.5\alpha_2 \\ 1 & -0.5\alpha_2 \leq x' \leq 0.5\alpha_1 \end{cases} \tag{2.13a}$$

$$g(y') = \begin{cases} \cos^2\left(\pi\left(\frac{y'-0.5\beta_1}{1-\beta_1}\right)\right) & 0.5\beta_1 < y' \leq 0.5 \\ \cos^2\left(\pi\left(\frac{y'+0.5\beta_1}{\beta_1-1}\right)\right) & -0.5 \leq y' < -0.5\beta_1 \\ 1 & -0.5\beta_1 \leq y' \leq 0.5\beta_1 \end{cases}. \tag{2.13b}$$

To compute the local draught D, it is necessary to have information about the ship's geometry and its heading, denoted by $\theta_s(t)$, relative to the positive x-axis. Let the length of the ship be denoted by L_s, the beam by B_s, the draught by D_s, and the center of the ship by $(x_s(t), y_s(t))$. Using this information, the coordinates x' and y' in the ship's local coordinate frame can be calculated as follows:

$$\begin{pmatrix} x' \\ y' \end{pmatrix} = \begin{bmatrix} \frac{1}{L_s} & 0 \\ 0 & \frac{1}{B_s} \end{bmatrix} \begin{bmatrix} \cos(\theta_s(t)) & \sin(\theta_s(t)) \\ -\sin(\theta_s(t)) & \cos(\theta_s(t)) \end{bmatrix} \begin{pmatrix} x - x_s(t) \\ y - y_s(t) \end{pmatrix}. \tag{2.14}$$

Here, three coefficients are present: $\alpha_1, \alpha_2 \in [0, 1]$ for shaping the bow and stern parts of the vessel, and $\beta_1 \in [0, 1]$ for defining the shape of the transverse cross-section. These coefficients enable the realistic modelling of both slender and bulky pressure fields [3][9].

In addition to the capabilities described above, the FEBOUSS model offers the flexibility to simulate waves generated by vessels moving at arbitrary velocities and following arbitrary paths, while also handling domains with arbitrary bathymetries. It can even model multiple moving vessels simultaneously by incorporating extra surface pressure terms into the governing equations.

2.4. Review coupling of distinct models

Now that the concept of hybrid modelling, in this case consisting of the separate FEBOUSS wave-generation model and the FSI model, has been described, the next challenge is to integrate them into a single efficient numerical framework. This section briefly reviews contemporary literature on how the FSI model has been enforced before, and how the FEBOUSS model has been coupled with another Navier-Stokes based fluid domain model. Coupling two models with different governing equations can involve several methods, as outlined in Reference [32]. The key consideration is how the coupling interface is numerically implemented to transfer wave-information between the models, which can occur at a single boundary or multiple boundaries depending on the specific problem.

The FEBOUSS model, previously used to simulate regular incoming waves, has been coupled with a Navier-Stokes model in 3D by enabling the potential flow solver in the far-field, where detailed flow information is not of interest, and using the computationally expensive Navier-Stokes solver near the structure, where more complex phenomena like steep wave conditions and wave breaking need to be modelled [5]. In these cases, full depth-resolved velocities and pressures around the structure's circumference were required for coupling. However, due to the necessity of pressure coupling conditions, which are numerically challenging, significant errors were observed in the transfer of wave-information between the models.

The FSI model has been successfully validated and implemented for analysing free surface waves interacting with VLFS [14]. In this implementation, the structure was enforced by Airy's wave theory using known analytical expressions by providing fluid particle velocities at the inlet boundary. However, the FSI model is highly versatile and can accommodate various types of wave input, depending on the specific application.

This review lays the groundwork for developing a state-of-the-art coupling algorithm between FEBOUSS and the FSI model in Chapter 3, an approach that has not been previously reported. The proposed coupling framework will be used to demonstrate the hydroelastic behaviour of floating membranes excited by ship-induced waves.

3

Numerical model

Numerical methods are crucial for analysing the hydroelastic behaviour of floating structures with finite dimensions and irregular shapes, or those subjected to complex wave inputs, as finding analytical solutions to the governing equations is rarely possible. This chapter begins by detailing the development of the novel fluid-fluid coupling algorithm for transferring wave-information from the FEBOUSS wave-generation model to the FSI model. The goal is to employ a hybrid numerical modelling approach to investigate the interaction of thin floating structures with ship-induced waves. Consequently, the continuous formulation of the governing equations, outlined in Chapter 2, is discretised in this chapter to enable the use of a monolithic finite element formulation to obtain solutions to the hydroelastic problem.

3.1. Fluid-fluid coupling algorithm

In this section, the general concept of how wave-information is transferred from FEBOUSS to the FSI model will be outlined, along with an existing numerical algorithm for retrieving depth-resolved velocities from the depth-integrated FEBOUSS model. This process facilitates the 3D fluid-fluid coupling within a region of the boundaries of the FSI model. The application of this coupling algorithm will be rigorously validated in Section 4.1.

3.1.1. Transfer of wave-information

Contemporary literature indicates that developing effective fluid-fluid coupling algorithms for hybrid models presents significant challenges [23]. This is primarily due to the necessity of satisfying compatibility requirements at the coupling interface, which can result in substantial convergence times for solvers. In this context, a novel one-way partitioned 3D fluid-fluid coupling algorithm will be explained, designed to couple the 2D FEBOUSS model with the 3D FSI model. The one-way coupling approach proposed for this study focuses solely on the transformation of waves into the FSI model, without considering the changes to the wave field caused by reflections from the FSI model back into the FEBOUSS domain. When coupling FEBOUSS with another model, it is preferable to avoid using pressures for coupling whenever possible, as reviewed in literature concerning FEBOUSS coupled with a Navier-Stokes model in Section 2.4. Additionally, it is preferable to couple models by passing through as few quantities as possible, while simultaneously balancing the trade-off between the efficiency and accuracy of the coupling algorithm [32].

A novel and efficient coupling algorithm is proposed in this subsection to transfer wave-information from FEBOUSS to the FSI model. The coupling strategy omits the use of pressure for coupling and relies solely on flow velocities and surface-elevations obtained from FEBOUSS. The integration of the two models can be efficiently achieved by introducing feeding particles in the damping zone Ω_{d1} of the FSI model. Similar to the wave input method used for the hydroelastic analysis of VLFS with free surface waves in Reference [14], depth-resolved horizontal velocity values u_{in}, in accordance with the specified boundary condition given by Equation 2.2b at Γ_{in} in the (y, z)-plane, will also be prescribed at the inlet of the FSI model. In addition, what primarily distinguishes this approach from others, is that the surface-elevation κ at the upper boundary of the damping zone Γ_{d1} at the inlet of the FSI model

will be prescribed, along with the normal fluid particle velocity $w_{in,0}$ to the (x, y)-plane[1]. For this thesis, a fixed overlapping zone will be established within the damping zone of the FSI model, as both are Eulerian models with fixed meshes. Here, wave-information can be gradually ramped between the two models using a relaxation function. This fluid-fluid coupling approach is depicted in Figure 3.1.

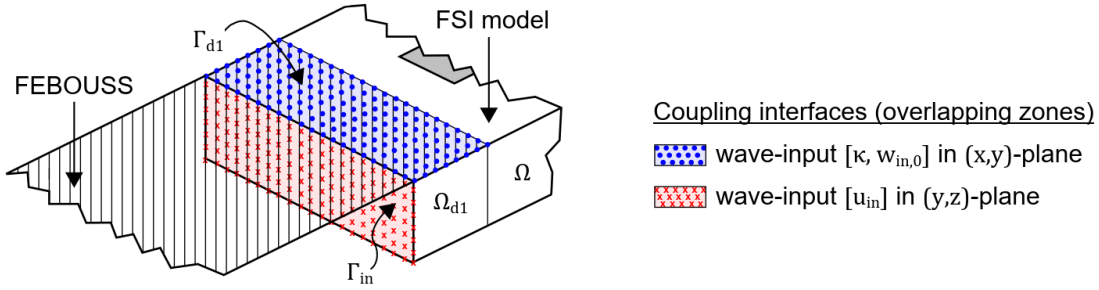

Figure 3.1: Schematic of 3D fluid-fluid coupling: one-way transfer of wave-information from FEBOUSS wave-generation model to FSI model with feeding particles placed at inlet damping zone of FSI model.

The implementation of this approach for wave input offers two major computational benefits. First, it can significantly reduce computational time by allowing the coupling zone to remain as compact as possible, thereby minimising the number of feeding particles required. Second, it alleviates storage demands, as managing a large volume of data can be demanding for a computational system. By employing this method, wave-propagation analysis towards the floating structure from the overlapping zone can be conducted efficiently. The proposed steps for transferring wave-information from FEBOUSS to the FSI model are summarised in the flowchart shown in Figure 3.2.

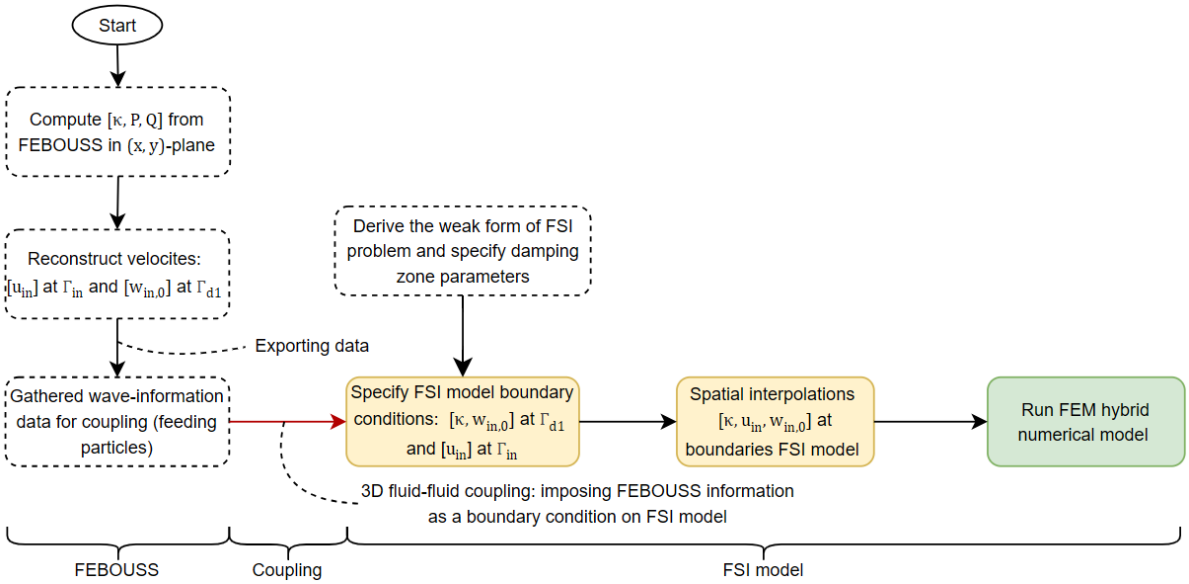

Figure 3.2: Flowchart one-way fluid-fluid coupling algorithm transfer wave-information from FEBOUSS to FSI model.

To facilitate numerical implementation, finite element (FE) spaces must be defined in the damping zone: one at the horizontal face Γ_{d1} and another at the vertical face Γ_{in}. Wave-information will be introduced through this overlapping zone into the new FE spaces. Next, spatial interpolations will be performed to provide the wave-information more accurately. Let $\mathcal{T}_{d1}$ and $\mathcal{T}_{in}$ represent the Cartesian triangulations of the upper part of the domain Γ_{d1} and the vertical wave input part Γ_{in}, respectively. Accordingly, let $\mathcal{W}_{d1}$ and $\mathcal{W}_{in}$ denote the FE spaces corresponding to the triangulations $\mathcal{T}_{d1}$ and $\mathcal{T}_{in}$, respectively. Note

[1]The implementation of this fluid-fluid coupling algorithm will be clearly evident in the numerical weak form in Section 3.2, which is essential for obtaining solutions with FEM.

that, since ship-induced waves are irregular and highly directional, it is essential to have a sufficiently fine partition in both horizontal directions.

After explaining the general concept of how FEBOUSS wave-information is imposed as a boundary condition on the FSI model, the focus will shift to the implementation of the damping zones in the FSI model and the process of obtaining depth-resolved velocities from the 2D FEBOUSS model. The latter process is not straightforward, as FEBOUSS originally solves for depth-integrated velocities. These topics will be discussed in Subsection 3.1.2 and 3.1.3, respectively. Both aspects have proven to be essential components of the proposed coupling strategy.

3.1.2. Damping zones

The damping zones Ω_{d1} at the inlet and Ω_{d2} at the outlet of the FSI model can be numerically implemented using various artificial wave-damping methods. The purpose of these damping zones is to absorb outwards propagating waves, absorb waves reflected from the membrane and reflections from the domain boundaries, which could lead to spurious effects in the numerical solution. Additionally, the inlet damping zone Ω_{d1} facilitates the gradual ramping of flow quantities using a relaxation function to prevent unwanted impulse-like transient behaviour in the wave-field when feeding the FSI model. For this work, the $\phi_n - \kappa$ type method 5 from Reference [22] has been selected, as it has demonstrated the best performance in a series of tests compared to other damping methods and is successfully applied to the analysis of various floating structures interacting with free surface waves [4][14].

The length of the damping zones is denoted by L_d. The x-coordinate of the end of damping zone Ω_{d1} is represented by $x_{d,in}$, while the x-coordinate of the start damping zone Ω_{d2} is denoted by $x_{d,out}$, both with respect to the local coordinate system of the FSI model. The damping zones Ω_{d1} and Ω_{d2} directly border the inlet surface Γ_{in} and outlet surface Γ_{out}, respectively. Waves in the numerical domain are generated using the Neumann boundary condition specified by Equation 2.2b on boundary Γ_{in}, where u_{in} is extracted from the FEBOUSS model. Additionally, the vertical velocity $w_{in,0}$, which is perpendicular to the Γ_{d1} boundary, along with the free surface-elevation κ, is also enforced and extracted from FEBOUSS.

Given this artificial damping method, the kinematic damped free surface condition at the upper boundaries of the damping zone, Γ_d, particularly at Γ_{d1} and Γ_{d2}, can be expressed as:

$$\mathbf{n} \cdot \nabla\phi = \dot{\kappa} + \mu_2(\kappa - \hat{\kappa}) \quad \text{on } \Gamma_d, \tag{3.1}$$

along with the damped dynamic free surface boundary condition, which reads:

$$\dot{\phi} + g\kappa + \mu_1(\mathbf{n} \cdot \nabla\phi - \mathbf{n} \cdot \nabla\hat{\phi}) = 0 \quad \text{on } \Gamma_d. \tag{3.2}$$

Here, the variables $\hat{\phi}$ and $\hat{\kappa}$ represent the velocity potential and surface-elevation values, respectively, which are enforced at each damping zone. These values are obtained from FEBOUSS at the inlet and set to zero at the outlet. Additionally, the factors μ_1 and μ_2 denote relaxation functions that govern the artificial wave-damping characteristics of the model and depend on the wavenumber k. The factors are defined by the following analytical expressions:

$$\mu_1(x) = \begin{cases} \mu_0 \left[1 - \sin\left(\frac{\pi}{2}\frac{x}{L_d}\right)\right] & \text{if } x_{d,in} < x, \\ \mu_0 \left[1 - \cos\left(\frac{\pi}{2}\frac{x - x_{d,out}}{L_d}\right)\right] & \text{if } x > x_{d,out}, \\ 0 & \text{otherwise,} \end{cases} \tag{3.3a}$$

$$\mu_2(x) = k\mu_1(x). \tag{3.3b}$$

This wave-damping approach offers the flexibility to modify the relaxation characteristics of the model, a critical parameter for fluid-fluid coupling studies. For preliminary analysis, the relaxation parameter μ_0 is set equal to 2.5 for all analysis in this work, as this value has shown stable numerical results in other hydroelastic FSI studies [14].

As previously discussed, the FSI model is based on an FEM approach, which necessitates the formulation of a weak form of the governing equations. In this weak form, the source terms, which simultaneously represent the fluid-fluid coupling terms, are clearly given by the following expression:

$$L([w, v, u]) \doteq \int_{\Gamma_{in}} [\, u_{in} w] \, d\Gamma_{in} + \int_{\Gamma_{out}} [\, u_{out} w] \, d\Gamma_{out} - \int_{\Gamma_{d1}} [\, \mu_{2,in} \hat{\kappa} w - \mu_{1,in} \underbrace{\mathbf{n} \cdot \nabla\hat{\phi}}_{w_{in,0}} (u + \alpha_h w)] \, d\Gamma_{d1} \tag{3.4}$$

In Equation 3.4, the terms that are not yet fully defined will be explained in Subsection 3.2.1. This equation, which involves boundary integrals, shows how the fluid-fluid coupling is mathematically implemented, specifically how the depth-resolved horizontal velocity u_{in}, the vertical velocity at the free surface $w_{in,0}$, and the surface-elevation $\hat{\kappa}$ are incorporated as boundary conditions to the FSI model. For this specific work, the vertical velocity at the outlet damping zone, u_{out}, is set to zero so that it can gradually be dampened by the outlet damping zone.

3.1.3. Reconstruction depth-resolved velocities from FEBOUSS

As previously highlighted, the 2D FEBOUSS wave-generation model and the 3D FSI model solve for different sets of variables. The FEBOUSS model computes depth-integrated velocities P, Q, and surface-elevation κ, while the FSI model, on the other hand, solves for a velocity potential ϕ, membrane deflection η, and surface-elevation κ. From the velocity potential ϕ, depth-resolved velocities in a given direction can be obtained by calculating the corresponding gradients. Before the instantaneous transfer of flow variables from FEBOUSS to the FSI model can take place, and to satisfy compatibility requirements at the coupling interface, the depth-resolved horizontal velocity u_{in} at Γ_{in} must be computed, along with the vertical velocity $w_{in,0}$ at the level of the Γ_{d1} boundary, in accordance with the fluid-fluid coupling boundary conditions outlined in Subsection 3.1.1.

Depth-resolved velocities can be derived from depth-integrated velocities through analytical expressions that involve higher-order spatial derivatives. For a 3D problem, the depth-resolved horizontal velocity u_{in} in the x-direction and the depth-resolved vertical velocity w_{in} in z-direction can be represented using the following parabolic equations [11]:

$$u_{in} = \frac{P}{h+\kappa} + \left(\frac{h^2}{6} - \frac{z^2}{2}\right)\frac{\partial}{\partial x}(\nabla_h \cdot \bar{\mathbf{u}}) - \left(\frac{h}{2} + z\right)\frac{\partial}{\partial x}(\nabla_h \cdot \bar{\mathbf{u}}h), \tag{3.5a}$$

$$\begin{aligned} w_{in} = &-\nabla_h \cdot \bar{\mathbf{u}}h - z(\nabla_h \cdot \bar{\mathbf{u}}) - \frac{zh}{3}(\nabla_h \cdot \nabla(\bar{\mathbf{u}})) + \frac{z}{2}(\nabla_h h \cdot \nabla(\nabla_h \cdot \bar{\mathbf{u}})) \\ &- \frac{z}{6}(h^2 - z^2)(\nabla_h \cdot \nabla(\nabla_h \cdot \bar{\mathbf{u}})) + \frac{z}{2}(h+z)(\nabla_h \cdot \nabla(\nabla_h \cdot \bar{\mathbf{u}}h)), \end{aligned} \tag{3.5b}$$

where $\nabla_h(\cdot) = \frac{\partial(\cdot)}{\partial x}\hat{i} + \frac{\partial(\cdot)}{\partial y}\hat{j}$ and $\bar{\mathbf{u}} = \frac{P}{\kappa+h}\hat{i} + \frac{Q}{\kappa+h}\hat{j}$. For numerical implementation, it is important to note that the analytical expressions provided in Equation 3.5 are defined with respect to $z = 0$, which corresponds to the still-water level.

To discretise the partial differential equations presented in Equation 3.5, FEBOUSS employs a widely used method in computational fluid dynamics: a mesh-free approach based on moving least squares (MLS) for calculating the terms related to the spatial derivatives in the analytical formulation. This method has proven effective in minimising numerical noise in the solution [5]. The theoretical background of the MLS method and its implementation in the FEBOUSS model for accurately obtaining full velocity profiles across the depth are explained in detail in References [24] and [5], respectively.

Now that all essential aspects related to FEBOUSS wave input and fluid-fluid coupling have been covered, the next step in the analysis is to discretise the FSI problem in the following sections to enable numerical simulations.

3.2. Finite element method implementation FSI model

A two-way FSI analysis solves for the structural deformation while simultaneously considering the transformation of incident waves caused by the presence of a structure. For floating structures, this two-way interaction is crucial due to the scale of the problem, resulting in phenomena such as (partial) reflection and hydroelastic dispersion [4][14].

The finite element method is particularly well-suited for modelling this multi-physics problem, as demonstrated by others in coupling potential flow equations with Poisson-Kirchhoff plate equations [14]. In this work, a two-way coupled monolithic FEM formulation will be employed to solve the resulting single, fully coupled system of equations that includes both fluid as solid unknowns. As apposed to partitioned approaches, this method has shown improved numerical stability, strong coupling between the structure and fluid, and allows for the simultaneous solution of the multi-physics problem without requiring (excessive) iterations to resolve the fluid-structure coupling [6].

3.2.1. Weak form formulation

The boundary value problem, formulated in continuous form in Sections 2.2 and 3.1 must be cast into weak form before the finite element method can be applied to solve for the unknowns. Therefore, some additional notation needs to be introduced first.

Let $\mathcal{V}$ denote a functional space in the domain Ω, $\mathcal{V}_{\Gamma_{fs}}$ denote the space for the free surface boundary defined on Γ_{fs}, and $\mathcal{V}_{\Gamma_m}$ denote the space for the boundary between the structure and the fluid defined on Γ_m. The unknown velocity potential field is defined as $\phi \in \mathcal{V}$, with the associated weight function[2] $w \in \mathcal{V}$, the free surface-elevation field $\kappa \in \mathcal{V}_{\Gamma_{fs}}$ with its associated weight function $u \in \mathcal{V}_{\Gamma_{fs}}$, and finally the membrane deflection $\eta \in \mathcal{V}_{\Gamma_m}$ with its associated weight function $v \in \mathcal{V}_{\Gamma_m}$. Note that the functional spaces of the unknowns are defined across different topological dimensions leading to the aforementioned mixed-dimensional problem formulation.

Subsequently, the monolithic weak form of this problem setting can be formulated as: find $[\phi, \eta, \kappa] \in \mathcal{V} \times \mathcal{V}_{\Gamma_m} \times \mathcal{V}_{\Gamma_{fs}}$ such that

$$B([\phi, \eta, \kappa], [w, v, u]) = L([w, v, u]) \quad \forall [w, v, u] \in \mathcal{V} \times \mathcal{V}_{\Gamma_m} \times \mathcal{V}_{\Gamma_{fs}}, \tag{3.6}$$

where the bilinear form B, assuming the structure to be continuous and the membrane boundary condition specified by Equation 2.7 is satisfied, is defined by:

$$\begin{aligned} B([\phi, \eta, \kappa], [w, v, u]) \doteq & \int_{\Omega} [\, \nabla\phi \cdot \nabla w] \, d\Omega - \int_{\Gamma_{fs}} [\, \dot{\kappa} w] \, d\Gamma_{fs} + \int_{\Gamma_{fs}} [\, (\dot{\phi} + g\kappa)\beta_h(u + \alpha_h w)] \, d\Gamma_{fs} \\ & - \int_{\Gamma_m} [\, \dot{\eta} w] \, d\Gamma_m + \int_{\Gamma_m} [\, v(m_\rho \ddot{\eta} + \dot{\phi} + g\eta)] \, d\Gamma_m + \int_{\Gamma_m} [\, \nabla v(T_\rho \nabla\eta + T_\rho \tau \nabla\dot{\eta})] \, d\Gamma_m \\ & - \int_{\Lambda_m} [\, v(\mathbf{n} \cdot T_\rho \nabla\eta + \mathbf{n} \cdot T_\rho \tau \nabla\dot{\eta})] \, d\Lambda_m + \int_{\Gamma_{d1}} [\, \beta_h(u + \alpha_h w)\dot{\phi} - w\dot{\kappa}] \, d\Gamma_{d1} \\ & + \int_{\Gamma_{d2}} [\, \beta_h(u + \alpha_h w)\dot{\phi} - w\dot{\kappa}] \, d\Gamma_{d2} \\ & + \int_{\Gamma_{d1}} [\, \beta_h(u + \alpha_h w)g\kappa - \mu_{2,in}\kappa w + \mu_{1,in}\mathbf{n} \cdot \nabla\phi(u + \alpha_h w)] \, d\Gamma_{d1} \\ & + \int_{\Gamma_{d2}} [\, \beta_h(u + \alpha_h w)g\kappa - \mu_{2,out}\kappa w + \mu_{1,out}\mathbf{n} \cdot \nabla\phi(u + \alpha_h w)] \, d\Gamma_{d2}, \end{aligned} \tag{3.7}$$

and the linear form L, assuming that there is no other external loading other than the wave-induced pressure on the structure, is given by:

$$L([w, v, u]) \doteq \int_{\Gamma_{in}} [\, u_{in} w] \, d\Gamma_{in} + \int_{\Gamma_{out}} [\, u_{out} w] \, d\Gamma_{out} - \int_{\Gamma_{d1}} [\, \mu_{2,in}\hat{\kappa} w - \mu_{1,in}\mathbf{n} \cdot \nabla\hat{\phi}(u + \alpha_h w)] \, d\Gamma_{d1}. \tag{3.8}$$

Contemporary literature underscores that developing a stable monolithic FEM formulation for the analysis of VLFS coupled with free surface waves is not straightforward [14]. To overcome this challenge, dynamic boundary conditions are introduced using a stabilised approach, following the methodology described in Reference [6]. In this method, the weight function is adjusted to $\beta_h(u + \alpha_h w)$, where the parameter α_h is selected based on the time-integration scheme used to ensure coercivity [14] and the parameter β_h controls the influence of the weight function. This results in the stabilised weak form outlined in Equation 3.6. The step-by-step derivation of this weak form can be found in Appendix A.

3.2.2. Spatial discretisation

Consider an FE partition of the three-dimensional domain Ω, denoted by Ω^h. From this partition, corresponding finite-dimensional spaces can be constructed: $\mathcal{V}^h \subset \mathcal{V}$ for the velocity potential, $\mathcal{V}^h_{\Gamma_{fs}} \subset \mathcal{V}_{\Gamma_{fs}}$ for the free surface-elevation, and $\mathcal{V}^h_{\Gamma_m} \subset \mathcal{V}_{\Gamma_m}$ for the membrane deformation. Additionally, new triangulations of the domain boundaries are created, represented by Γ^h_{fs}, Γ^h_m, Γ^h_{in}, Γ^h_{out}, and Γ^h_b. Furthermore, let Λ^h_m denote the set of one-dimensional edges between facets of Γ^h_m. Refer to Figure 3.3a for a representation of these boundaries used to solve the discrete unknowns depicted in Figure 3.3b.

[2] Often also referred to as 'test function' in literature.

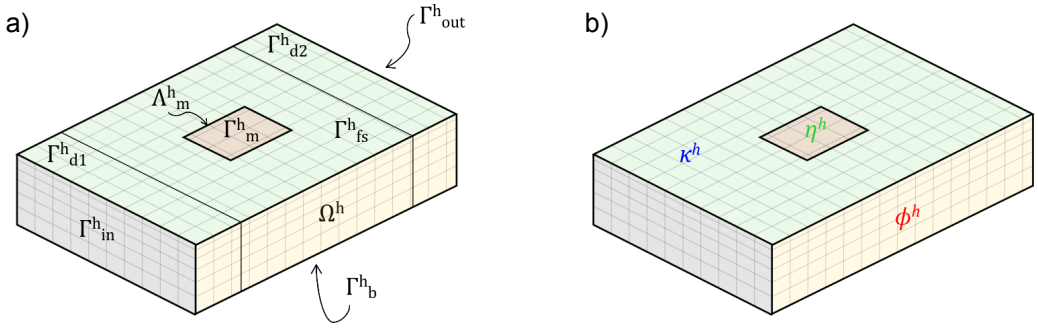

Figure 3.3: a) Schematic of the discretised 3D FSI boundary value problem. b) Representation discretised unknowns.

Subsequently, the spatially discretised problem formulation, which is analogous to Equation 3.6, is defined as follows: find $[\phi^h, \eta^h, \kappa^h] \in \mathcal{V}^h \times \mathcal{V}^h_{\Gamma_m} \times \mathcal{V}^h_{\Gamma_{fs}}$ such that

$$B^h([\phi^h, \eta^h, \kappa^h], [w^h, v^h, u^h]) = L^h([w^h, v^h, u^h]) \quad \forall [w^h, v^h, u^h] \in \mathcal{V}^h \times \mathcal{V}^h_{\Gamma_m} \times \mathcal{V}^h_{\Gamma_{fs}}, \tag{3.9}$$

where the spatially discretised bilinear form B^h can be expressed by adding the superscript h to the unknown field variables, their corresponding weight functions, and the domain boundaries in Equation 3.7. The same approach applies to finding the expression for the spatially discretised linear term L^h, which is analogous to Equation 3.8.

This weak form formulation is based on a continuous/discontinuous Galerkin (C/DG) approach, specifically developed for handling fourth-order operators [17]. In this framework, the shape functions are continuous at the element nodes, while the gradients are discontinuous. The continuity of first-order derivatives is weakly enforced through an interior penalty method. In this work Lagrange polynomials will be employed as shape functions, as demonstrated to perform effectively in Reference [14].

3.2.3. Temporal discretisation

The resulting C/DG formulation given by Equation 3.9 at this stage describes a semi-discrete system of second-order ordinary differential equations, that is, discrete in space and still continuous in time. To find the solution to the transient problem, a time-domain approach based on the Newmark-Beta time discretisation scheme [29] will be applied.

Consider a uniform temporal discretisation with constant time-step Δt. At a given time step $n+1$, with $t_{n+1} = t_n + \Delta t$, an unknown ξ_{n+1}, and its first and second-order time derivatives are given as:

$$\xi_{n+1} = \xi_n + \Delta t \dot{\xi}_n + \Delta t^2 \left[\left(\frac{1}{2} - \beta \right) \ddot{\xi}_n + \beta \ddot{\xi}_{n+1} \right], \tag{3.10a}$$

$$\dot{\xi}_{n+1} = \delta_t \left(\xi_{n+1} - \xi_n \right) + \frac{1-\gamma}{\beta} \dot{\xi}_n + \Delta t \frac{1-\gamma}{2\beta} \ddot{\xi}_n, \tag{3.10b}$$

$$\ddot{\xi}_{n+1} = \delta_{tt} \left(\xi_{n+1} - \xi_n \right) - \frac{1}{\beta \Delta t} \dot{\xi}_n + \frac{1-2\beta}{2\beta} \ddot{\xi}_n, \tag{3.10c}$$

where $\delta_t = \frac{\gamma}{\beta \Delta t}$ and $\delta_{tt} = \frac{1}{\beta \Delta t^2}$. It is important to note that the solution ξ_n, along with its first-order time derivative $\dot{\xi}_n$, and second-order time derivative $\ddot{\xi}_n$, are assumed to be known a priori. The parameters γ and β are weight factors that influence the stability and accuracy of the time-integration scheme. In this work, $\gamma = 1/2$ and $\beta = 1/4$ will be used as the weight factors, as they have been shown to produce a second-order accurate and unconditionally stable numerical scheme. This selection of parameters is referred to as the average acceleration method.

Now that the temporal discretisation scheme has been specified, next the fully discrete problem in the time-domain can be formulated as follows: find $[\phi^h_{n+1}, \eta^h_{n+1}, \kappa^h_{n+1}] \in \mathcal{V}^h \times \mathcal{V}^h_{\Gamma_m} \times \mathcal{V}^h_{\Gamma_{fs}}$ such that

$$B^h_{n+1}([\phi^h_{n+1}, \eta^h_{n+1}, \kappa^h_{n+1}], [w^h, v^h, u^h]) = L^h_{n+1}([w^h, v^h, u^h]) \quad \forall [w^h, v^h, u^h] \in \mathcal{V}^h \times \mathcal{V}^h_{\Gamma_m} \times \mathcal{V}^h_{\Gamma_{fs}}, \tag{3.11}$$

where the fully discretised bilinear form B^h_{n+1} and the linear form L^h_{n+1} can be represented by adding the subscript $n+1$ to the expressions for B^h and L^h from Equation 3.9, respectively.

This concludes the fully discrete well-posed problem formulation, which will be solved in the subsequent chapter. It is worth noting that this numerical formulation is versatile, as it can handle various types of wave inputs, not just those generated by the FEBOUSS wave-generation model.

3.3. Finite element method implementation FEBOUSS

The finite element method is also used to solve the depth-integrated Boussinesq-type equations in space for modelling ship-induced waves, as outlined in Subsection 2.3.1. For this work, a structured triangular mesh is employed, utilising a standard Galerkin approach with a mixed interpolation scheme that combines linear and quadratic shape functions to minimise spurious effects in the numerical solution [31]. While an unstructured mesh might have been more efficient for this large-scale FSI problem, as discussed in Reference [3], this approach still yields robust results. The FEBOUSS model computes the elemental integrals analytically, rather than using traditional Gauss quadrature, to reduce overall computational time requirements.

The time-stepping is performed using the classical Runge-Kutta fourth-order method, with a constant time-step prescribed by the dimensionless Courant-Friedrichs-Lewy (CFL) condition:

$$CFL = max\{\frac{\Delta t}{\Delta r}\sqrt{gh}\}, \tag{3.12}$$

where h represents the still-water depth, g is the acceleration due to gravity, Δr is the characteristic mesh dimension, and Δt is the constant time-step. Since the shallow water wave celerity $c = \sqrt{gh}$ is used, a CFL-number smaller than 1.0 is typically sufficient to ensure stability in the simulation [3]. The iterative solver has a termination criterion based on an absolute tolerance, which, from numerical tests, is set to 10^{-4} for this study. It is important to note that the absolute tolerance significantly impacts the computational time of the solver.

For a comprehensive overview of how the governing FEBOUSS equations are solved, the reader is referred to Reference [3], as the underlying implementation of this method remains unchanged for the purposes of this work.

4

Results and discussion

In this chapter, a series of numerical results are presented to investigate the hydroelastic behaviour of thin floating membranes excited by ship-induced waves, while simultaneously assessing the potential for resonance. The analysis begins with the validation of the proposed fluid-fluid coupling algorithm, as described in Chapter 3, through various tests. Subsequently, the focus shifts to studying waves generated by a moving vessel within a rectangular two-dimensional domain, initially without the presence of a floating structure. Finally, the membrane is introduced into the 3D FSI domain, where its properties, which control the natural frequency of the membrane, are adjusted to align with the peak wave frequencies identified through spectral analysis.

4.1. Transfer of wave-information

In this section, the transfer of wave-information from FEBOUSS to the FSI model within the hybrid modelling framework is examined. The analysis starts with an evaluation of the coupling strategy's performance in Subsection 4.1.1, followed by an assessment of the impact of the input partition in the overlapping zone in Subsection 4.1.2.

4.1.1. Validation 3D fluid-fluid coupling

Before the proposed 3D fluid-fluid coupling algorithm presented in Section 3.1 can be effectively utilised for FSI considerations, it is crucial to rigorously test whether the incident wave is accurately transferred within the hybrid model. The setup for the validation method is illustrated in Figure 4.1. Two sets of simulations will be conducted: the first will involve a full FEBOUSS simulation across the entire domain, while the second will utilise the hybrid model, which couples FEBOUSS with the FSI model, in an empty tank without a structure in the domain. This is important, as the presence of a structure can significantly alter the wave field, as demonstrated in Reference [4].

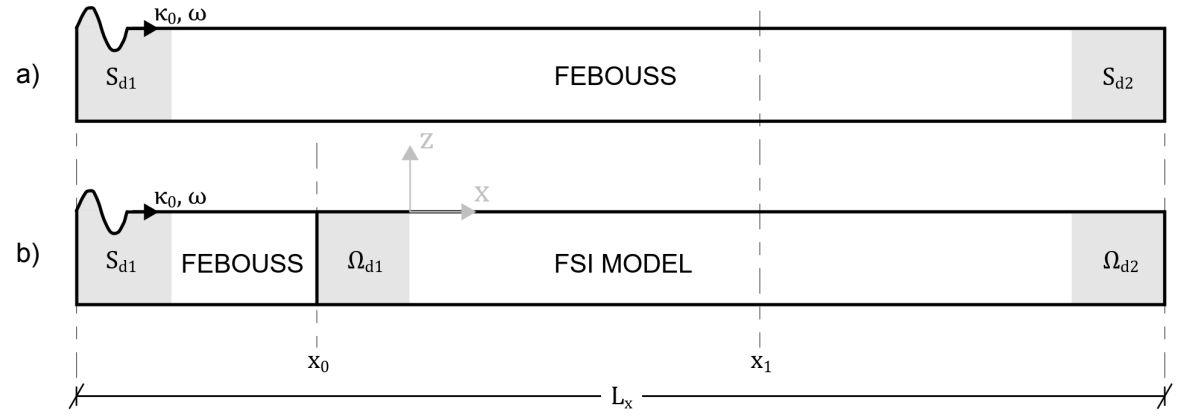

Figure 4.1: a) FEBOUSS wave-generation across entire domain. b) FEBOUSS coupled with empty tank FSI model.

To evaluate the performance of the 3D fluid-fluid coupling strategy, regular monochromatic incident waves with a prescribed wave-amplitude κ_0 and angular frequency ω will be generated using FEBOUSS by numerically solving the governing Boussinesq-type equations, as outlined in Equation 2.9, while excluding the ship wave-generation term. Weakly nonlinear solutions are then obtained through the Fourier series method, as proposed in Reference [26]. In the FEBOUSS model, the waves can freely propagate out of the domain towards the downstream sponge layer S_{d2}. In contrast, the hybrid model couples the fluid domains starting at $x = x_0$, where wave-information is fed into the damping zone Ω_{d1} of the FSI model, allowing the waves to continue propagating in the empty tank until they reach the end of the numerical domain Ω_{d2}. It is essential that the coupling begins only after the waves have propagated a sufficient distance to allow for full development. Additionally, the total length of the simulation domain must be adequately long to accommodate a sufficient number of waves.

The total length of the domain is fixed at $L_x = 240m$ for both scenarios, and the length of the damping zones in the FSI model is set to accommodate the largest wavelength tested, resulting in a fixed value of $L_d = 20m$. The coupling strategy is tested for wave-amplitude $\kappa_0 = 0.1m$, and for wavelengths $\lambda = \{6.3, 12.6, 19.6\}m$, corresponding to wave frequencies $\omega = \{3.1, 2.2, 1.8\}rad/s$. These frequencies are approximated using the linear dispersion relation $\omega = \sqrt{gktanh(kh)}$ for open waters. The free surface-elevation κ is measured at a probe positioned far from the coupling zone, specifically at $x_1 = 70m$. The results of this fluid-fluid coupling validation for different wave characteristics are presented in Figure 4.2, with a total simulation duration of $t_{sim} = 100s$.

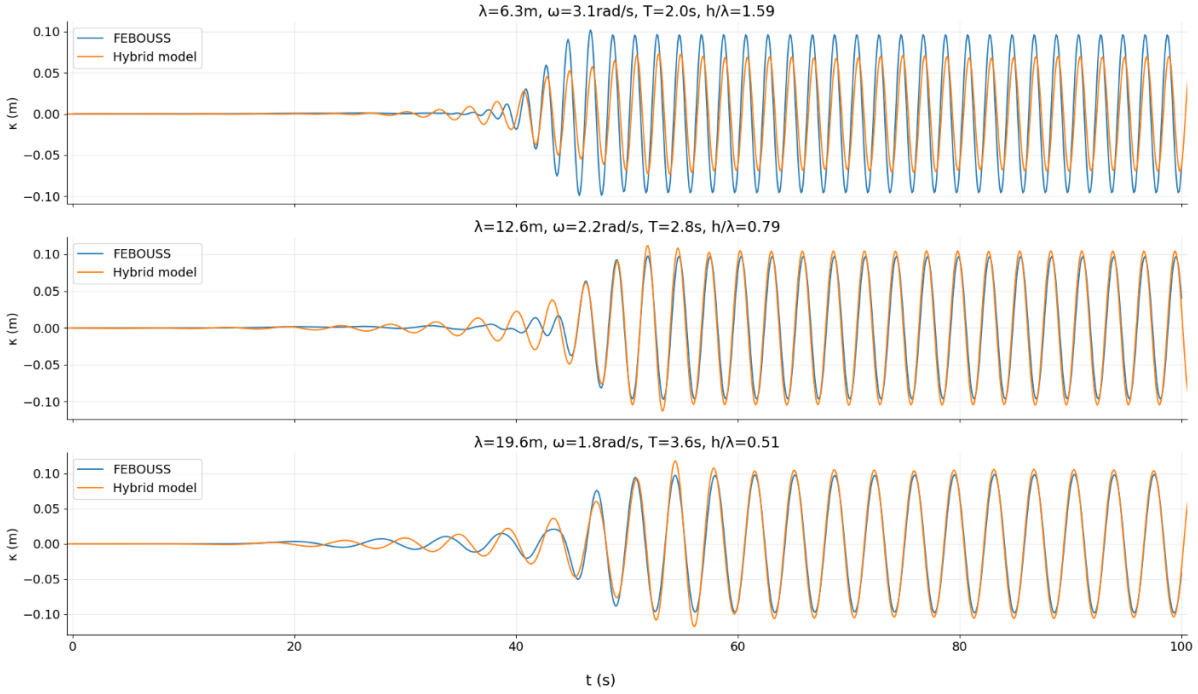

Figure 4.2: Validation fluid-fluid coupling algorithm: transfer wave-information from FEBOUSS to FSI model with regular monochromatic waves with amplitude $\kappa_0 = 0.1m$, measured at probe $x_1 = 70m$ for duration $t_{sim} = 100s$.

The results presented in Figure 4.2 generally demonstrate good agreement between the pure FEBOUSS simulations and the hybrid model in the steady-state regime. However, prior to reaching this regime, significant mismatches in surface-elevation are observed. This could be expected upfront due to the differing time ramping schemes employed by the two models. As the hybrid model begins coupling the waves from FEBOUSS at $x = x_0$ in the FSI model, the signal has been manually shifted to align closely with the harmonic signal, as initially, the coupling involves zero wave-information since the wave signal has not yet reached the coupling zone. Slight mismatches in amplitude peaks are evident, attributed to errors that occur during the transfer of wave-information from the nonlinear wave-generation model to the linear FSI model. Notably, the cases for $\lambda = 12.6m$ and $\lambda = 19.6m$ exhibit small discrepancies, while the short wave case of $\lambda = 6.3m$ seemingly shows the most pronounced errors.

One might argue that the short waves tested could not be accurately transferred with the proposed

coupling algorithm. However, this is incorrect. The short wave case was tested for $h/\lambda = 1.59$, which corresponds to a deep-water case, and the FEBOUSS model becomes invalid after $kh \approx 3$, as shown in Reference [3]. For lower depths, the coupling would have worked well, as demonstrated in the other cases with $\lambda = 12.6m$ and $\lambda = 19.6m$. The coupling strategy shows good accuracy even in deep-water conditions. This highlights the limitations of the current coupling strategy. If the coupling zone length L_d had been increased, even longer waves could have been accommodated in intermediate water depths, which would have worked well due to the successfully tested coupling in deep-water cases. Another approach to reduce the error further is to adjust the damping coefficient μ_0, which was set to a fixed value of $\mu_0 = 2.5$ in this work. However, it is important to note that such adjustments should be made in conjunction with modifications to the damping zone length L_d to properly implement the relaxation functions in the artificial damping method.

Following the validation of wave transfer in the hybrid model, the next step is to assess how the method of introducing wave-information through the input partition in the damping zone affects the numerical results.

4.1.2. Validation convergence coupling zone

The convergence of the fluid-fluid coupling algorithm will be evaluated using the same tank setup and wave characteristics described in Subsection 4.1.1. This validation study involves conducting new simulations that again solve the Boussinesq-type equations for regular monochromatic incoming waves. In contrast to previous validation study, in these simulations, the input partitions N_x, N_y, and N_z in the x, y, and z directions will be progressively refined. The objective is to show that as the partition in the coupling zone becomes finer, the solution converges towards the result obtained from the simulation with the finest partition tested. The results of this analysis are presented in Figure 4.3, where a zoom-in of the surface-elevation κ at a peak in the steady-state regime, between $t = 60.6s$ and $t = 61.0s$, is shown. The total number of feeding particles N in the overlapping zone ranges from $N = 1457$ for the coarsest configuration to $N = 7597$ for the finest partition tested.

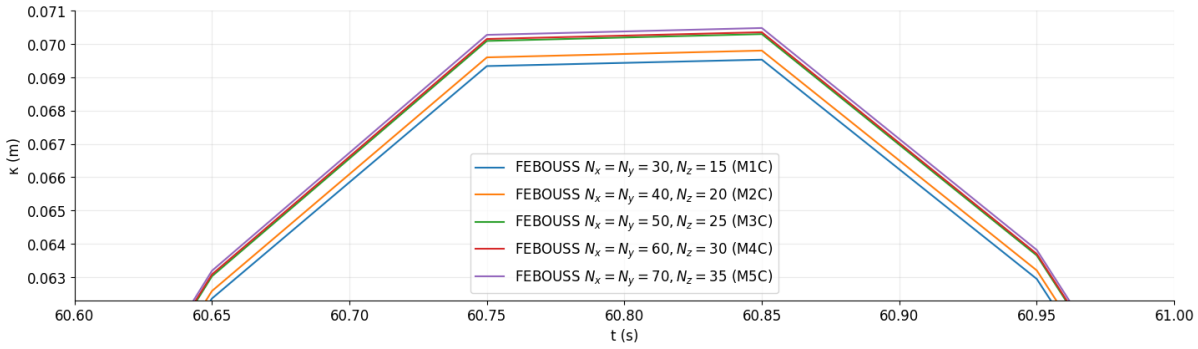

Figure 4.3: Validation coupling strategy with regular monochromatic waves, demonstrated for case with angular frequency $\omega = 3.1rad/s$ and wave-amplitude $\kappa_0 = 0.1m$, zoom-in between $t = 60.6s$ and $t = 61.0s$.

Overall, good agreement is observed for the resulting surface-elevations κ across all mesh configurations. As the partition is refined, the results converge towards those obtained from the finest simulation tested. To further evaluate the convergence of this coupling strategy, a self-convergence study was conducted by comparing the surface-elevation κ from meshes M1C through M4C to the reference surface-elevation κ_{ref} obtained from the finest mesh M5C. The error is quantified using the statistical error parameter $P_d = \sqrt{\sum(\kappa - \kappa_{ref})^2 / \sum(\kappa_{ref})^2}$, where perfect agreement between two signals would result in P_d approaching zero [27]. The results of this analysis in Figure 4.4 demonstrate that as the partition in the overlapping zone becomes finer, the error relative to mesh M5C decreases, confirming the convergence of the fluid-fluid coupling algorithm.

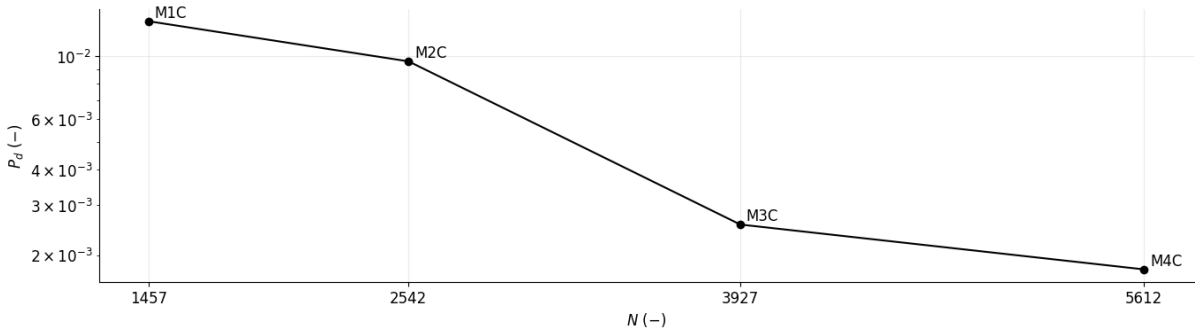

Figure 4.4: Self-convergence study partition in coupling zone with error parameter P_d, partitions M1C-M4C relative to M5C.

With the validation of the fluid-fluid coupling strategy complete, the algorithm can now be confidently employed to study the interaction between ship-induced waves and floating structures in the fluid-structure interaction sections of this chapter.

4.2. Ship-induced waves

In this work, a 2D rectangular domain is employed for FEBOUSS ship-induced simulations. The tank is defined by a total length L_y and a width L_x. Figure 4.5a provides a schematic representation of the problem setup, where initially the presence of a floating structure in the domain is not considered. Ship-induced waves are generated by a moving pressure field that travels in the positive y-direction at a constant velocity v_s, positioned centrally within the domain and following a straight trajectory. Additionally, sufficiently long sponge layers, each with a length of L_a, are implemented along both horizontal boundaries of the domain to effectively absorb the vessel wake and thereby minimise wave reflections.

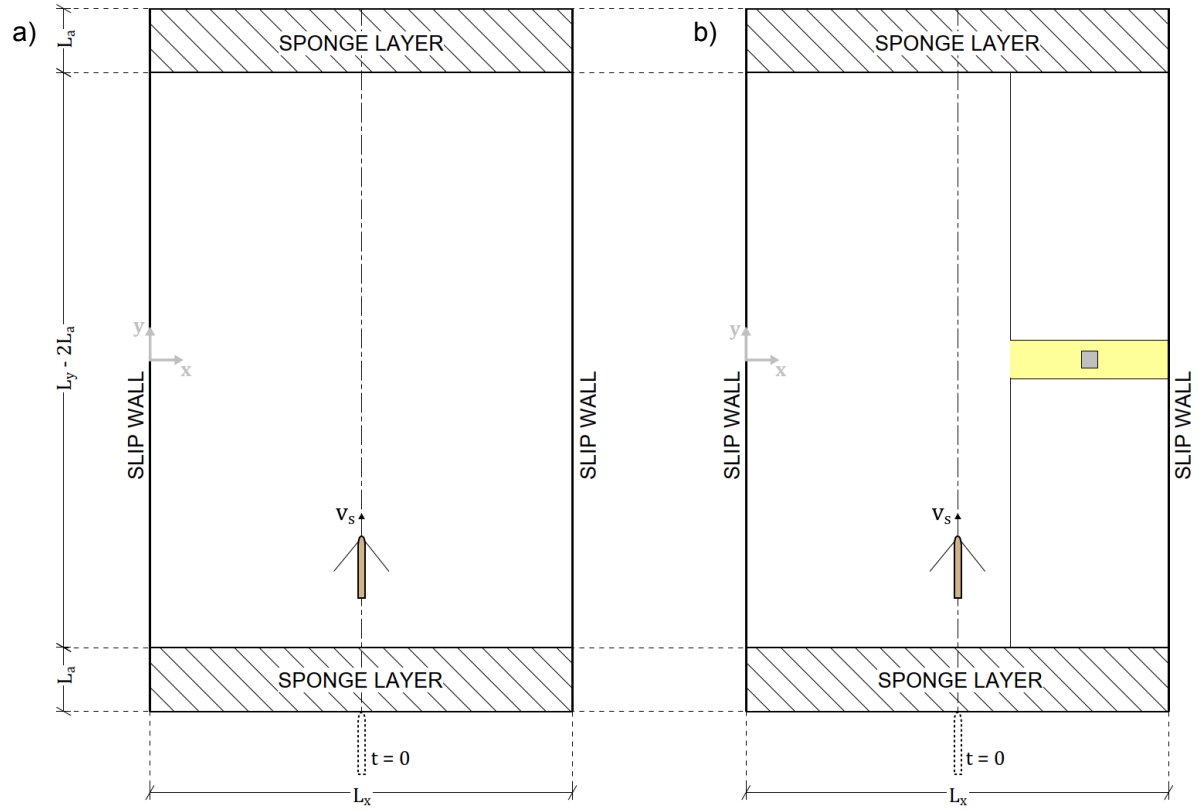

Figure 4.5: a) Schematic problem setting propagation of ship-induced waves in 2D numerical domain. b) Schematic problem setting propagation of ship-induced waves towards floating structure in 3D numerical domain.

The results presented in this chapter are based on a domain with a length of $L_y = 400m$, a width of $L_x = 240m$, and a constant still-water depth of $h = 10m$. The vessel dimensions are set follows: length $L_s = 36m$, beam $B_s = 6m$, and draught $D_s = 1m$. A bulky three-dimensional vessel shape, prescribed by the analytical expressions provided by Equations 2.13 and 2.14, is utilised to model the moving pressure field. The constants used in this configuration are $\alpha_1 = \alpha_2 = 0.7$ and $\beta_1 = 0.4$. The length of the sponge layers is assumed to be at least one ship length, and therefore is fixed at $L_a = 40m$ in this case. Additionally, the vertical side-walls are positioned sufficiently far from the moving disturbance to minimise wave reflections. To avoid spurious transient effects at the start of the wave-generation simulations and to ensure the vessel moves without initial accelerations in initially calm waters, the vessel's starting location is set outside the numerical domain, with its center positioned at coordinate $(L_x/2, -L_y/2 - L_s/2)$.

Based on these specified parameters and principles, several studies on wave propagation and convergence analyses will be conducted in the following subsections. Initially, these will exclusively focus on scenarios where no floating structure is present within the numerical domain. Afterwards, in Section 4.3, the floating structure will be introduced into the numerical domain for studying the final 3D FSI problem.

4.2.1. Mesh convergence study FEBOUSS

The domain is discretised using a structured, regular grid consisting of right-angled isosceles triangular elements. Figure 4.6a illustrates the discretisation of the domain, including the trajectory of the moving vessel. Figure 4.6b provides a zoomed-in view of the region containing the moving pressure field at an arbitrary time-instant, displaying a contour plot of the pressure distribution around the vessel.

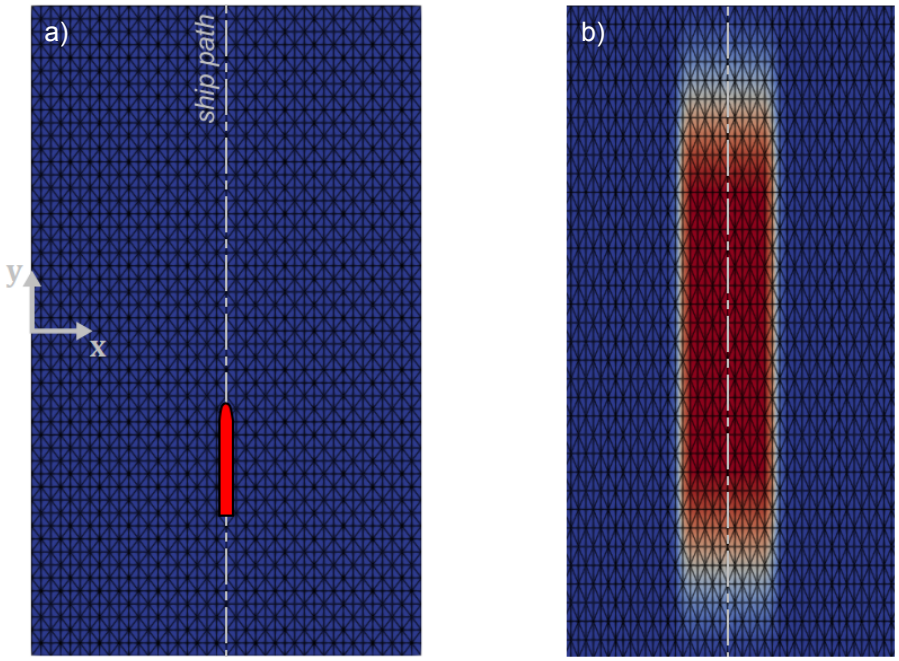

Figure 4.6: a) Illustration discretisation of the 2D numerical FEBOUSS domain. b) Zoomed-in view at location of moving pressure field at an arbitrary time-instant.

A self-convergence study for the FEBOUSS model is conducted using the mesh setups outlined in Table 4.1. The spatial discretisation is reported non-dimensionally, using the beam B_s and length L_s of the ship. M1 represents the coarsest mesh tested, while M5 represents the finest, with progressively finer meshes used in between. In this mesh convergence study, a constant time-step of $\Delta t = 0.05s$ is maintained, resulting in CFL-numbers ranging from 0.50 to 1.24.

Setup	$B_s/\Delta x$	$L_s/\Delta y$	CFL	Number of elements
M1	6.00	36.00	0.50	192 000
M2	8.00	36.00	0.66	256 000
M3	10.00	36.00	0.83	320 000
M4	12.00	36.00	0.99	384 000
M5	15.00	36.00	1.24	480 000

Table 4.1: Details simulation setups for the mesh convergence study for FEBOUSS simulations.

To ensure a stable numerical method, it is essential to use an adequate number of elements to accurately capture the shape of the moving pressure field in both the beam and length directions of the ship. Overly coarse meshes can lead to divergent solutions in the wave field. The surface-elevation κ is measured along the domain's centerline at $x = 120m$ at time-instant $t = 45s$ using all mesh configurations, with results presented in Figure 4.7. Visual inspections indicate that meshes M1 through M3 tend to convergence towards the results obtained with mesh M5, while mesh M4 appears to have already converged. The resolution of the mesh significantly impacts computational time. Therefore, finer meshes should only be utilised in scenarios where precision is critical. The nearly overlapping surface-elevation results from meshes M4 and M5 at the peak around $y = 42m$ illustrate this convergence visually, as shown in Figure 4.7c.

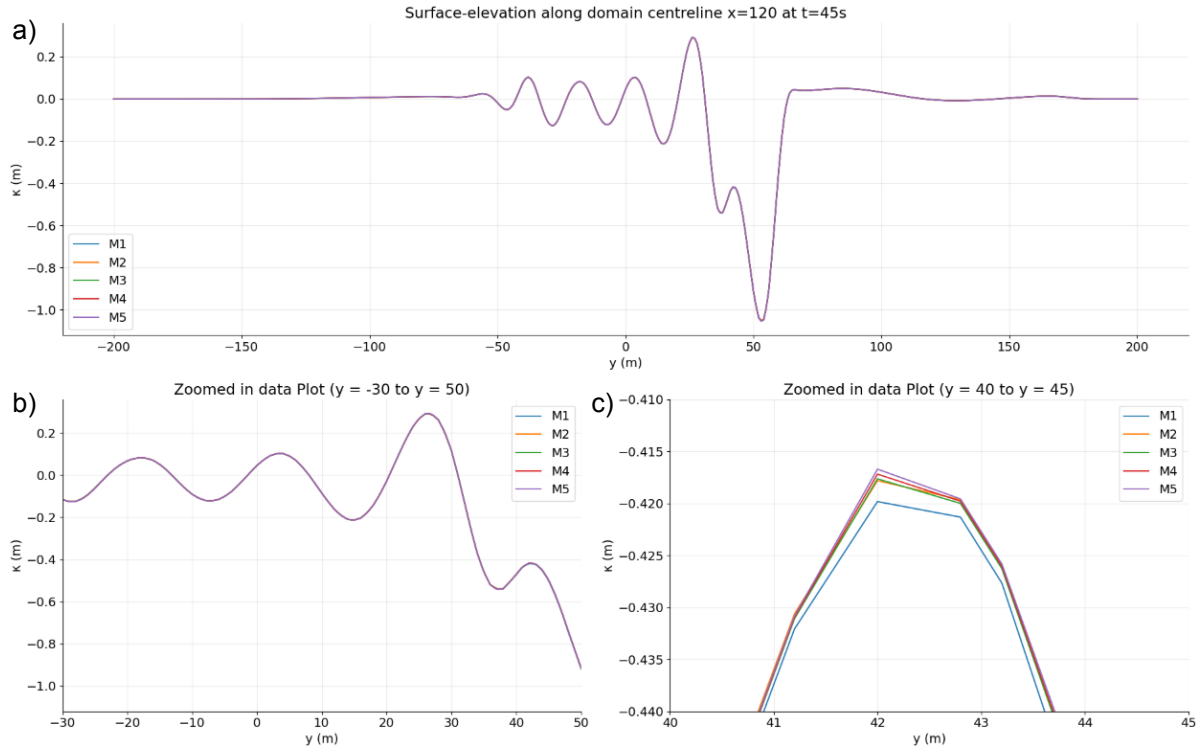

Figure 4.7: a) Spatial evolution of the surface-elevation at a fixed time-instant for the FEBOUSS mesh convergence study. b) Zoomed-in view at segment of domain to visually check for mesh convergence. c) Zoom-in at location of peak.

In addition to the visual comparison of the results, the rate of self-convergence is further quantified using the same statistical error parameter as described in Subsection 4.1.2. The surface-elevation κ obtained from meshes M1 through M4 is compared with the reference surface-elevation κ_{ref} from the reference setup M5, and the results are presented in Figure 4.8.

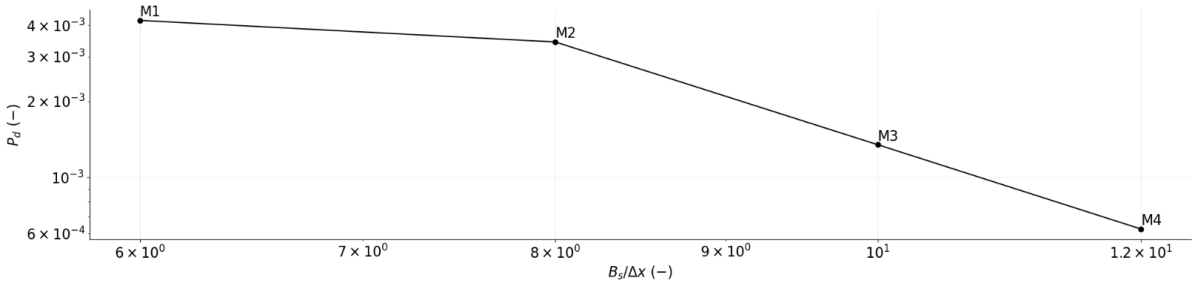

Figure 4.8: Quantification of self-convergence through error parameter P_d, comparison mesh setups M1-M4 relative to M5.

From the P_d error parameter results, it can be observed that the obtained surface-elevation values are highly accurate due to the large number of elements used. It is important to note that further refining the mesh for this structured, regular grid could theoretically reduce the error margin even more, but this would come at a high computational cost.

A more efficient approach, as demonstrated by others in Reference [3], involves using variable mesh resolutions across the domain. This strategy eliminates the need for a uniformly fine grid throughout the entire domain by applying coarser meshes in areas where the ship does not pass, thereby optimising the spatial distribution of elements in the finite element method. This approach is particularly useful when dealing with larger domains. However, the implementation of these variable mesh configurations is beyond the scope of this thesis.

4.2.2. Time convergence study FEBOUSS

The influence of refining the time-step Δt is investigated here for the probe located at $x = 120m$ and $y = 0m$, representing the probe at the center of the simulation domain. The results of this analysis are summarised in Table 4.2. The surface-elevations resulting from setups T1-T3 have been compared to those from test setup T4, which has the smallest time step. The sufficiently fine spatial discretisation setup M1, obtained from Subsection 4.2.1, has been used for this time-convergence analysis and will also be used throughout the remainder of this report.

Setup	Δt	CFL	P_d
T1	0.05	0.50	4.754e-5
T2	0.025	0.25	1.695e-5
T3	0.02	0.20	2.925e-5
T4	0.01	0.10	-

Table 4.2: Table with setup time convergence analysis and results.

This analysis shows that refining the time-step results in very limited changes in the surface-elevation, as the solution for the surface-elevation already looks converged from the biggest time-step. Hence, the CFL-number condition given in Section 3.3 produces stable numerical results, making setup T1 suitable for efficient numerical simulations.

4.2.3. Influence distance to moving pressure field

The first aspect of the propagation of ship-induced waves considered here involves analysing the influence of the moving pressure field's distance relative to specific spatial points, focusing on how surface-elevations at these probes are affected as a ship passes increasingly closer and how the waves develop over time. To achieve this, surface-elevations are monitored at various probes located outside the sponge layers. The y-position of the moving ship over time, along with the time-series of the surface-elevation and the corresponding amplitude spectra, are presented in Figure 4.9.

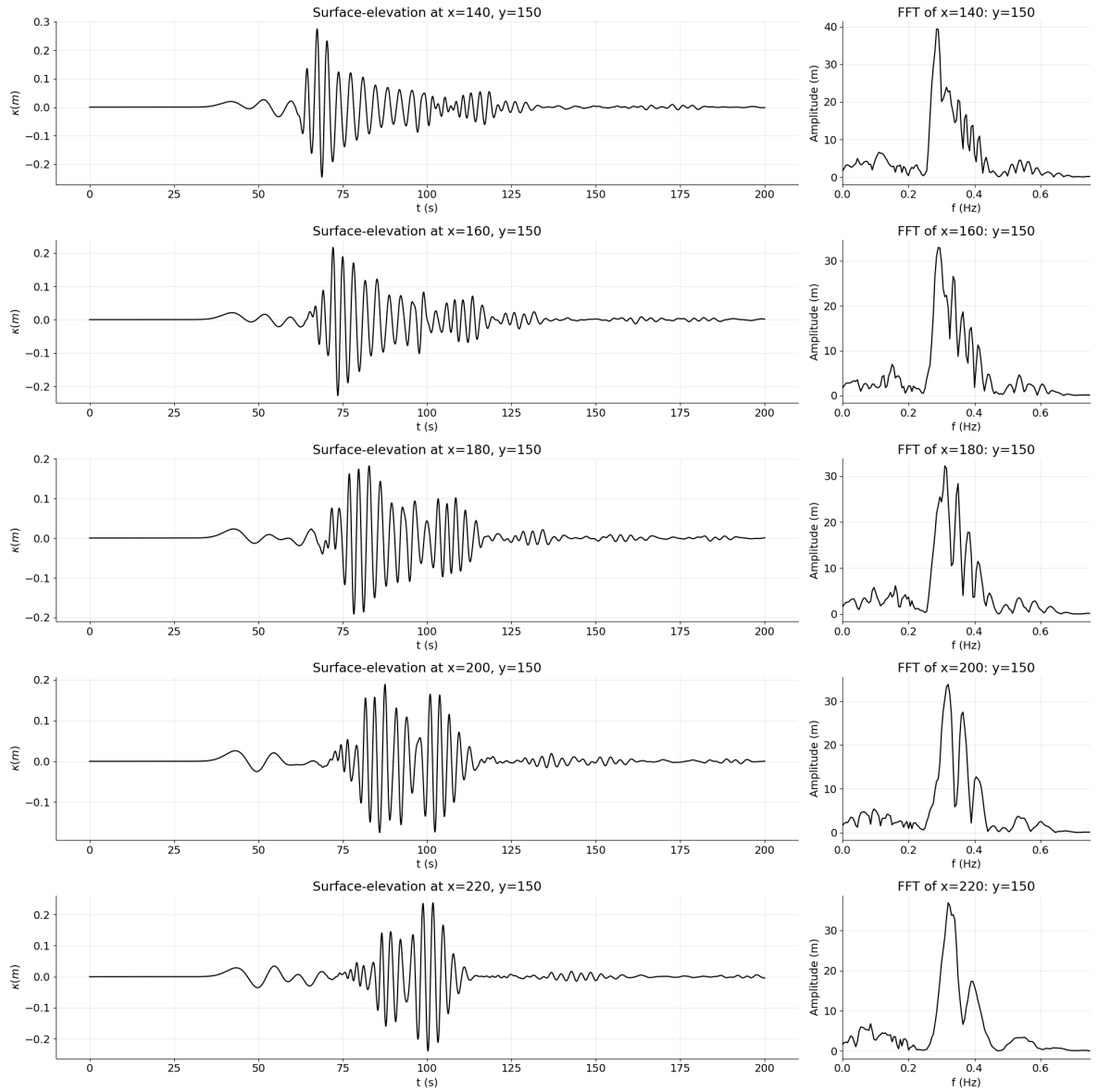

Figure 4.9: Time-series surface-elevation κ and the corresponding spectra illustrating the development of waves at different probes, with vessel moving at a depth-Froude number of $Fr_d = 0.6$.

The probes have been placed along one symmetric part of the (x, y)-plane, with only 5 reported here: for a fixed $y = 150m$ at corresponding $x \in [140, 160, 180, 200, 220]$, while the ship's path remains fixed. The ship-distance study has been conducted over a total simulation duration of $t_{sim} = 200s$, using a constant time-step of $\Delta t = 0.05s$. The domain is discretised with a grid spacing of $\Delta x = 1m$ and $\Delta y = 0.5m$, which have been shown to produce relatively fast and stable numerical results, albeit at the costs of some accuracy, as discussed in Subsections 4.2.1. Furthermore, for this simulation, the ship is moved at a fixed constant speed of $v_s = 4.202m/s$, representing a depth-Froude number of 0.6.

Initial observations of the results show that wave-trains with large wave heights occur at time-instances when the ship's y-location closely aligns with the y-location of the probe of interest. In front of the wave-trains, small oscillations in the surface-elevation are observed. Physically, this represents minor disturbances in the still-water level remaining after the ship has passed away, which ultimately diminish to zero. Additionally, it is observed that the wave heights are greatest when the distance in x-direction between the moving pressure field and the nearest probe is minimal. This conforms the importance of placing floating structures sufficiently far from ship traffic to avoid exciting a structure with large wave-heights.

Additionally, the time-series in Figure 4.9 show that there are two components of the wave: one at the front and one at the back. The front wave is still developing as it continues to lengthen over time, while the waves behind form a fully developed wave-train after propagating over a sufficiently long distance. This development is observed by the steady wave-train being merely time-shifted from one probe to the next probe without significant differences in the surface-elevation pattern measurements.

From visual inspection can be concluded that at $x = 140m$ the waves represent a developing wave train, while the waves from $x = 200m$ onwards show more developed behaviour after a certain period of time. Although the rate of wave development can be visually inferred from 2D contour plots of surface-elevation at different time instances, a different approach is employed here for a more qualitative analysis. This method will be useful later when introducing the floating structure into the numerical domain. The rate of wave development is further analysed using spectral analysis, specifically by examining the amplitude spectrum obtained from a fast Fourier transform (FFT) of the surface-elevation. The results for the case where the ship is moving at a fixed depth-Froude number of 0.6 are presented in the second column of Figure 4.9. The results of these FEBOUSS simulations are shown for the same aforementioned placed probes in the simulation domain.

Figure 4.9 reveals a distinct peak frequency around $f = 0.3Hz$, with a secondary peak observed at $f = 0.4Hz$, indicating the dominant frequencies present in the signal for this particular case. The wave development is inferred from the fairly well-matching amplitude spectrum results, especially as surface-elevation is measured closer to $y = 150m$. However, some discrepancies in amplitude are evident, likely because of the wave reflections from the side walls and the restricted length of the domain in both directions, which constrains the waves from fully developing. It is noteworthy that the amplitude spectrum will exhibit variations in peak frequencies when the ship's speed is adjusted. This analysis supports the conclusion that the selected domain is appropriate for ship-wave propagation analysis later in this thesis.

4.2.4. Influence velocity of moving pressure field

The second set of numerical tests, conducted within the same problem setting, varied the speed at which the disturbance is moving. The ship speed is reported non-dimensionally using the depth-Froude number defined by $Fr_d = v_s/\sqrt{gh}$, with tests ranging from $Fr_d = 0.6$ to $Fr_d = 1.4$, corresponding to ship speeds from $v_s = 5.943m/s$ to $v_s = 13.866m/s$, respectively.

In Figure 4.10, contour plots illustrate the surface-elevation at a fixed ship location ($y = 100m$), revealing considerably different patterns in the wave field results. To obtain the wave field results for varying the speeds presented in Figure 4.10, the same spatial and temporal discretisation was used as is done in Subsection 4.2.3. Below a depth-Froude number of approximately $Fr_d = 0.9$, the transverse wave system remains clearly noticeable. However, above this value, the transverse system disappears and is replaced by divergent waves. Physically, this transition occurs because the balance between the velocity of the moving disturbance and the shallow water wave celerity strongly determines the governing wave regime. Up to $Fr_d = 1.0$, the Kelvin wave angle is clearly visible in the contour plots. In deep-water cases, this angle increases to 90 degrees in the limit as the depth-Froude numbers increase. For Fr_d values higher than 1.0, the Kelvin wave angle drops back to smaller values due to the rapid propagation of divergent ship-induced waves. When the shallow water wave celerity and ship speed are approximately equal, significant surface-elevations and gradients in the wave field are observed. This is because both transverse and divergent waves dominate and amplify each other.

The wide variety of possible wave fields arising from the presence of a moving pressure field has also been observed by other researchers [9]. Furthermore, studies have confirmed the relationship between the Kelvin wave angle and the dominance of transverse or divergent waves at different depth-Froude numbers by establishing analytical expressions [20].

With the different wave field patterns observed for various depth-Froude numbers, the next objective of this analysis is to investigate how these distinct wave fields interact with a floating structure within the domain. This FSI study will be conducted in Section 4.3, focusing specifically on the scenario where a moving vessel generates waves that propagate into a narrow inlet waterway.

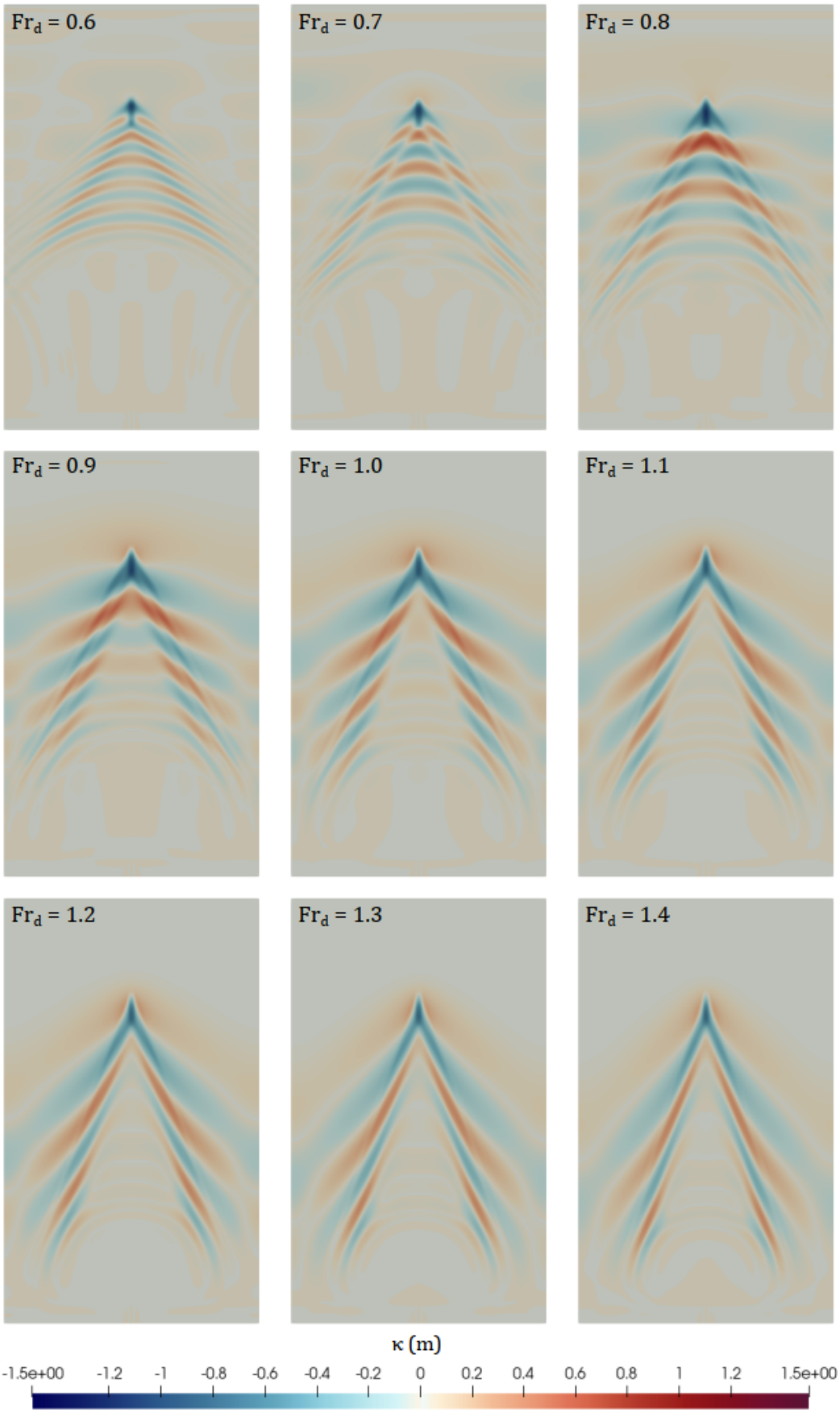

Figure 4.10: Contour plots of surface-elevation κ with different ship speeds at different time-instants, showing different patterns in the wave field.

4.3. Implementation hydroelastic analysis

The FEBOUSS domain and problem setup for wave propagation studies remain consistent with the approach used in Section 4.2, but now incorporate the floating structure within the hybrid model framework for the hydroelastic analysis. Figure 4.5b illustrates the problem setup for modelling the interaction between ship-induced waves and floating structures. It is important to note that in this thesis, wave input is considered only from one face for the FSI model, with side walls placed along the entire length of the simulation domain.

The notation for the hybrid model variables follows the description outlined in Chapters 2 and 3. The water depth is set to $h = 10m$, with the domain dimensions defined as $L_\Omega = 90m$ for the length and $W_\Omega = 20m$ for the width. The structural analysis assumes a square, thin elastic membrane with dimensions $L_m = W_m = 12m$. To absorb the waves on both sides of the tank and to give in wave input to the FSI model from FEBOUSS, square damping zones with a length of $L_d = 20m$ are used. The mass parameter of the membrane is set to $m_\rho = 0.9$, and the tension parameter in the membrane, T_ρ, is varied depending on the specific application under consideration.

Spatial discretisation of the FSI domain is performed using a Cartesian grid with second-order hexahedral elements in all simulations. Uniform discretisation is applied in the Δx and Δy directions, while the Δz discretisation varies. The height of the vertical elements increases exponentially with depth, which allows for enhanced resolution near the free surface, while enabling a coarser mesh near the bottom. This mesh configuration is computationally efficient, providing finer resolution where needed most. A schematic of the spatially discretised problem is shown in Figure 3.3.

Before analysing the hydroelastic response of the floating structure to ship-induced waves in 3D, a mesh convergence study and a time convergence study of the FSI model will first be conducted in Subsections 4.3.1 and 4.3.2, respectively. Additionally, an approach to quantifying the natural frequencies of a membrane will be highlighted in Subsection 4.3.3.

4.3.1. Mesh convergence study FSI model

The spatial convergence analysis for the FSI model is carried out by examining the deformation of a section of the 2D floating membrane subjected to linear monochromatic waves in the time-domain, as described by Airy's linear wave theory [21]. For this analysis, the meshes are progressively refined for each simulation, following the mesh setups outlined in Table 4.3. The partitions n_y and n_z in the y and z directions, respectively, remain fixed during these simulations, as the validation is carried out with monochromatic, unidirectional waves. The simulation will run for $t_{sim} = 75s$, which is sufficient to ensure that a steady-state solution is reached within this time frame.

Setup	Δx	Δy	Δz	n_x	n_y	n_z	Number of elements
M1FSI	1.00	2.00	0.38 - 1.98	90	10	10	9 000
M2FSI	0.50	2.00	0.38 - 1.98	180	10	10	18 000
M3FSI	0.25	2.00	0.38 - 1.98	360	10	10	36 000
M4FSI	0.20	2.00	0.38 - 1.98	450	10	10	45 000

Table 4.3: Details of mesh configurations for the mesh convergence study FSI model, note that the height of the mesh in vertical direction Δz varies over depth.

The deformation of the membrane η is plotted along the domain center line at $y = 0m$ for all the same parameters, with the mesh configuration as the only variable, based on the mesh setups from Table 4.3. The results of this analysis are presented in Figure 4.11, where a snapshot of the membrane's deformation is shown at time-instant $t = 42.0s$. The tension in the membrane is set to $T_\rho = 35.316$, which is relatively low, allowing for considerable hydroelastic deformations. The regular incoming linear waves to which the floating membrane is exposed have an angular frequency of $\omega = \frac{2\pi}{3} rad/s$, and wave-amplitude $\kappa_0 = 0.1m$.

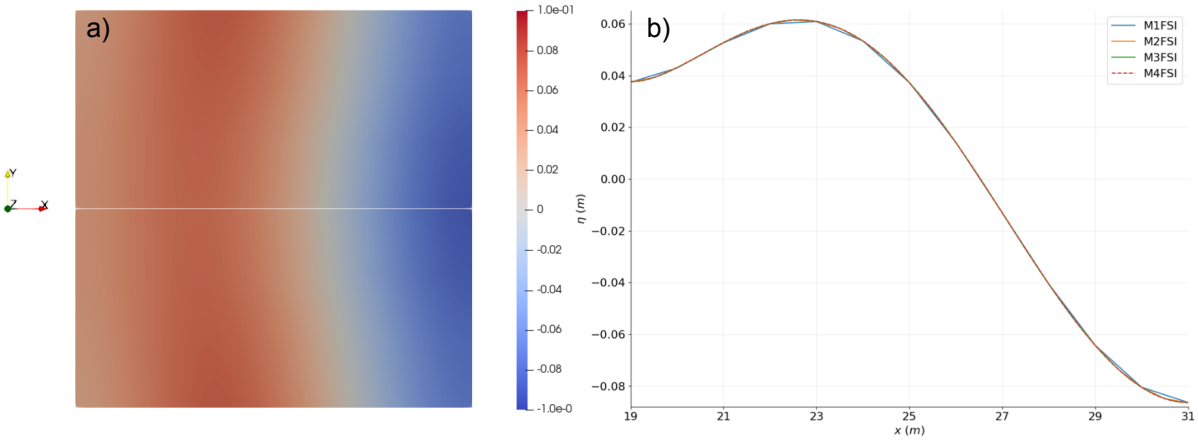

Figure 4.11: a) 2D contour plot deformation membrane at $t = 42.0s$ with white horizontal line depicting center line $y = 0m$. b) 1D plot corresponding deformation membrane along the center line.

Based on the results for the membrane deformation in Figure 4.11b, the model mesh appears to have converged from mesh M1FSI onwards already. Therefore, this mesh can be used for subsequent FSI simulations. The time-step for these simulation was fixed at $\Delta t = 0.1s$, and the effect of refining the time-step will be explored in the next part of the analysis in Subsection 4.3.2.

4.3.2. Time convergence study FSI model

Now that the mesh convergence of the FSI model is completed, the temporal convergence will be tested by examining the deflection of a probe on the membrane. This deflection will be measured at the corner point with coordinates $(19.0, 6.0, 0.0)$. For this test, mesh M1FSI from Subsection 4.3.1 will be used, as it has proven to be both efficient and sufficiently accurate. The setup for this test is identical to the one used in Subsection 4.3.1, with the only difference being that the time-step Δt is varied for the following time-step discretisations: $\Delta t = \{0.2, 0.1, 0.05, 0.025\}s$. The resulting time-series of the deflection is displayed in Figure 4.12a. From Figure 4.12b, it can be concluded that the results converge for time-steps smaller than $\Delta t = 0.1s$.

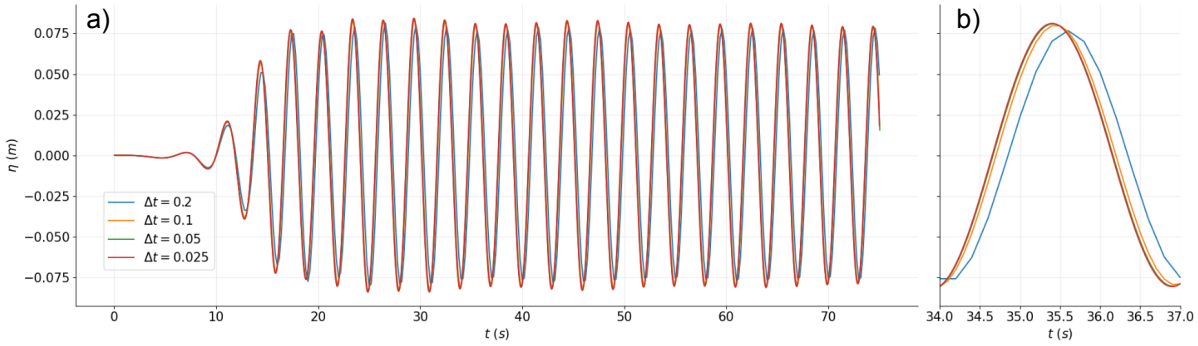

Figure 4.12: Time-series deflection left corner point floating membrane at coordinate $(19.0, 6.0, 0.0)$.

With convergence in both space and time verified, the analysis now progresses to the first steps of examining the hydroelastic behaviour of floating structures under ship-induced waves, focusing on the quantification of the natural frequencies of a thin elastic membrane. Section 4.4 will finally explore the model's response to this complex wave forcing.

4.3.3. Natural frequencies membrane

The analysis in the following section requires information about the natural frequencies of the floating membrane. In reality, when a body vibrates in water, the surrounding fluid is also accelerated, and the hydrostatic-gravitational stiffness influenced by the water-plane area becomes significant. This concept

is known as added-mass in computational fluid dynamics. The approach taken here is to use wet modal analyses. A comprehensive overview of determining the wet natural frequencies and modal shapes of materially damped floating membranes has been provided in Reference [4]. Typically, the wet natural frequency of a structure is lower than its dry natural frequency, indicating (strong) added-mass effects.

Although wet modal analysis provides a more realistic representation of the actual natural frequencies of the membrane, the presence of the surrounding fluid will be neglected here for finding the natural frequencies of the structure. This approximation allows the natural frequencies of free vibration of the membrane to depend solely on the material properties and geometry of the structure. For the free-vibration analysis, free-edge boundary conditions are assumed, as described by Equation 2.7. The analytical expression for determining the dry natural frequencies of a finite, materially undamped, 1D floating membrane for mode number n is given by:

$$\omega_n^d = n\pi\sqrt{\frac{T_\rho/L_m^2}{m_\rho}}, \tag{4.1}$$

where T_ρ is the tension parameter, L_m is the length of the membrane, and m_ρ is the mass parameter. The natural frequencies of the membrane will be calculated for various tension values to obtain different natural frequencies in the the analysis of ship-induced waves interacting with floating membranes, which will be discussed in the following section.

4.4. Ship-induced waves interacting with floating membranes

The final part of this thesis examines the hydroelastic response of the floating structure when subjected to ship-induced waves using the proposed one-way partitioned fluid-fluid coupling algorithm. This section begins by quantifying the incoming wave characteristics at the inlet of the FSI model. It then proceeds with the hydroelastic analysis of a thin floating membrane, exploring how it responds to these complex waves as they propagate into a narrow FSI domain, where the floating structure is located.

4.4.1. Measurements incoming waves

To obtain information about the incoming wave characteristics propagating from the FEBOUSS wave-generation model through the coupling zone into the FSI model, a probe P_0 is placed at the inlet of the FSI model. This probe measures the incoming surface-elevation κ, as shown in Figure 4.13. Wave-information is transferred from FEBOUSS to the FSI model through the adjacent coupling zone, as illustrated in the schematic for the ship-induced waves interacting with floating structures scenario in Figure 4.5b. The same tank dimensions and model properties as previously validated in Section 4.3 are used for this series of analysis.

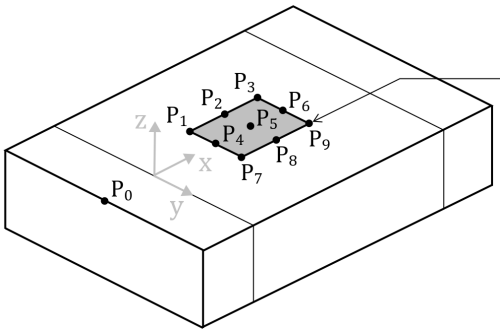

Probe	x	y	z
P_0	-20.0	0.0	0.0
P_1	19.0	6.0	0.0
P_2	25.0	6.0	0.0
P_3	31.0	6.0	0.0
P_4	19.0	0.0	0.0
P_5	25.0	0.0	0.0
P_6	31.0	0.0	0.0
P_7	19.0	-6.0	0.0
P_8	25.0	-6.0	0.0
P_9	31.0	-6.0	0.0

Figure 4.13: The location of the probes $P_0 - P_9$, where incoming wave characteristics at the inlet, surface-elevation κ in empty tank, and membrane deflection η in FSI model will be measured.

The surface-elevation time-series κ and their corresponding spectra are shown in Figure 4.14 for depth-Froude numbers $Fr_d = \{0.6, 0.9, 1.2\}$, which, as discussed in Subsection 4.2.4, produce a diverse range of wave field patterns. Further results for additional depth-Froude numbers, $Fr_d = \{0.6, 0.7, ..., 1.4\}$, can be found in Appendix B. The FEBOUSS model is run for a total simulation duration of $t_{sim} = 200s$, while the FSI model runs for $t_{sim} = 175s$. To ensure compatibility between the two models, both simulations use the same constant time-step of $\Delta t = 0.05s$.

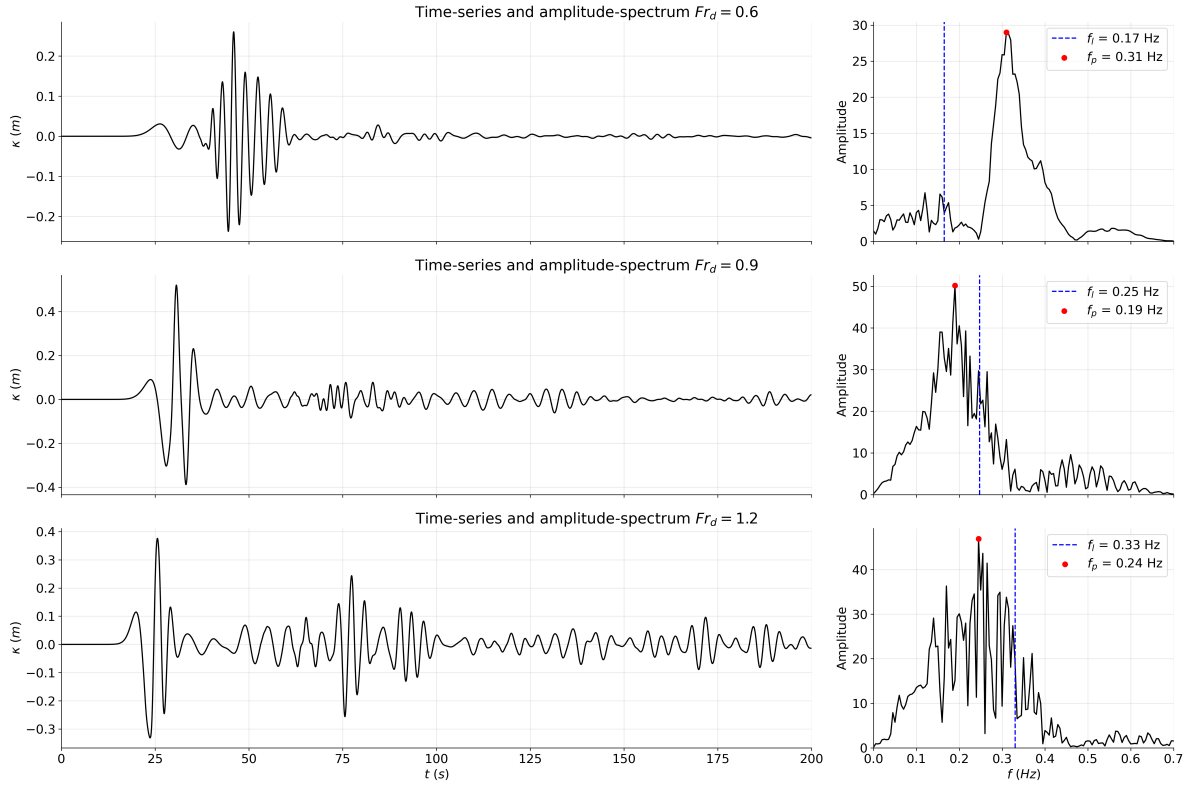

Figure 4.14: Surface-elevation κ at inlet probe P_0 of the FSI model, plotted for $Fr_d = \{0.6, 0.9, 1.2\}$.

The results for the incoming wave characteristics, shown in Figure 4.14, initially reveal long waves entering the FSI domain, followed by a short, highly irregular wave train with relatively large wave heights. The varying ship speeds result in different wave field behaviours, as previously noted. Notably, in the higher depth-Froude number cases, large oscillations are observed after the wave train passed. This phenomenon is primarily due to the interference between ship-generated waves and waves reflected from the walls of the FEBOUSS model. This observation is supported by the corresponding spectra for the higher depth-Froude number cases, which exhibit a broader range of frequencies compared to the lower depth-Froude number cases. To provide a point of reference, the frequency of a linear wave propagating at the celerity of the corresponding ship velocity, denoted as f_l, is plotted in the amplitude-spectrum graphs, where the wavelength λ is approximated by the length of the moving ship, $L_s = 36m$. For lower depth-Froude numbers, the peak weak frequency f_p is underestimated, while for higher depth-Froude numbers, it is overestimated.

To further investigate the characteristics of the incoming waves, the maximum wave heights for each depth-Froude number Fr_d, defined as $H_{max} = \kappa_{max} - \kappa_{min}$, are reported. The results are presented in Figure 4.15 for the full range of depth-Froude numbers, which are provided in Appendix B. Here, κ_{max} represents the maximum surface-elevation in the signal, and κ_{min} denotes the minimum surface-elevation observed. The results show that the largest wave heights occur at depth-Froude numbers where the vessel's velocity v_s nearly matches the shallow water wave celerity $c = \sqrt{gh}$, specifically at $Fr_d = 0.9$. At this point, a transition in wave field patterns occurs, where combination of both transverse and diverse waves is replaced by only divergent waves due to the relatively rapid ship movement. Beyond this transition, for higher depth-Froude number cases, the maximum wave height begins to decrease and eventually levels off, converging towards a plateau.

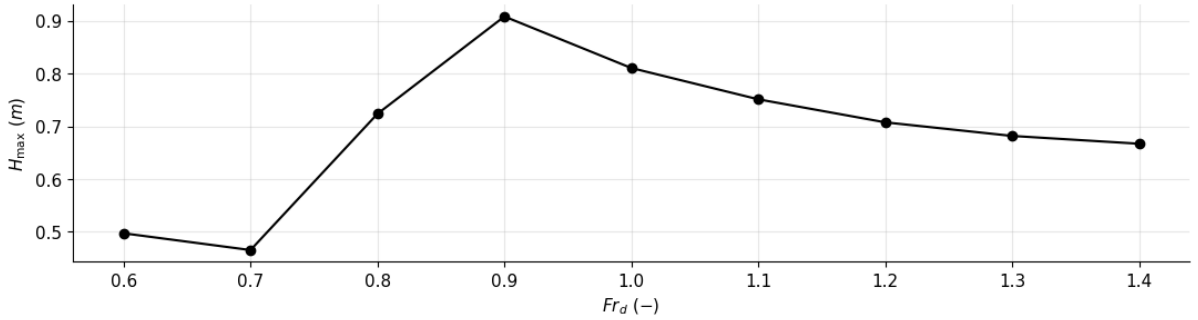

Figure 4.15: The maximum measured wave height H_{max} for each depth-Froude number at the inlet probe P_0.

Now that the incoming waves have been investigated, the focus of the analysis will shift to the deflection of the floating membrane in response to the resulting wave field generated by the vessel, which will be discussed in detail in the subsequent subsection.

4.4.2. Measurements surface-elevation and deflection membrane

The next step in the analysis examines the deflection η of the floating membrane in response to the incoming waves. The membrane deflection is measured at probes $P_1 - P_9$ within the FSI model, with their locations shown in Figure 4.13. The deflections at these probes are compared to the surface-elevation κ obtained from an empty tank model at exactly the same probes, exposed to the same ship-generated wave conditions as applied to the FSI model with the membrane. The results of this hydroelastic study are presented for the ship-wave cases with depth-Froude numbers $Fr_d = \{0.6, 0.9, 1.2\}$, with the corresponding results shown in Figures 4.16, 4.17, and 4.18, respectively. For a complete set of hydroelastic behaviour for other depth-Froude number cases tested, refer to Appendix C.

In many applications, resonance is a critical physical phenomenon as it can lead to excessively high stresses and deformations in a structure. Therefore, the results presented in Figures 4.16, 4.17, and 4.18 focus on quantifying the potential for large hydroelastic responses caused by the variety of incoming waves acting on the structure. To assess this, the dry natural frequency ω_n^{dry} of the membrane, as defined by Equation 4.1, is aligned with the peak wave frequency f_p present in the wave signal generated by the ship's movement at depth-Froude numbers $Fr_d = \{0.6, 0.7, ..., 1.4\}$. These peak frequencies are obtained through spectral analysis, specifically by performing an FFT on the time-series data from probes $P_1 - P_9$. In order to explore different natural frequencies, the tension parameter T_ρ of the membrane is adjusted for each scenario tested. This theoretically enables an evaluation of large membrane hydroelastic responses to the incoming waves. For this study, the focus is on capturing the first free vibration mode of the structure. The resulting peak wave frequencies f_p, the corresponding probes at which these peaks are measured, and the tension parameters T_ρ for each depth-Froude number are presented in Table 4.4.

Fr_d	f_p	Probe (peak)	T_ρ
0.6	0.35	P_2, P_3, P_8, P_9	63.504
0.7	0.35	P_4, P_6	63.504
0.8	0.23	P_5	27.423
0.9	0.23	P_2	27.423
1.0	0.24	P_3, P_5	29.860
1.1	0.24	P_2, P_3, P_5	29.860
1.2	0.30	P_2, P_3	46.656
1.3	0.29	P_1, P_2, P_3, P_4	43.597
1.4	0.30	P_6	46.656

Table 4.4: Peak wave frequencies f_p for probes $P_1 - P_9$ and tension parameters T_ρ for each depth-Froude number.

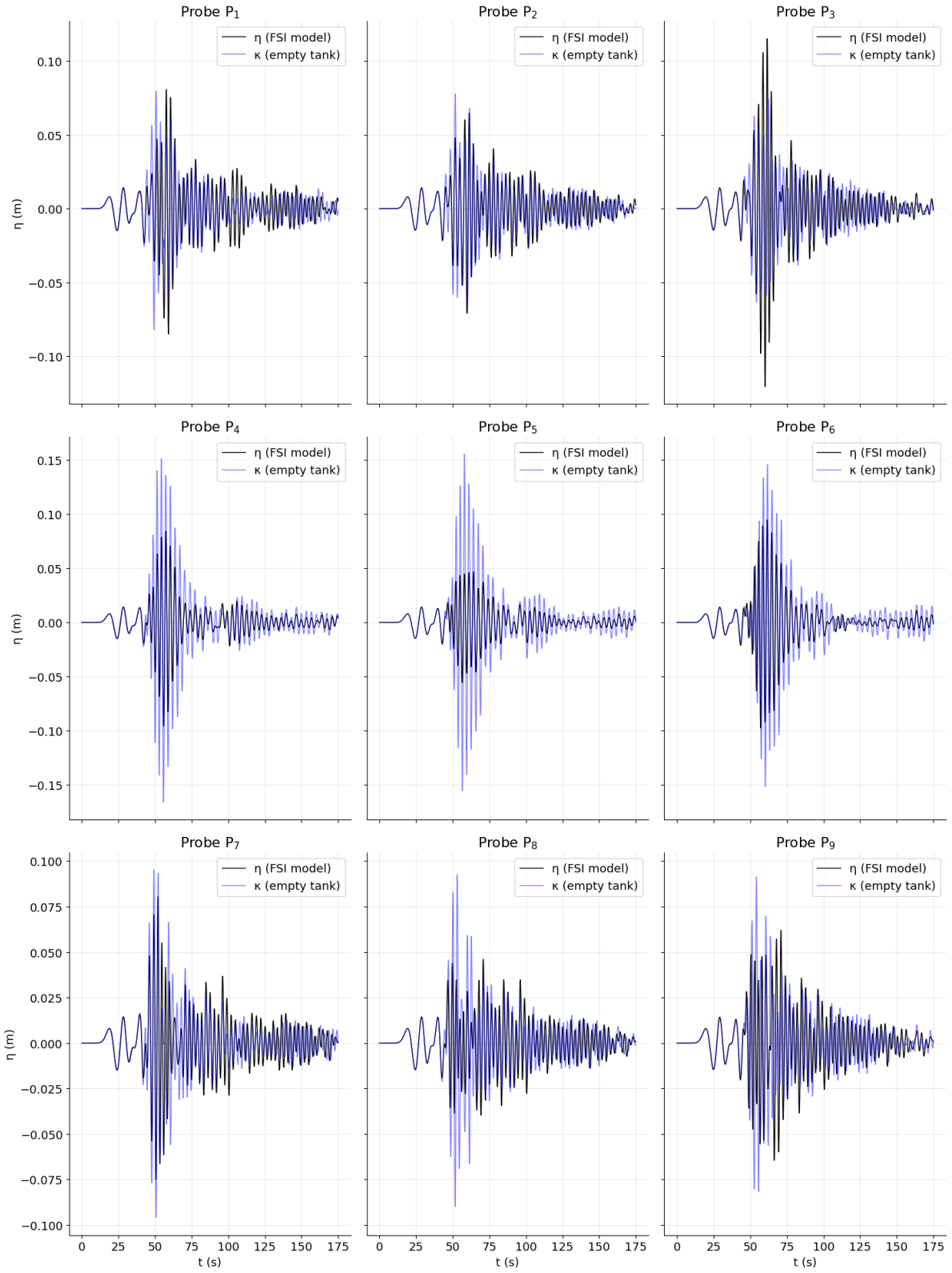

Figure 4.16: Time-series of membrane deflection η measured at probes $P_1 - P_9$ for a depth-Froude number $Fr_d = 0.6$ (sub-critical regime), compared to the measured surface-elevation κ from the empty tank.

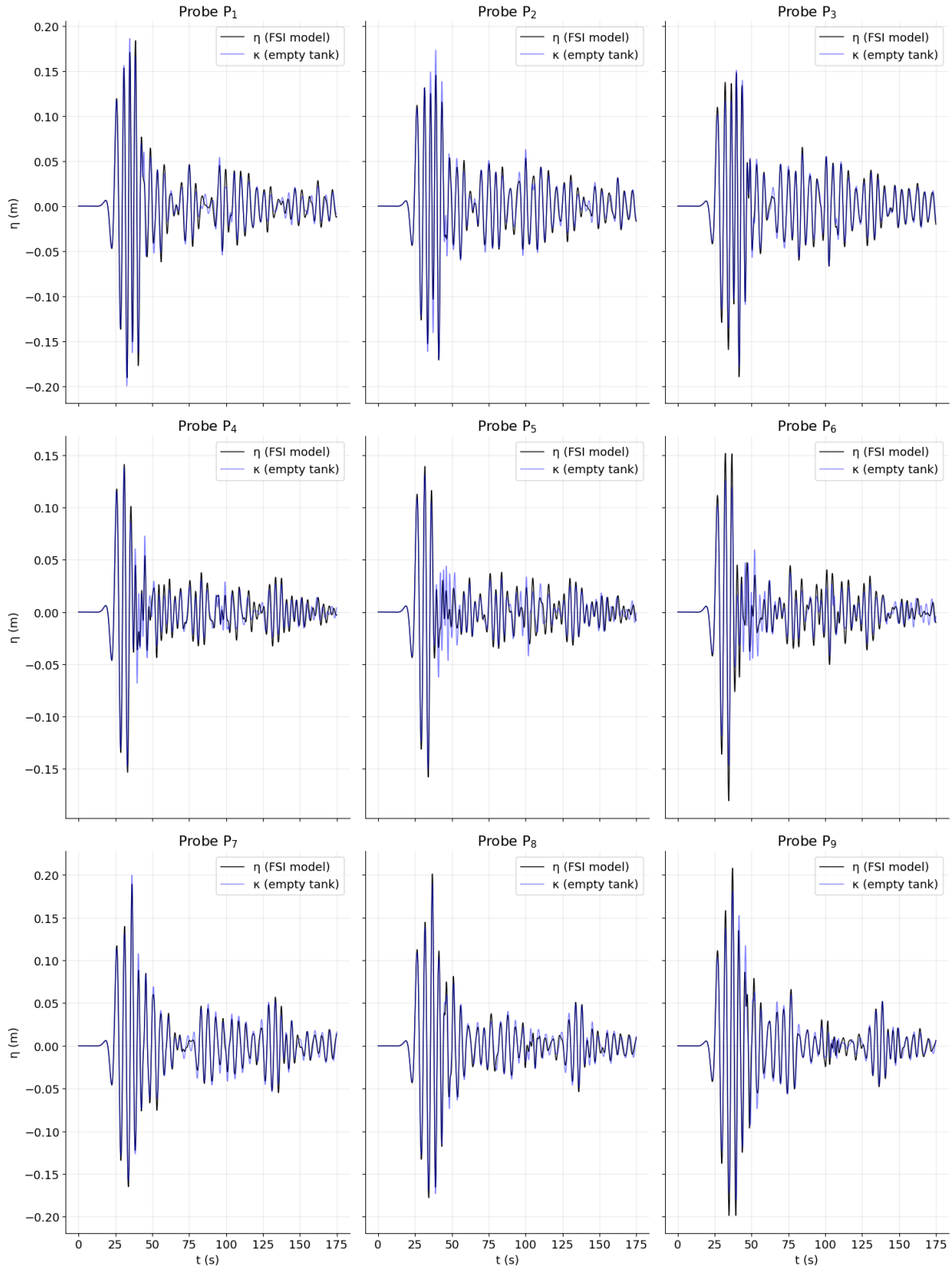

Figure 4.17: Time-series of membrane deflection η measured at probes $P_1 - P_9$ for a depth-Froude number $Fr_d = 0.9$ (trans-critical regime), compared to the measured surface-elevation κ from the empty tank.

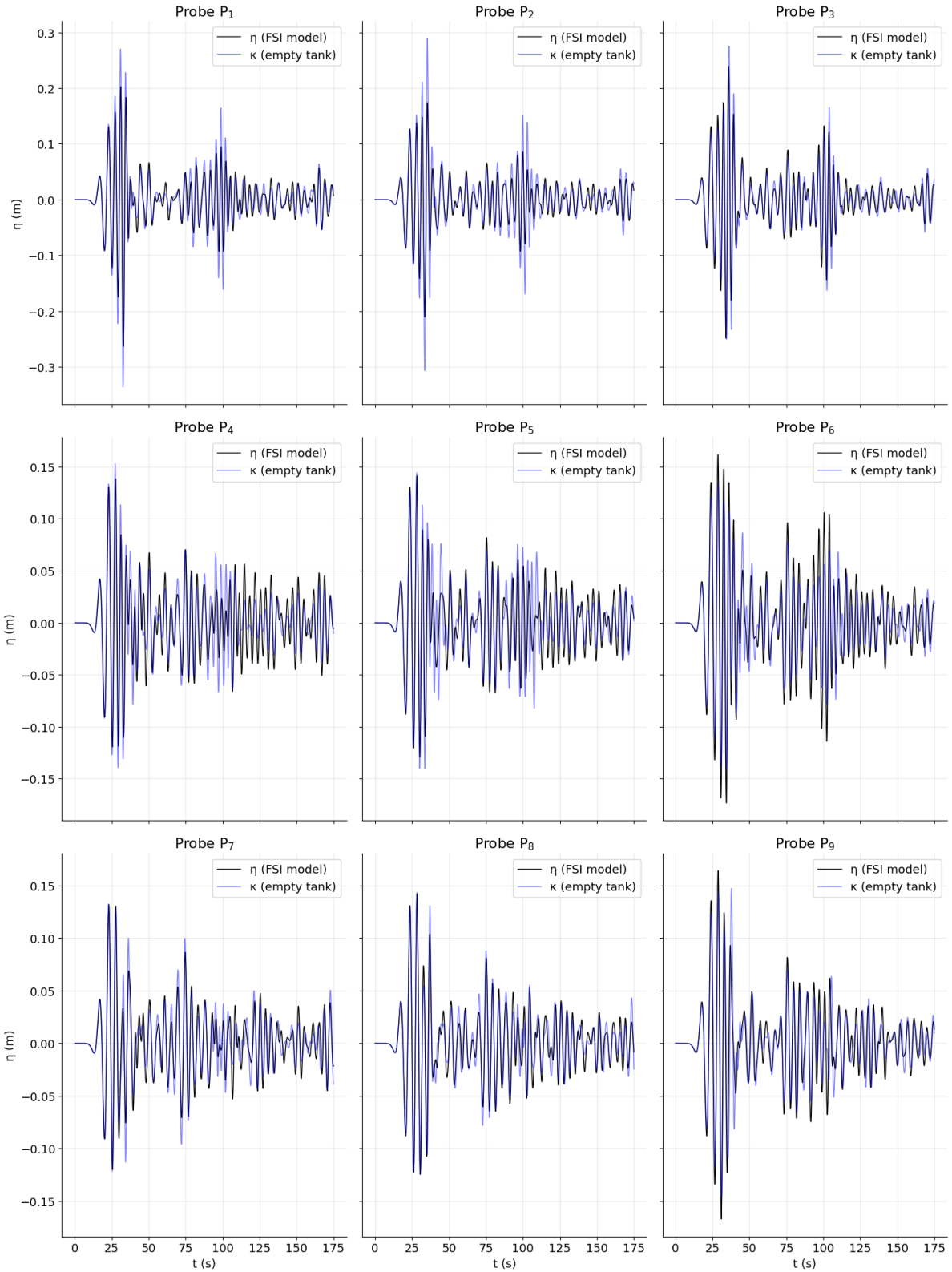

Figure 4.18: Time-series of membrane deflection η measured at probes $P_1 - P_9$ for a depth-Froude number $Fr_d = 1.2$ (super-critical regime), compared to the measured surface-elevation κ from the empty tank.

The time-series of the membrane deflection show that the structure's response is highly irregular, reflecting the irregular nature of the ship-induced waves. Furthermore, the hydroelastic effects are clearly visible across all test cases. In each of the cases considered, the membrane initially follows the long incoming waves, which are the first stage of ship-induced waves, behaving in the same way as the free surface. After the long waves pass, an irregular wave train propagates towards the structure, and the response varies depending on the depth-Froude number and the location of the probes. During the excitation caused by the short irregular wave train, the stiffness of the membrane becomes evident in the response graphs, where the membrane's response is either (significantly) amplified relative to the incoming waves or dampened, leading to smaller amplitude oscillations.

Determining whether resonance occurs in this time-domain problem is not straightforward, as the forcing from ship-induced waves is transient and not harmonically continuous. To quantify the floating structure's response relative to the wave field in the absence of the structure, the relative amplitude error parameter, defined as $A_r = \sqrt{\sum \eta^2 / \sum \kappa^2}$, is used. This parameter is calculated for probes $P_1 - P_9$ across all tested depth-Froude numbers, resulting in a range of errors, which are presented in Table 4.5 and Figure 4.19. Here, a perfect match between the two signals corresponds to $A_r = 1$. Values of $A_r > 1$ indicate that the structure's response is amplified relative to the wave field, while values of $A_r < 1$ suggest that the structure's response is dampened.

Fr_d	P_1	P_2	P_3	P_4	P_5	P_6	P_7	P_8	P_9
0.6	1.037	0.943	1.339	0.540	0.413	0.678	0.897	0.728	0.921
0.7	0.728	0.723	0.903	0.685	0.602	0.773	0.938	0.812	0.875
0.8	0.966	0.926	1.025	0.996	0.989	1.091	0.994	1.012	1.047
0.9	1.009	0.949	1.060	1.041	1.039	1.174	0.988	1.013	1.054
1.0	1.001	0.921	1.078	1.034	1.026	1.203	0.997	1.019	1.071
1.1	0.991	0.880	1.075	1.064	0.998	1.251	1.028	1.032	1.110
1.2	0.827	0.758	0.981	0.977	0.953	1.218	0.961	0.995	1.067
1.3	0.852	0.761	0.993	0.963	0.956	1.244	0.955	0.989	1.096
1.4	0.838	0.729	0.955	0.932	0.898	1.160	0.949	0.980	1.078

Table 4.5: Quantification of the membrane deflection η at probes $P_1 - P_9$ with respect to the surface-elevation κ for different depth-Froude numbers, using the relative amplitude error parameter A_r.

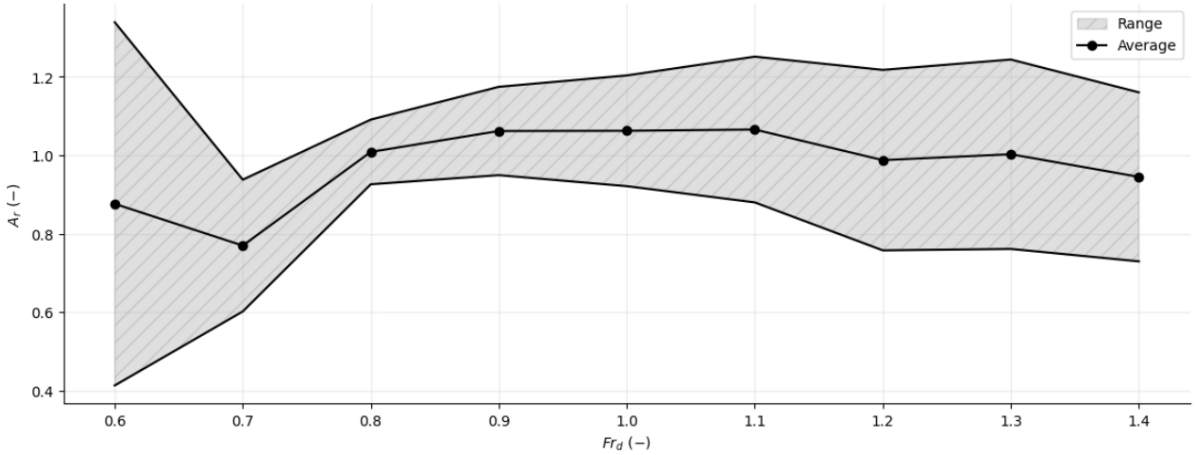

Figure 4.19: Range of the relative amplitude error parameter A_r for each depth-Froude number, along with the average values (in correspondence with Table 4.5).

The results presented here indicate that, despite the transient nature of the ship-wake signal, the system still contains sufficient energy to excite the structure with relatively large responses. This is primarily because the signal contains the natural frequency of the membrane. In the sub-critical regime, significant variations in the error parameter are observed, suggesting that for low depth-Froude numbers,

the structure's response is either heavily dampened or experiences large oscillations relative to the incoming waves. In contrast, for the trans-critical and super-critical regimes, the membrane tends to more closely follow the incoming waves on average, with smaller variations in response. Interestingly, while the largest incoming wave heights, H_{max}, were observed for $Fr_d = 0.9$ in Figure 4.15, this does not necessarily correlate with the largest amplifications in the hydroelastic response of the structure.

4.4.3. Deformation membrane in 2D

As previously outlined, the overall 3D problem involves a 2D floating membrane. Therefore, in this subsection, the 2D deformations of the membrane will be plotted at different time-instants. This is shown in Figure 4.20 for depth-Froude numbers $Fr_d = \{0.6, 0.9, 1.2\}$, where the time variable t is non-dimensionally represented as $\tilde{t} = v_s t/h$, with v_s being the velocity of the vessel and h the still-water depth. The deformations are plotted for $\tilde{t} = \{12.5, 35.7, 74.3\}$, which, for the $Fr_d = 0.6$ depth-Froude number FSI problem case studied earlier, correspond to time-instants at which the membrane experiences different phases of wave-excitation: first, by long waves, then by large amplitude oscillations caused by the wave-train, and finally, by short oscillations occurring after the wave-train has passed.

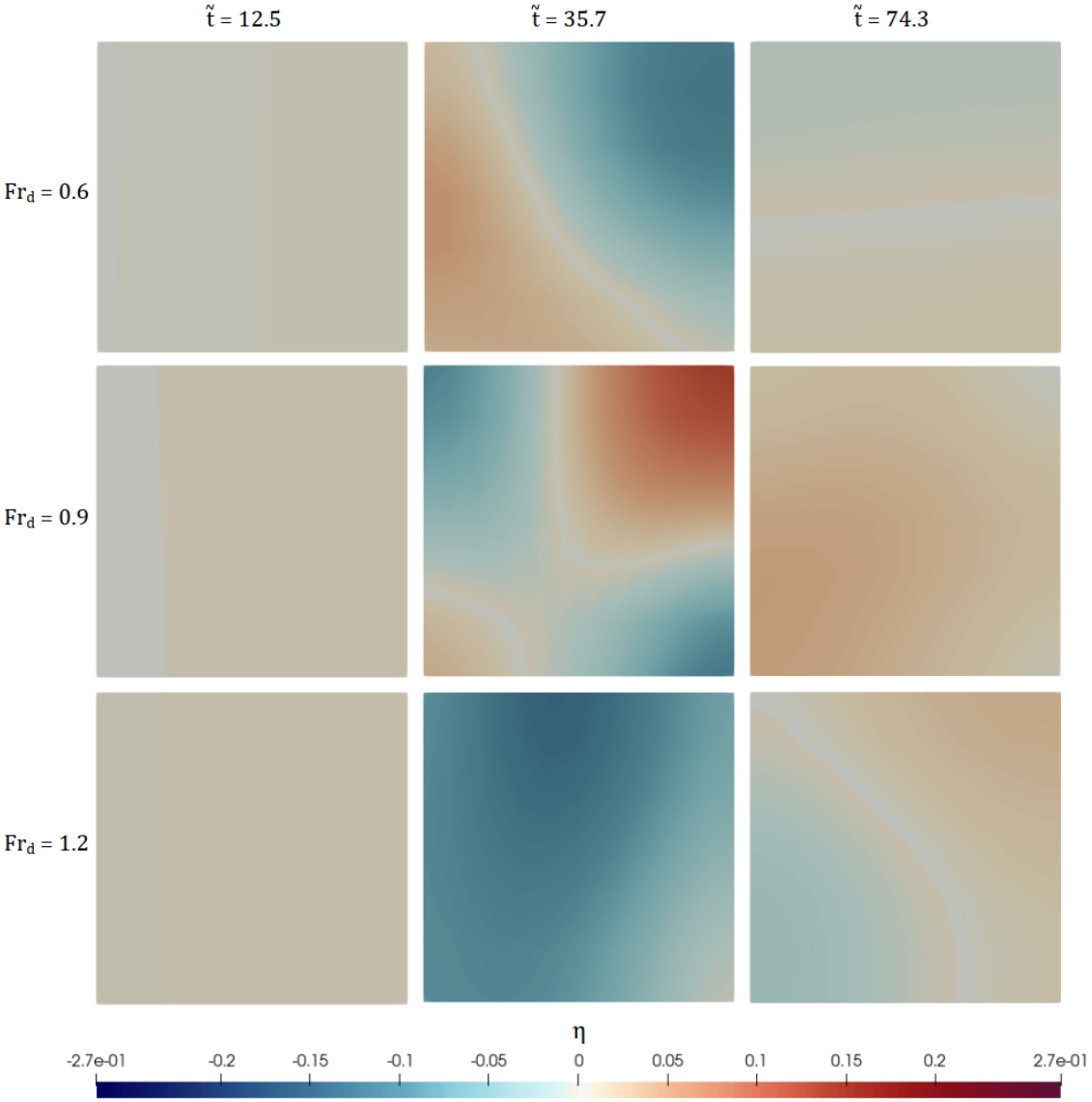

Figure 4.20: Hydroelastic deformation of the membrane in 2D for waves induced by vessel movement at $Fr_d = \{0.6, 0.9, 1.2\}$, plotted for non-dimensional time-instants $\tilde{t} = \{12.5, 35.7, 74.3\}$.

The first time-instant plotted, at $\tilde{t} = 12.5$, shows relatively small amplitude vibrations as the membrane closely follows the long waves in this regime. In the second stage, at $\tilde{t} = 35.7$, significant gradients in the membrane deformation are observed, due to the short, irregular wave-train, with clear hydroelastic effects visible in the deformation, particularly in the trans-critical regime. Finally, at $\tilde{t} = 74.3$, the membrane exhibits relatively small vibrations due to less steep gradients, indicating that the short waves have passed, leaving behind less pronounced vibrations.

There are several approaches to determine which modes are excited when a structure vibrates. A qualitative method would involve performing an FFT on the time-series of the membrane's response, identifying the natural frequencies of the membrane in the spectrum, and assessing which modes are excited by comparing the frequency of vibration to the corresponding natural frequencies. However, in this study, a quantitative approach will be employed to identify the excited modes. Contour plots and sections of the deformation along the membrane's center line ($y = 0$), are presented for the $Fr_d = 0.9$ case at the time-instants $t = \{250, 255, 400\}s$ in Figure 4.21. These plots provide a clear visual representation of the excited modes at different stages of the response.

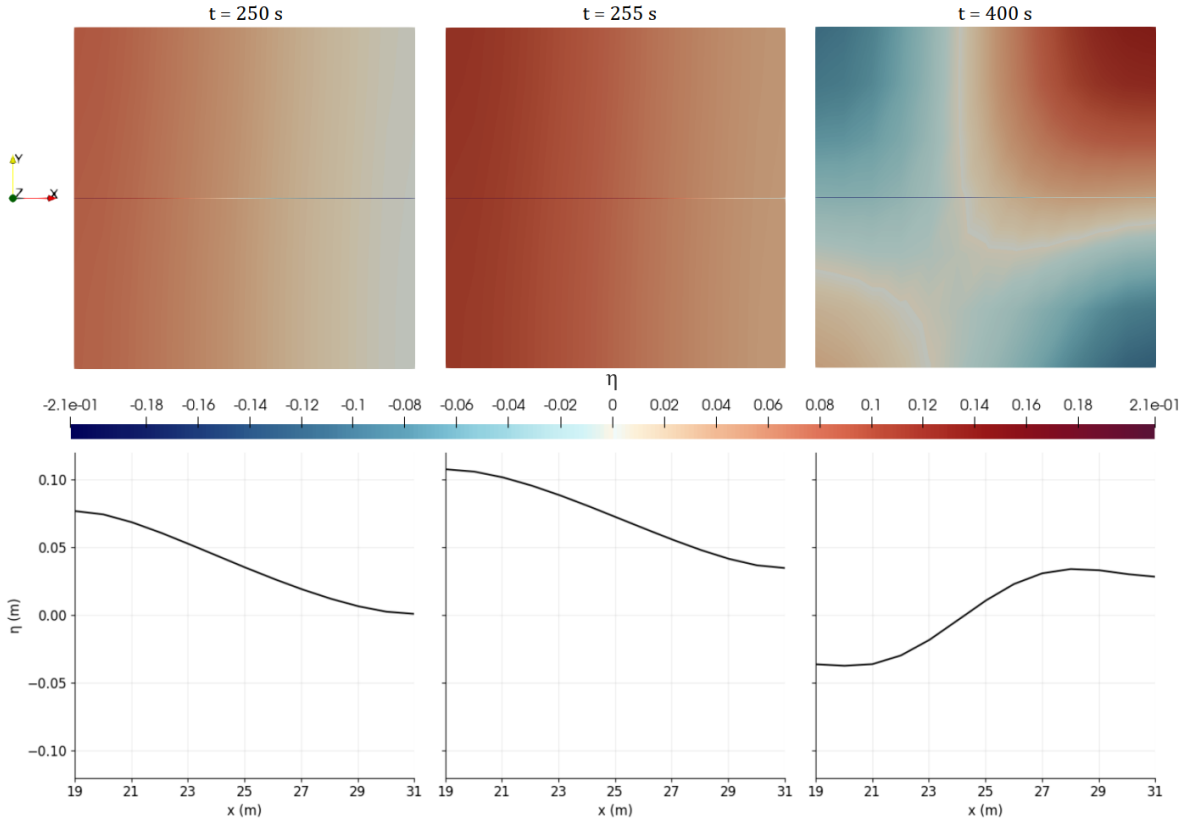

Figure 4.21: 2D contour plots of the membrane deformation, along with corresponding 1D graphs of the deformation along the center line, presented at different time-instants.

The results presented in Figure 4.21 show that a combination of mode 0, mode 1, and mode 2 are clearly present in the signal. At the time-instant $t = 250s$, the first mode of vibration is predominantly observed, characterised by a deformation with a single bifurcation point in the 1D graph. At $t = 255s$, the first mode is still visible, but it is shifted vertically relative to the still-water level, suggesting a rigid body heave motion. This rigid body motion is commonly seen in hydroelastic analyses and occurs alongside elastic deformation, as also noted in Reference [14]. At $t = 400s$, the activation of mode 2 is observed, indicated by the appearance of two bifurcation points in the deformation. The occurrence of these specific modes is consistent with the earlier analysis where the membrane tension was adjusted to align its first natural frequency with the peak frequency of the wave signal. This alignment is reflected in the membrane's hydroelastic response.

4.4.4. Evaluation hybrid model through global 3D perspective

Throughout the preceding sections, hydroelastic phenomena were primarily analysed by examining the wave conditions and the membrane deflection separately. Since this thesis employs a hybrid model, the final part of the analysis will showcase the global behaviour of this hybrid model for the 3D problem of ship-induced waves interacting with floating membranes. This will be demonstrated for a ship moving at a depth-Froude number of $Fr_d = 0.6$, where the 3D FSI domain is placed inside the 2D FEBOUSS domain[1], as clearly illustrated in Figure 4.22.

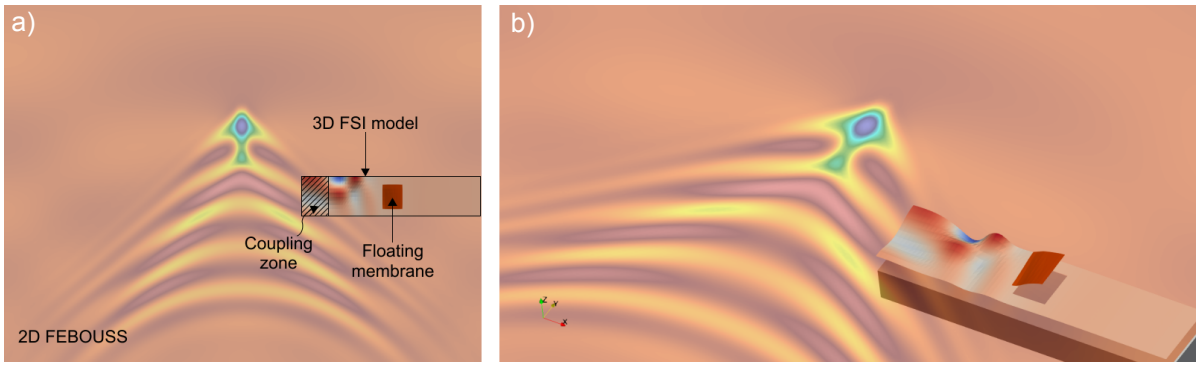

Figure 4.22: a) Top view hybrid model (FEBOUSS coupled with FSI model) displayed for a ship moving at $Fr_d = 0.6$ at time-instant $t = 42.0s$. b) 3D render of the transfer of wave-information at the same time-instant.

The plots in Figure 4.22 visually highlight key observations that validate the effectiveness of the proposed fluid-fluid coupling strategy, which were not as easily identifiable in the previous analysis. Firstly, the accurate transfer of surface-elevation data from the FEBOUSS wave-generation model to the FSI model is evident, with no discrepancies observed at the coupling interface. The one-way transfer of wave-information from FEBOUSS to the FSI model is confirmed, as the ship's wake remains unchanged despite the presence of the FSI model. If a two-way fluid-fluid coupling algorithm had been used, the wave field in the FEBOUSS model would have been altered due to reflections from the FSI model. Secondly, clear internal reflections are observed within the FSI domain due to its narrow width, with the side walls becoming significant contributors to the high gradients observed in the surface-elevation.

To finalise this thesis, the hydroelastic behaviour of the floating membrane is further illustrated through a series of plots depicting the FSI domain in isolation, as shown in Figure 4.23. This figure presents the full 3D FSI domain at six different time-instants, showcasing the deformation of the membrane as it responds to various stages of the ship-induced wave excitation. Each plot highlights a distinct physical phenomenon, offering a clear and comprehensive representation of the membrane's hydroelastic response over time.

The first plot in Figure 4.23 shows the initial conditions applied to the model, where the fluid velocity potential ϕ, membrane deflection η, and surface-elevation κ are all set to zero at $t = 0s$. This condition represents calm water, as no waves from the FEBOUSS model have yet reached the inlet of the FSI domain. At the subsequent time-step, at $t = 18.5s$, long waves propagate into the FSI domain, clearly displaying wave crests and troughs. These wave patterns were also evident in earlier time-series analyses. At $t = 33.0s$, strong diffraction is observed at the corner points of the FSI model, indicating the turning of the waves as they enter the domain. Moving to $t = 41.0s$, a highly irregular wave-train typical of ship-induced waves propagates towards the floating membrane. At this point, internal reflections from the side walls of the FSI model become evident. As time progresses to $t = 58.8s$, large gradients in the membrane deformation appear as the short-length waves continue to propagate into the FSI domain. Finally, at $t = 70.0s$, the short waves continue to excite the membrane, causing it to vibrate with relatively small oscillations.

[1] Note that the FSI domain does not necessarily need to be inside the FEBOUSS domain, only the coupling zone should overlap with the FEBOUSS domain.

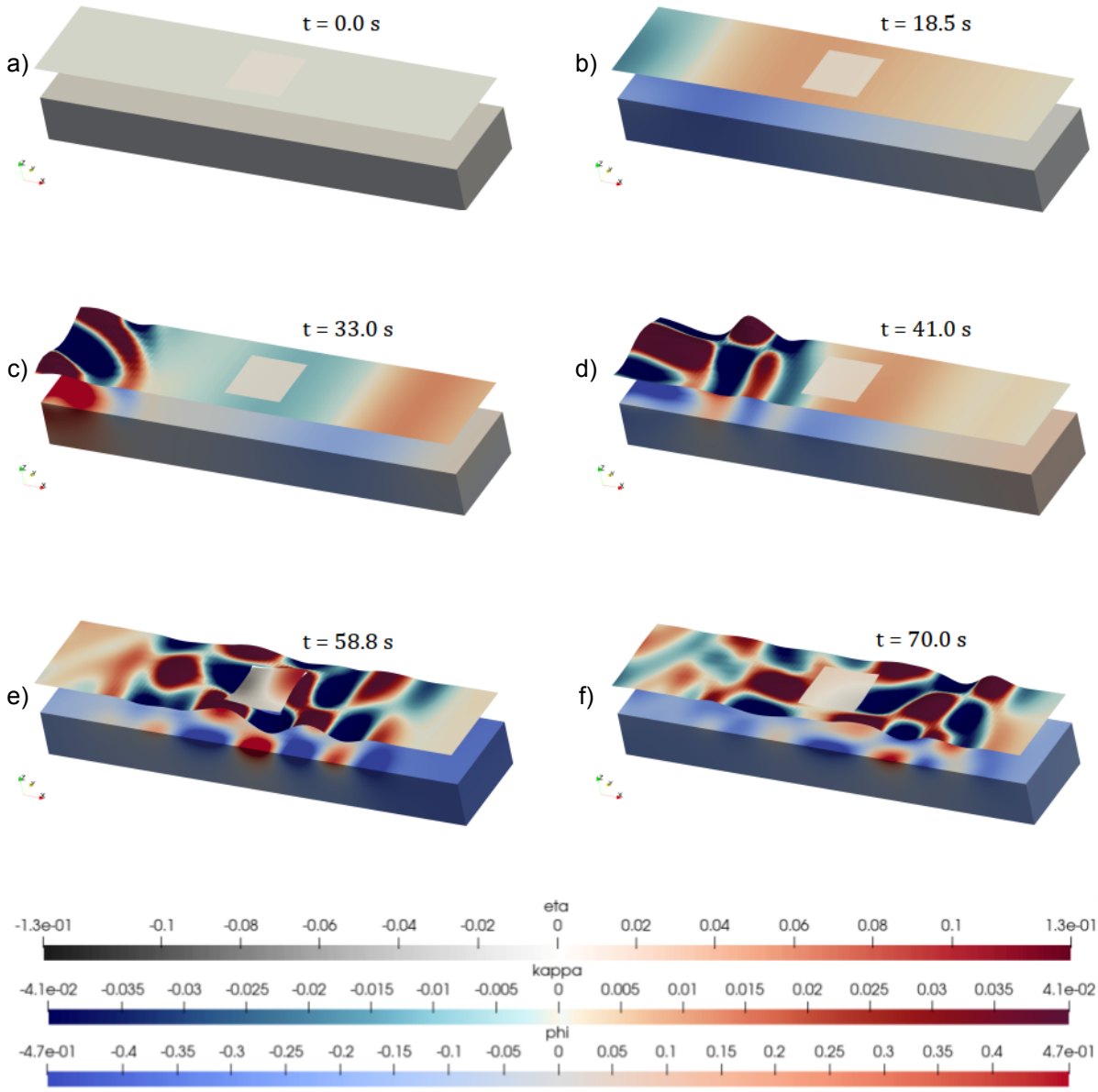

Figure 4.23: a) Initially calm waters. b) Long waves propagating in domain. c) Strong diffraction. d) Irregular wave-train propagating towards structure. e) Large gradients membrane deflection. f) Short waves continuing to excite the membrane.

One might question the decision to use dry natural frequencies for the membrane rather than wet ones, as the latter would offer a more realistic representation of the underlying physics. However, this choice is not expected to lead to significantly different outcomes in terms of the membrane's response, as the ship-wake amplitude spectrum is broad and contains a wide range of frequencies. It is important to note, however, that the contribution from each vibration mode in the hydroelastic response will certainly vary with the use of wet modes. Nonetheless, ship-induced waves interacting with thin floating membranes are expected to be physically interpretable as a transient, large impulsive load on the structure, which gradually dampens in amplitude over time, as clearly depicted in Figure 4.23.

5

Conclusion

This thesis aimed to address existing research gaps related to the interaction between flexible floating structures and a category of waves observed in nature by using a hybrid model. This model couples the 2D weakly nonlinear FEBOUSS wave-generation model with a 3D time-domain linearised monolithic FSI model, primarily focusing on the hydroelastic behaviour of a thin square floating membrane excited by waves generated by a nearby moving vessel in relatively calm waters. To achieve this, a novel 3D one-way partitioned fluid-fluid coupling algorithm has been developed to effectively transfer wave-information between the two numerical models.

Before delving into the hydroelastic analysis, the characteristics of ship-induced waves have been studied extensively. It was found that ship-induced waves are characterised by an irregular wave-train, relatively long wavelengths, and a transient nature. To effectively study ship-induced waves without interference from other physical phenomena, a sufficiently large domain was necessary. Subsequently, the influence of the distance from a moving pressure field relative to spatial points was assessed, along with the impact of the vessel's velocity on the resulting wave field. It was observed that the waves initially start as long waves, requiring some time to develop further, eventually resulting in a highly irregular short wave-train. Regarding the influence of the velocity, notably different patterns in the wave field emerge depending on the depth-Froude number. This includes: (1) cases where both divergent and transverse waves are equally present in the wave field, typical of the sub-critical regime, (2) instances where these waves amplified each other, resulting in significant gradients in the surface-elevation, characteristic of the trans-critical regime, and (3) high-velocity cases where only divergent waves are present, typical of the super-critical regime.

The FEBOUSS model provides wave input to the FSI model through feeding particles in the damping zone of the FSI model. This was achieved by probing wave-information from both a horizontal and vertical plane of the FEBOUSS model. A key contribution of this thesis is the successful implementation of this one-way fluid-fluid coupling approach for transferring the waves. The FSI model used here relied on the finite element method, where defining a weak form is part of the analysis, and boundary integrals automatically arise during the process. The coupling is efficiently implemented by enforcing the horizontal wave-particle velocity from FEBOUSS as the boundary condition at the inlet of the FSI model through the weak form. Additionally, a damping zone is used not only to absorb reflected waves from the membrane but also to enforce both the wave-elevation and vertical velocity at the free surface boundary of the damping zone. This approach ensures computational efficiency by reducing computational time and data storage requirements, while maintaining high physical accuracy.

The final part of the thesis focused on the research questions related to the hydroelastic response of the floating membrane when excited by ship-induced waves, as well as the inquiry whether resonance can occur in this FSI problem. To evaluate the potential for large responses, several tests were conducted, including the analysis of waves generated by vessels passing at different velocities. Spectral analysis was then employed to extract peak frequencies from the wave signals for each scenario. The natural frequency of the structure was aligned with the peak wave frequency present in each signal and multiple probes were placed to collect data on the deflection of the membrane. Hydroelastic effects became evident, demonstrating the flexibility of the structure as it closely followed the pattern of the

ship-induced waves. The behaviour of the membrane was studied over a sufficiently long time-series to understand its deformation characteristics, establishing a clear relation between the input wave conditions at specific time-instants and the resulting membrane behaviour. Finally, an examination was conducted to identify any significant responses in the structure that could lead to undesirable conditions during the design of floating membranes. It was determined that no resonance phenomena were observed for this particular FSI problem, as the excitation should be interpreted as a (large) transient impulsive force rather than a continuous harmonic excitation.

In response to the earlier formulated main research question: "*How can an efficient numerical fluid-fluid coupling algorithm be developed to couple a wave-generation model with a fluid-structure interaction model?*", the following conclusions can be drawn. The one-way partitioned coupling approach proposed here effectively transfers wave-information from FEBOUSS to the FSI model, while maintaining computational efficiency for the reasons outlined earlier. The accuracy of the numerical scheme can be improved by increasing the partition of feeding particles in the coupling zone and by extending the length of the damping zone where wave input is applied as a boundary condition, allowing for the accommodation of longer waves. A noteworthy result is that the coupling strategy performs well even in deep water cases, taking into account the individual limitations of the models involved.

Now, when addressing the second formulated main research question: "*How does the variation in ship speed influence the hydroelastic response of a floating membrane exposed to ship-induced waves in relatively calm waters?*", the following conclusions arise. First, the analysis was conducted for the specific case of a ship moving in a navigation channel of constant depth with a constant velocity, while the FSI domain, housing the floating structure, was modelled as a narrow harbour where waves enter from one face. This setup focused on fixed square membrane dimensions, and the influence of the velocity of a moving vessel was varied to study its effect on the deformation of the structure. This problem is particularly relevant in harbour engineering, where floating structures are placed near areas with heavy ship traffic, and vessel velocity must be regulated. The impact of the ship's velocity was expressed non-dimensionally using the depth-Froude number. In this analysis, no resonance behaviour was observed, even though the membrane's properties were adjusted to align its natural frequency with the peak wave frequency in the ship-wake. For this specific scenario, it was found that for long waves, the membrane tends to closely follow the incoming wave pattern across all depth-Froude number scenarios. Whereas, for the irregular wave-train propagating through, the stiffness of the membrane becomes more pronounced in the response. Depending on the depth-Froude number case and the probe location, the response could either be amplified or dampened. Generally, it was observed that for $Fr_d \approx 1$, the membrane experienced significant hydroelastic deformations, which were clearly pronounced in the signal. For the $Fr_d = 0.6$ case, where both divergent and transverse waves were present, the membrane's response exhibited the most notable fluctuations. In this scenario, the membrane's deformation was either strongly amplified by the wave-field or remained very stiff in relation to the incoming waves, highlighting the complex interplay between the wave dynamics and the membrane's stiffness in the hydroelastic response.

Although the analysis focused on a specific FSI problem with several limitations, it provides a solid foundation for a broad range of future studies. This work lays the groundwork for understanding more complex interactions between various types of waves and offshore structures.

6

Recommendations

The FEBOUSS wave-generation model, FSI model, and fluid-fluid coupling algorithm used in this thesis are highly versatile, paving the way for exploring a wide range of interesting future studies.

This thesis employed a one-way partitioned approach to transfer wave-information from FEBOUSS to the FSI model. However, in real-world scenarios, the presence of a floating structure on water induces reflections in the direction opposite to the the incoming waves. This modifies the wave field due to the interference between incident and reflected waves, a characteristic captured by two-way fluid-fluid coupling. Implementing a two-way coupling approach would provide different results and reveal additional phenomena, further enhancing the understanding of fluid-structure interaction problems.

In reality, when a structure vibrates in water, the surrounding water particles are also accelerated due to added-mass effects. These effects can significantly influence the response of offshore structures, but were not considered in this study. However, using wet modes would lead to different vibration frequencies for the membrane. For future applications, incorporating wet modes is recommended to provide a more accurate representation of the membrane's deformation and to refine the understanding of the actual magnitude of these responses.

The FEBOUSS and FSI models used here have many additional parameters that could be explored in future research. More complex scenarios could include factors such as variable bathymetry, different ship sizes, multiple wave input faces, and structures with arbitrary geometries. Furthermore, wave input generated by multiple ships within the same domain could be considered. The nonlinear nature of the wave-generation model suggests that incorporating these factors would yield entirely different results. A practical example where such complexity could be relevant is in the port of Rotterdam, where the navigation channel is deeper than the surrounding harbours. This setup introduces different physics, such as shoaling, and more complex fluid-fluid interactions due to the need to account for wave input from multiple sides simultaneously.

Further exploration in these directions would significantly enhance understanding of complex fluid-structure interactions, not only for floating structures but also for a wide range of offshore engineering applications. Such studies could provide valuable insights for optimising the design and improving the resilience of these structures.

A

Monolithic weak form

The weak form presented in Subsection 3.2.1 will be derived step-by-step in this appendix. For convenience, the governing equations are first repeated here in their continuous form. The analysis then clearly demonstrates the process of transitioning the weak form from an empty tank, which includes two damping zones, to the case where a floating structure is introduced into the domain.

A.1. Strong form governing equations

Consider the three-dimensional Laplace equation to describe a potential fluid flow:

$$\nabla^2\phi = 0 \quad \text{in} \quad \Omega. \tag{A.1}$$

The governing fluid flow equation is supplemented with the following kinematic boundary conditions for the fluid domain:

$$\mathbf{n}\cdot\nabla\phi = 0 \qquad \text{on } \Gamma_b, \tag{A.2a}$$
$$\mathbf{n}\cdot\nabla\phi = u_{in} \qquad \text{on } \Gamma_{in}, \tag{A.2b}$$
$$\mathbf{n}\cdot\nabla\phi = u_{out} \qquad \text{on } \Gamma_{out}, \tag{A.2c}$$
$$\mathbf{n}\cdot\nabla\phi = \dot{\kappa} \qquad \text{on } \Gamma_{fs}, \tag{A.2d}$$

along with the dynamic free surface boundary condition, which reads:

$$\dot{\phi} + g\kappa = 0 \quad \text{on} \quad \Gamma_{fs}. \tag{A.3}$$

The tank is equipped with two damping zones. In accordance with the methodology outlined in Reference [22], the kinematic damping condition is first applied at the free surface, followed by the dynamic damped free surface boundary condition. These conditions for the inlet damping zone are expressed as follows:

$$\mathbf{n}\cdot\nabla\phi = \dot{\kappa} + \mu_{2,in}(\kappa - \hat{\kappa}) \quad \text{on } \Gamma_{d1}, \tag{A.4a}$$
$$\dot{\phi} + g\kappa + \mu_{1,in}(\mathbf{n}\cdot\nabla(\phi - \hat{\phi})) = 0 \quad \text{on } \Gamma_{d1}. \tag{A.4b}$$

In a similar manner to the inlet damping zone, the boundary conditions for the outlet damping zone can be specified as follows:

$$\mathbf{n}\cdot\nabla\phi = \dot{\kappa} + \mu_{2,out}(\kappa - \hat{\kappa}) \quad \text{on } \Gamma_{d2}, \tag{A.5a}$$
$$\dot{\phi} + g\kappa + \mu_{1,out}(\mathbf{n}\cdot\nabla(\phi - \hat{\phi})) = 0 \quad \text{on } \Gamma_{d2}. \tag{A.5b}$$

As a structure is present in the domain, interface conditions describing the fluid-structure coupling must be specified. First, the kinematic coupling condition is provided, followed by the dynamic coupling

condition, as given below:

$$\mathbf{n} \cdot \nabla\phi = \dot{\eta} \qquad \text{on } \Gamma_m, \tag{A.6a}$$

$$m_\rho \ddot{\eta} - \nabla_h \cdot (T_\rho \nabla_h \eta) - \nabla_h \cdot (\tau T_\rho \nabla_h \dot{\eta}) + \dot{\phi} + g\eta = 0 \qquad \text{on } \Gamma_m. \tag{A.6b}$$

The boundaries of the membrane are assumed to be free to translate in vertical direction, which is described by the following boundary condition:

$$\mathbf{n} \cdot \nabla_h \eta = 0 \quad \text{on } \Lambda_m. \tag{A.7}$$

With the boundary value problem formulated, the next step in the analysis is to convert the strong form of the governing fluid flow equation into its weak form, while also addressing the boundary and interface conditions.

A.2. Derivation weak form

In accordance with the finite element method, Equation A.1 must be multiplied by a certain weight function, $w \in \mathcal{V}$, and then integrated over the entire domain Ω, as follows:

$$\int_\Omega \left[w \cdot \nabla^2 \phi \right] d\Omega = 0, \quad \forall\, w \in \mathcal{V}. \tag{A.8}$$

To balance the order of the derivatives of the functions w and ϕ on the left-hand side of Equation A.8, integration by parts is performed, leading to the following expression:

$$\int_\Omega \left[w \cdot \nabla^2 \phi \right] d\Omega = \int_\Omega \left[\nabla w \cdot \nabla \phi \right] d\Omega - \int_\Gamma \left[w \cdot (\mathbf{n} \cdot \nabla \phi) \right] d\Gamma = 0. \tag{A.9}$$

The results obtained from Equation A.9 demonstrate the significance of the integration by parts step, as is leads to an expression consisting of a reduced-order domain integral and a boundary integral, which is expressed over the domain boundary Γ. This boundary integral can be conveniently expanded into a summation of multiple subdomain integrals, as follows:

$$\begin{aligned} \int_\Gamma \left[w \cdot (\mathbf{n} \cdot \nabla \phi) \right] d\Gamma = &\int_{\Gamma_b} \left[w \cdot (\mathbf{n} \cdot \nabla \phi) \right] d\Gamma_b + \int_{\Gamma_{out}} \left[w \cdot (\mathbf{n} \cdot \nabla \phi) \right] d\Gamma_{out} + \int_{\Gamma_{in}} \left[w \cdot (\mathbf{n} \cdot \nabla \phi) \right] d\Gamma_{in} \\ &+ \int_{\Gamma_{fs}} \left[w \cdot (\mathbf{n} \cdot \nabla \phi) \right] d\Gamma_{fs} + \int_{\Gamma_{d1}} \left[w \cdot (\mathbf{n} \cdot \nabla \phi) \right] d\Gamma_{d1} + \int_{\Gamma_{d2}} \left[w \cdot (\mathbf{n} \cdot \nabla \phi) \right] d\Gamma_{d2} \end{aligned} \tag{A.10}$$

The boundary conditions specified in Section A.1 can now be applied. The dynamic boundary condition from Equation A.3 is subtracted from the right-hand side of the kinematic boundary condition in Equation A.2d, since the dynamic boundary condition equals zero. Here, the term representing the contribution of the dynamic boundary condition is multiplied by a modified test function, $(u + \alpha_h w)$, and weighted by a factor β_h for stability, as outlined in Reference [14]. After substituting the kinematic boundary conditions for the fluid particle velocity $(\mathbf{n} \cdot \nabla\phi)$ from Equation A.2, and incorporating the dynamic boundary condition from Equation A.3, Equation A.10 then simplifies to:

$$\begin{aligned} \int_\Gamma \left[w \cdot (\mathbf{n} \cdot \nabla \phi) \right] d\Gamma = &\int_{\Gamma_{out}} \left[w \cdot u_{out} \right] d\Gamma_{out} + \int_{\Gamma_{in}} \left[w \cdot u_{in} \right] d\Gamma_{in} + \int_{\Gamma_{fs}} \left[w \cdot \dot{\kappa} \right] d\Gamma_{fs} \\ &- \int_{\Gamma_{fs}} \left[(\dot{\phi} + g\kappa)\beta_h(\alpha_h w + u) \right] d\Gamma_{fs} + \int_{\Gamma_{d1}} \left[w \cdot (\mathbf{n} \cdot \nabla \phi) \right] d\Gamma_{d1} \\ &+ \int_{\Gamma_{d2}} \left[w \cdot (\mathbf{n} \cdot \nabla \phi) \right] d\Gamma_{d2}. \end{aligned} \tag{A.11}$$

The terms in Equation A.11 that have remained unchanged are integrals over the inlet damping zone Γ_{d1} and outlet damping zone Γ_{d2}. How the boundary conditions are implemented, will be demonstrated for the integral over the inlet damping zone Γ_{d1}. The dynamic boundary condition from Equation A.4b is subtracted from the kinematic boundary condition in Equation A.4a, and the resulting fluid particle

velocity $(\mathbf{n} \cdot \nabla\phi)$ is substituted accordingly. As before, the contribution from the dynamic boundary condition term is implemented using the stabilised approach, which involves modifying the test function. The result of this substitution into the boundary integral reads:

$$\begin{aligned}\int_{\Gamma_{d1}} [w \cdot (\mathbf{n} \cdot \nabla\phi)\,]\, d\Gamma_{d1} = &\int_{\Gamma_{d1}} [w \cdot \dot{\kappa}\,]\, d\Gamma_{d1} + \int_{\Gamma_{d1}} [w \cdot \mu_{2,in}\kappa\,]\, d\Gamma_{d1} - \int_{\Gamma_{d1}} \Big[(\dot{\phi} + g\kappa)\beta_h(\alpha_h w + u)\Big]\, d\Gamma_{d1} \\ &- \int_{\Gamma_{d1}} [\mu_{1,in}\mathbf{n} \cdot \nabla\phi(\alpha_h w + u)\,]\, d\Gamma_{d1} + \int_{\Gamma_{d1}} \Big[\mu_{1,in}\mathbf{n} \cdot \nabla\hat{\phi}(\alpha_h w + u)\Big]\, d\Gamma_{d1} \\ &- \int_{\Gamma_{d1}} [w \cdot \mu_{2,in}\hat{\kappa}\,]\, d\Gamma_{d1}.\end{aligned} \tag{A.12}$$

In a similar manner, while gradually damping the surface-elevation at the outlet damping zone to zero, the expression for the outlet boundary integral can be formulated as follows:

$$\begin{aligned}\int_{\Gamma_{d2}} [w \cdot (\mathbf{n} \cdot \nabla\phi)\,]\, d\Gamma_{d2} = &\int_{\Gamma_{d2}} [w \cdot \dot{\kappa}\,]\, d\Gamma_{d2} + \int_{\Gamma_{d2}} [w \cdot \mu_{2,out}\kappa\,]\, d\Gamma_{d2} - \int_{\Gamma_{d2}} \Big[(\dot{\phi} + g\kappa)\beta_h(\alpha_h w + u)\Big]\, d\Gamma_{d2} \\ &- \int_{\Gamma_{d2}} [\mu_{1,out}\mathbf{n} \cdot \nabla\phi(\alpha_h w + u)\,]\, d\Gamma_{d2}.\end{aligned} \tag{A.13}$$

The final step of this derivation involves substituting Equations A.11, A.12, A.13 back into the right-hand side of Equation A.9. This results in the weak form of a 3D empty tank wave propagation problem with two damping zones. Following the same procedure as outlined in this appendix, terms arising from the presence of the floating structure can be included. This will ultimately lead to the final weak form, which can be split into a bilinear form B given by the following expression:

$$\begin{aligned}B([\phi,\eta,\kappa],[w,v,u]) \doteq &\int_{\Omega} [\,\nabla\phi \cdot \nabla w]\, d\Omega - \int_{\Gamma_{fs}} [\,\dot{\kappa}w]\, d\Gamma_{fs} + \int_{\Gamma_{fs}} [\,(\dot{\phi} + g\kappa)\beta_h(u + \alpha_h w)]\, d\Gamma_{fs} \\ &- \int_{\Gamma_m} [\,\dot{\eta}w]\, d\Gamma_m + \int_{\Gamma_m} [\,v(m_\rho\ddot{\eta} + \dot{\phi} + g\eta)]\, d\Gamma_m + \int_{\Gamma_m} [\,\nabla v(T_\rho\nabla\eta + T_\rho\tau\nabla\dot{\eta})]\, d\Gamma_m \\ &- \int_{\Lambda_m} [\,v(\mathbf{n} \cdot T_\rho\nabla\eta + \mathbf{n} \cdot T_\rho\tau\nabla\dot{\eta})]\, d\Lambda_m + \int_{\Gamma_{d1}} [\,\beta_h(u + \alpha_h w)\dot{\phi} - w\dot{\kappa}]\, d\Gamma_{d1} \\ &+ \int_{\Gamma_{d2}} [\,\beta_h(u + \alpha_h w)\dot{\phi} - w\dot{\kappa}]\, d\Gamma_{d2} \\ &+ \int_{\Gamma_{d1}} [\,\beta_h(u + \alpha_h w)g\kappa - \mu_{2,in}\kappa w + \mu_{1,in}\mathbf{n} \cdot \nabla\phi(u + \alpha_h w)]\, d\Gamma_{d1} \\ &+ \int_{\Gamma_{d2}} [\,\beta_h(u + \alpha_h w)g\kappa - \mu_{2,out}\kappa w + \mu_{1,out}\mathbf{n} \cdot \nabla\phi(u + \alpha_h w)]\, d\Gamma_{d2},\end{aligned} \tag{A.14}$$

and a linear form L which reads:

$$L([w,v,u]) \doteq \int_{\Gamma_{in}} [\,u_{in}w]\, d\Gamma_{in} + \int_{\Gamma_{out}} [\,u_{out}w]\, d\Gamma_{out} - \int_{\Gamma_{d1}} [\,\mu_{2,in}\hat{\kappa}w - \mu_{1,in}\mathbf{n} \cdot \nabla\hat{\phi}(u + \alpha_h w)]\, d\Gamma_{d1}. \tag{A.15}$$

B

Measurements incoming waves

In this appendix, the measured surface-elevation κ and their corresponding amplitude-spectra at the inlet probe P_0 of the FSI domain for $Fr_d = \{0.6, 0.7, ..., 1.4\}$ are presented.

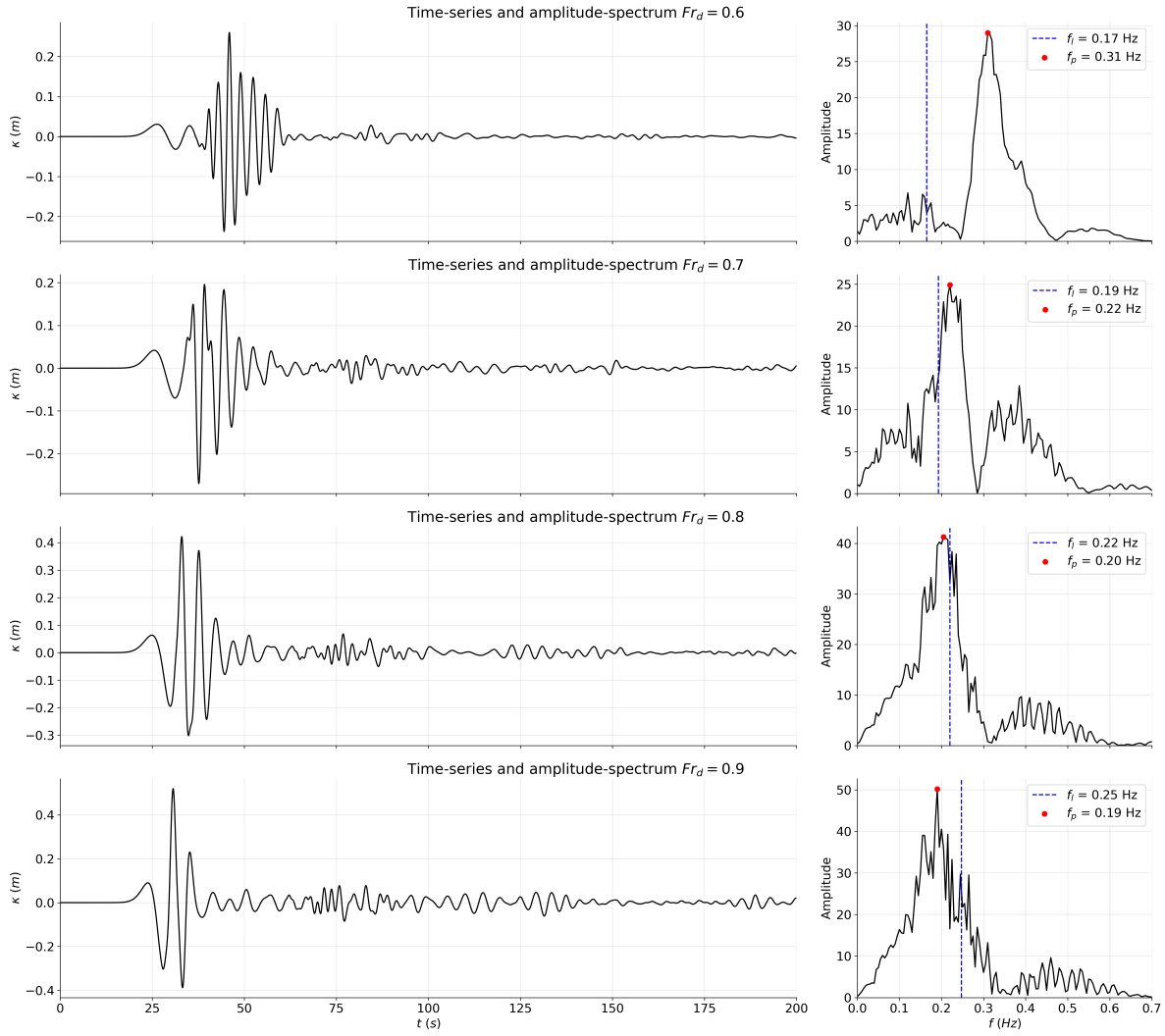

Figure B.1: Surface-elevation κ and their corresponding spectrum at inlet probe FSI model P_0 for $Fr_d = 0.6 - 0.9$.

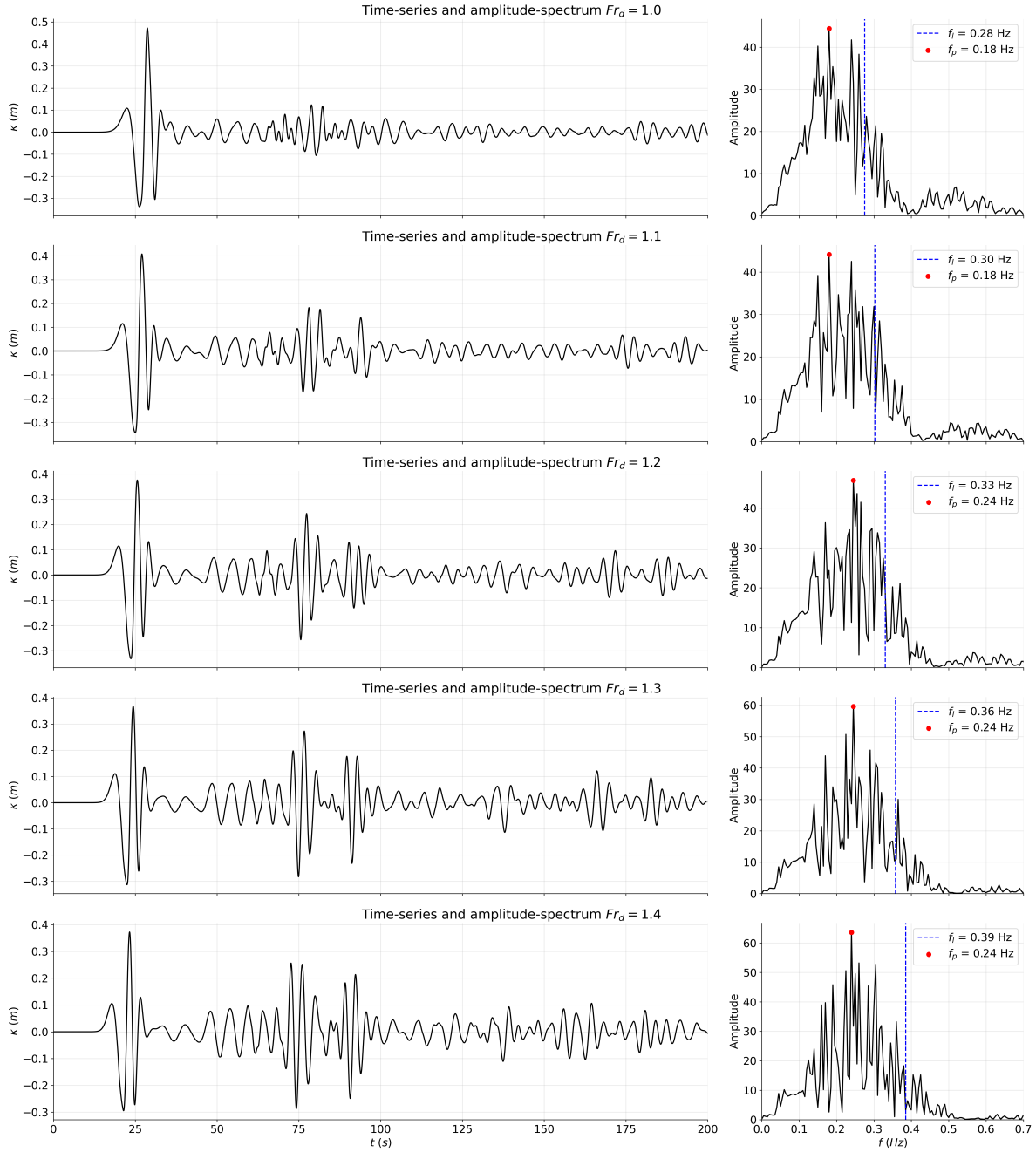

Figure B.2: Surface-elevation κ and their corresponding spectrum at inlet probe FSI model P_0 for $Fr_d = 1.0 - 1.4$.

C

Hydroelastic response

In this appendix, the complete hydroelastic response η of the membrane is presented for depth-Froude numbers $Fr_d = \{0.6, 0.7, ..., 1.4\}$, measured at the probes $P_1 - P_9$ within the FSI domain. These responses are compared at the same probes to the surface-elevation κ in an empty tank without floating membrane. The subsequent pages of this appendix provide the complete results.

C.1. Hydroelastic response with depth-Froude number 0.6

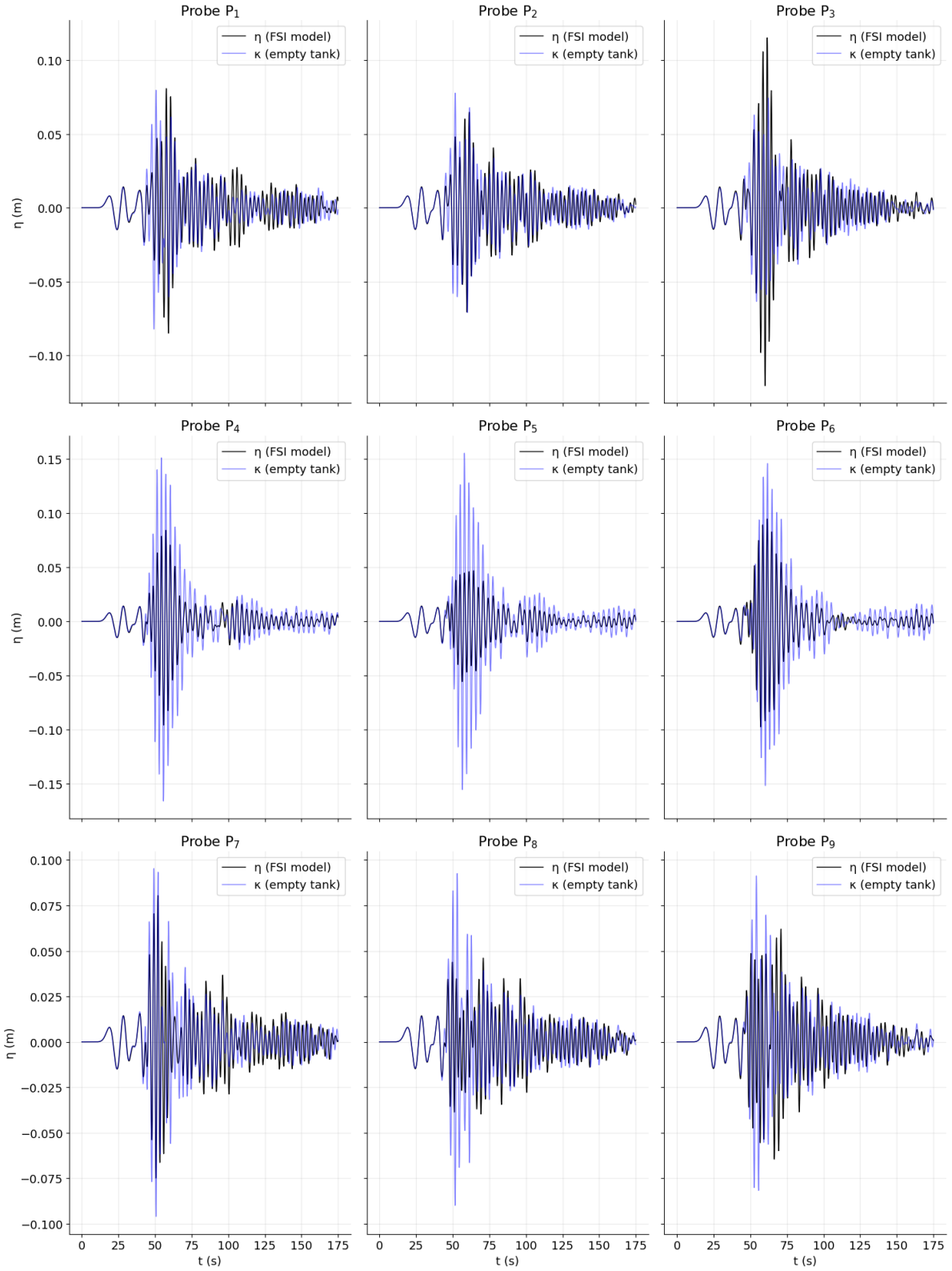

Figure C.1: Time-series hydroelastic response membrane measured at probes $P_1 - P_9$ for depth-Froude number $Fr_d = 0.6$.

C.2. Hydroelastic response with depth-Froude number 0.7

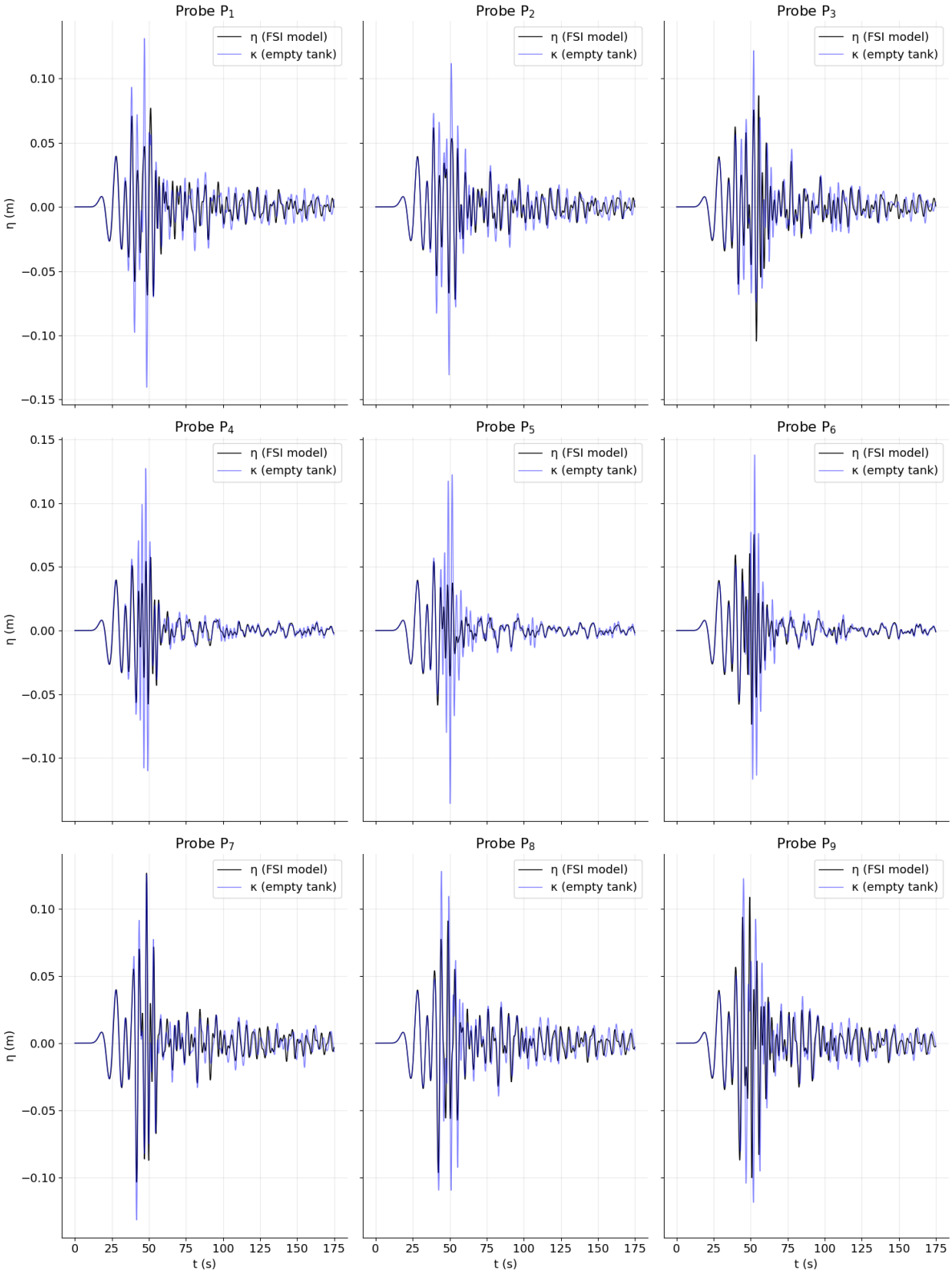

Figure C.2: Time-series hydroelastic response membrane measured at probes $P_1 - P_9$ for depth-Froude number $Fr_d = 0.7$.

C.3. Hydroelastic response with depth-Froude number 0.8

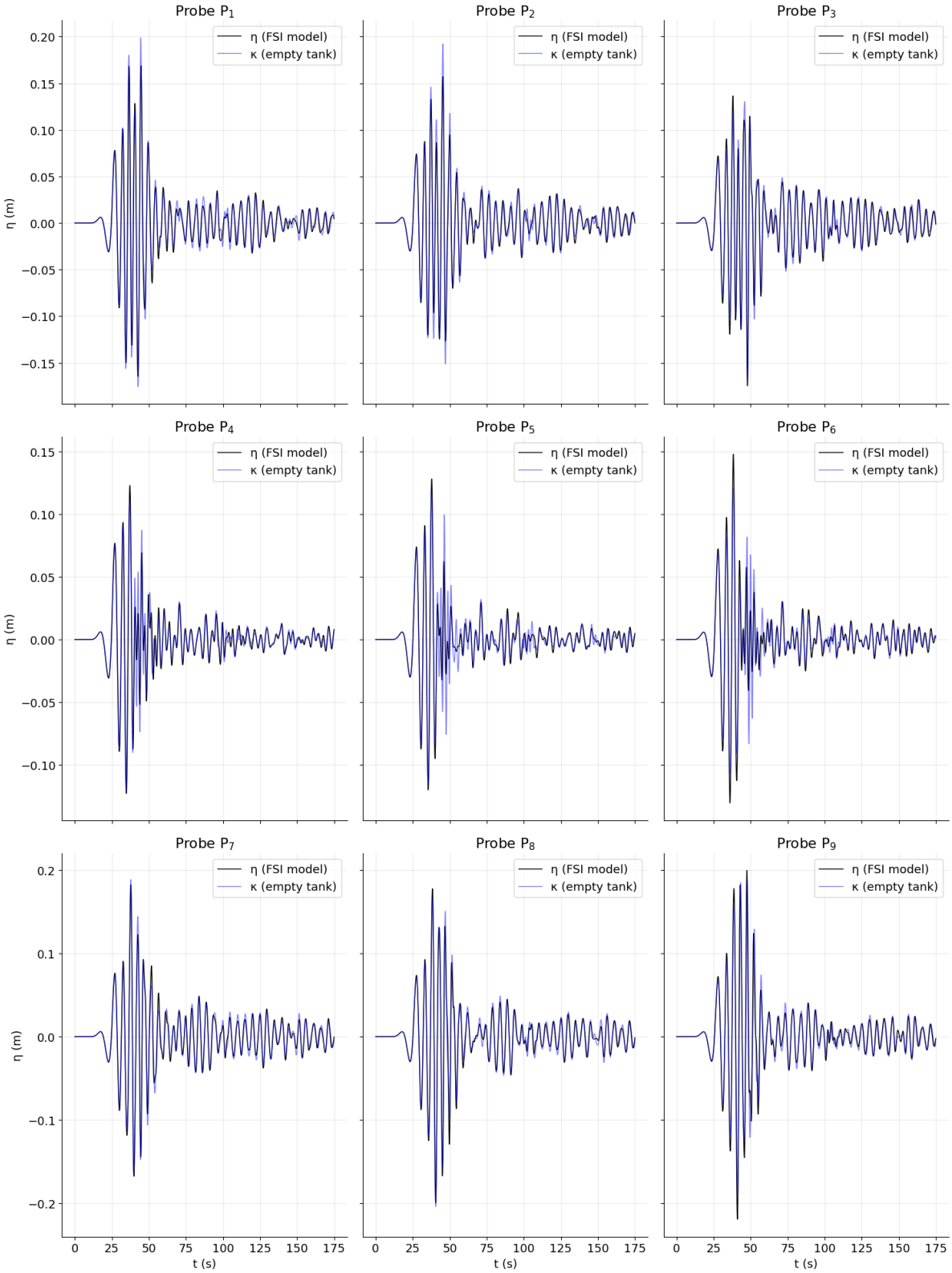

Figure C.3: Time-series hydroelastic response membrane measured at probes $P_1 - P_9$ for depth-Froude number $Fr_d = 0.8$.

C.4. Hydroelastic response with depth-Froude number 0.9

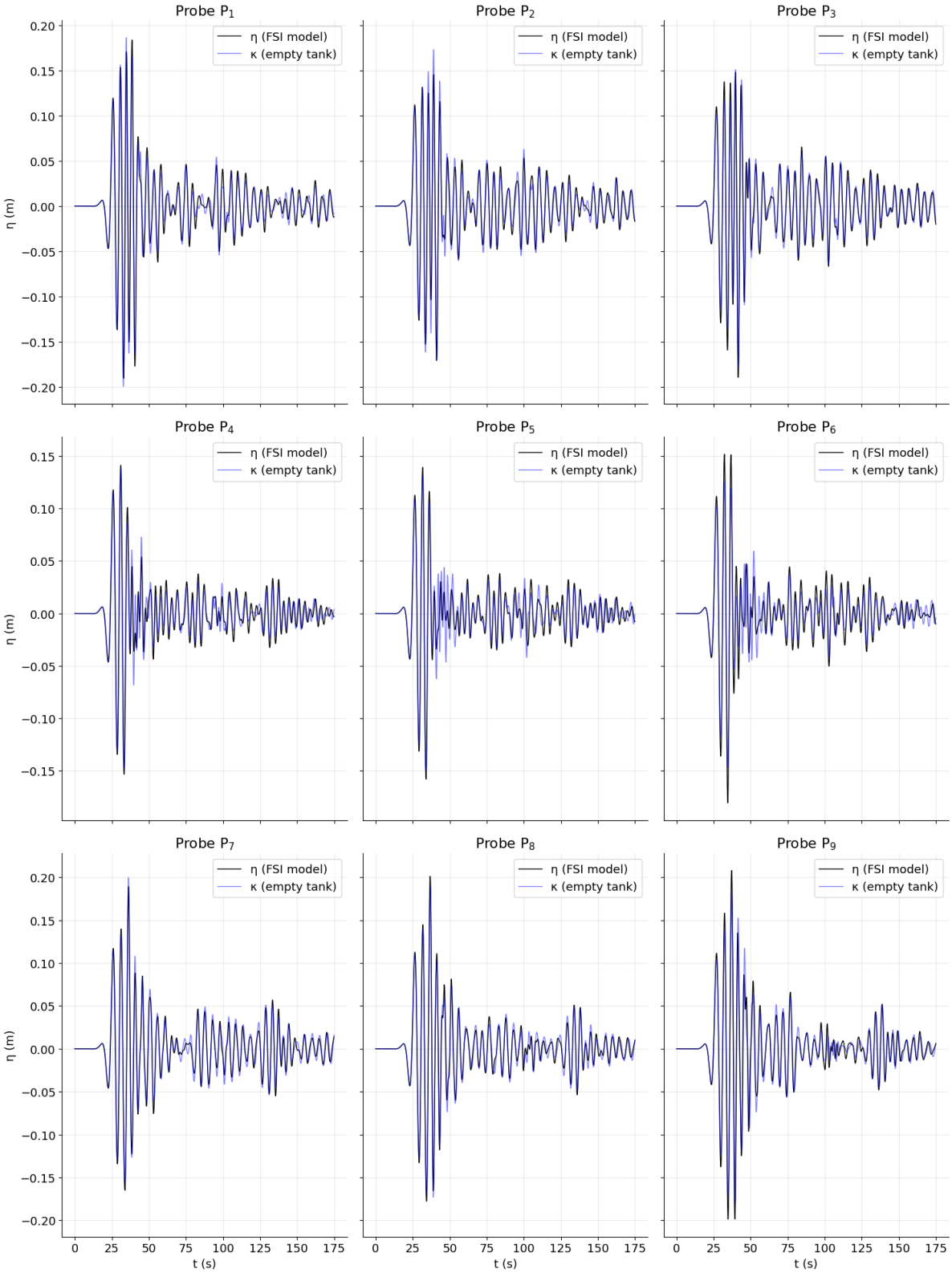

Figure C.4: Time-series hydroelastic response membrane measured at probes $P_1 - P_9$ for depth-Froude number $Fr_d = 0.9$.

C.5. Hydroelastic response with depth-Froude number 1.0

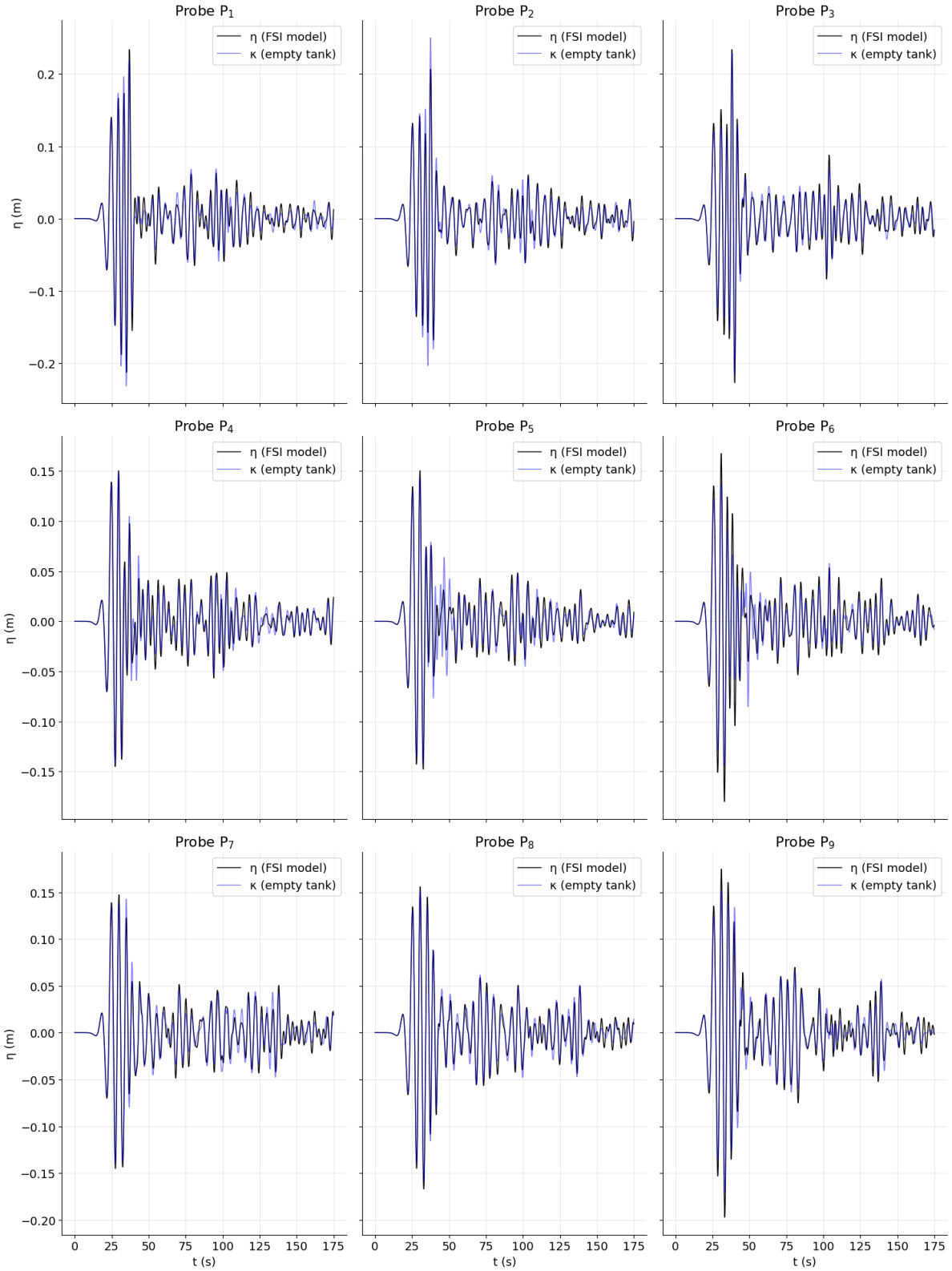

Figure C.5: Time-series hydroelastic response membrane measured at probes $P_1 - P_9$ for depth-Froude number $Fr_d = 1.0$.

C.6. Hydroelastic response with depth-Froude number 1.1

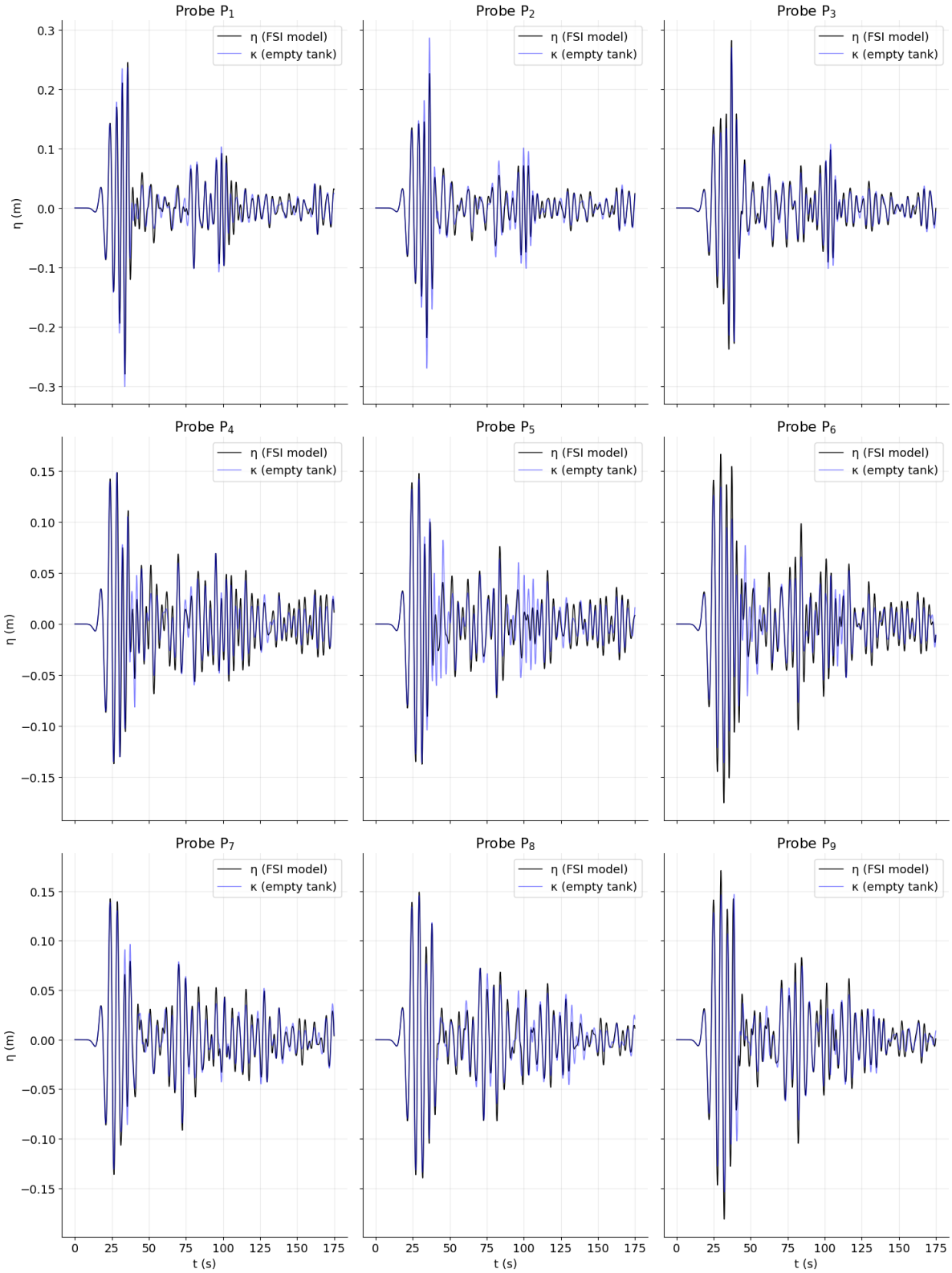

Figure C.6: Time-series hydroelastic response membrane measured at probes $P_1 - P_9$ for depth-Froude number $Fr_d = 1.1$.

C.7. Hydroelastic response with depth-Froude number 1.2

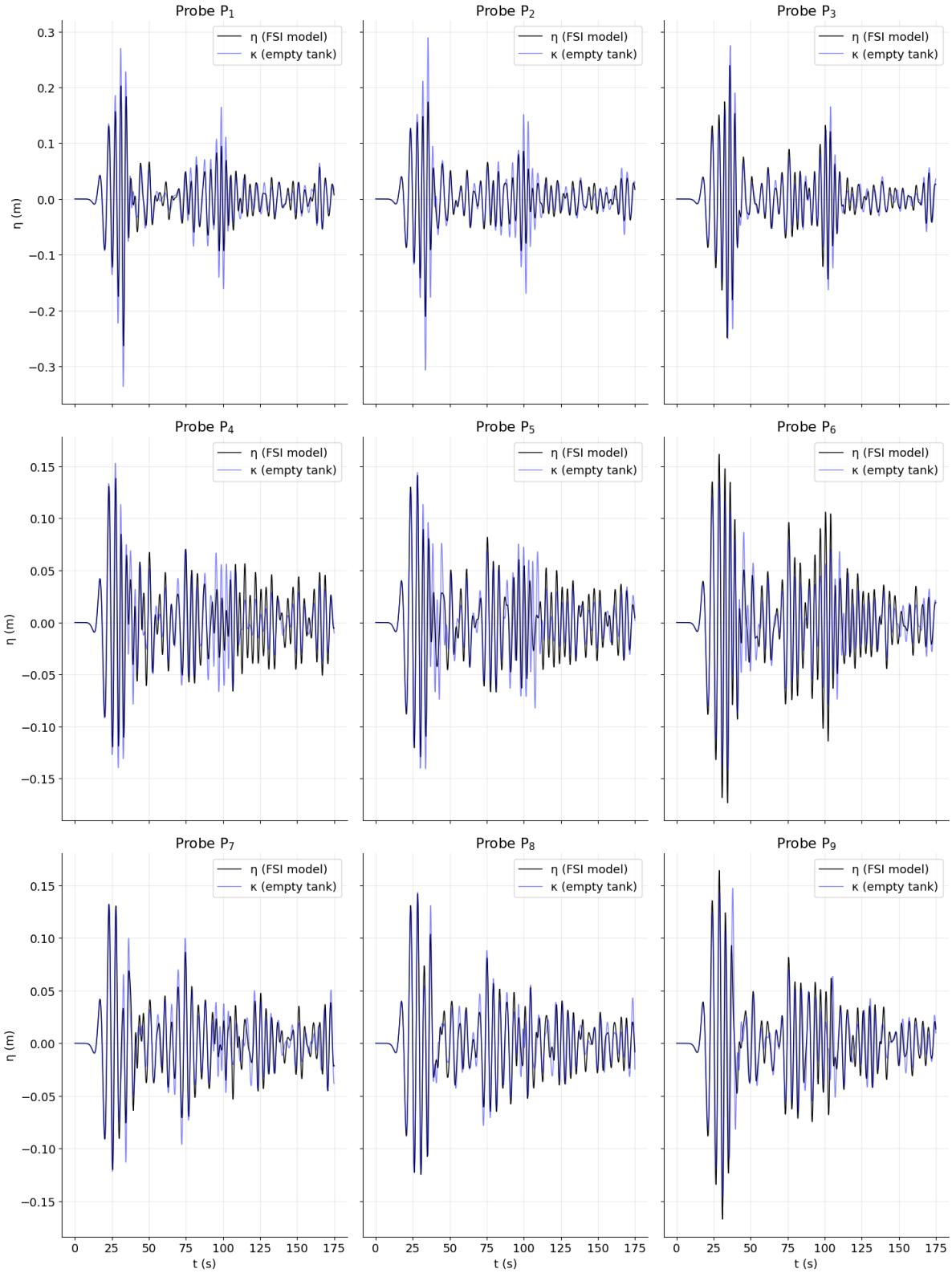

Figure C.7: Time-series hydroelastic response membrane measured at probes $P_1 - P_9$ for depth-Froude number $Fr_d = 1.2$.

C.8. Hydroelastic response with depth-Froude number 1.3

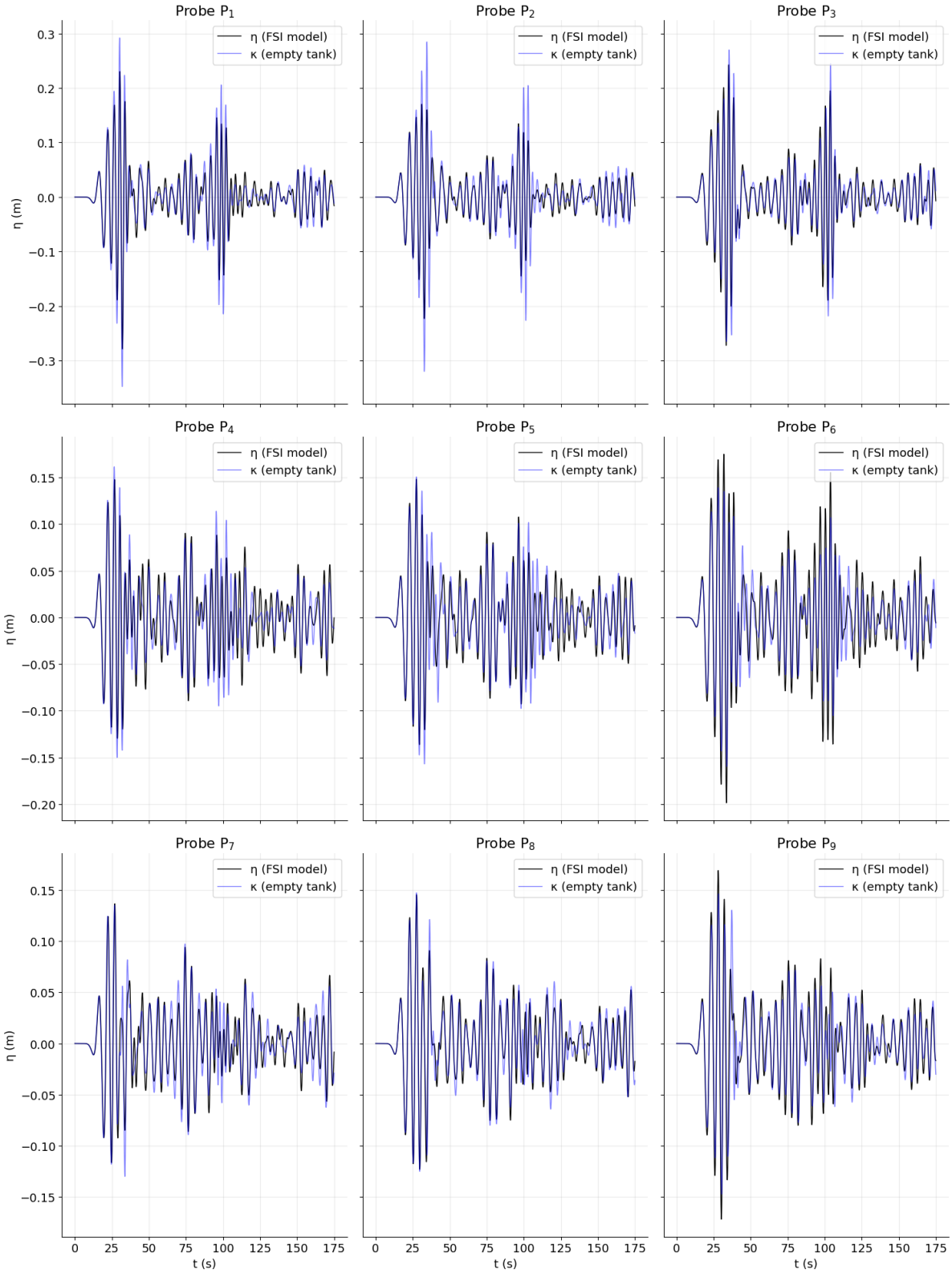

Figure C.8: Time-series hydroelastic response membrane measured at probes $P_1 - P_9$ for depth-Froude number $Fr_d = 1.3$.

C.9. Hydroelastic response with depth-Froude number 1.4

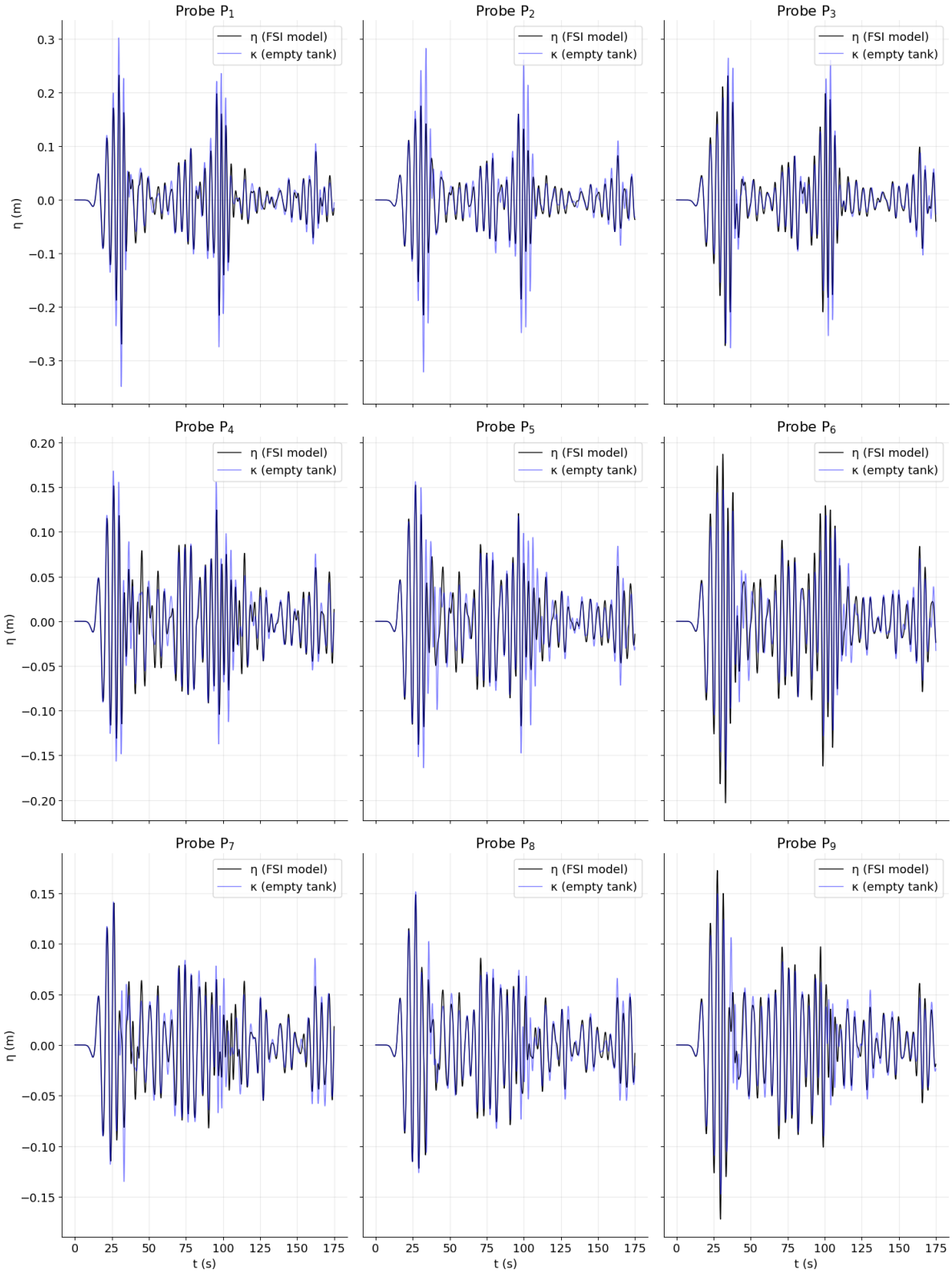

Figure C.9: Time-series hydroelastic response membrane measured at probes $P_1 - P_9$ for depth-Froude number $Fr_d = 1.4$.

References

[1] Delft High Performance Computing Centre (DHPC). *DelftBlue Supercomputer (Phase 2)*. https://www.tudelft.nl/dhpc/ark:/44463/DelftBluePhase2. 2024.

[2] "A new form of the Boussinesq equations with improved linear dispersion characteristics". In: *Coastal Engineering* 15.4 (1991), pp. 371–388. ISSN: 0378-3839. DOI: https://doi.org/10.1016/0378-3839(91)90017-B.

[3] S. Agarwal et al. "Waves in waterways generated by moving pressure field in Boussinesq equations using unstructured finite element model". In: *Ocean Engineering* 262 (2022), p. 112202. ISSN: 0029-8018. DOI: https://doi.org/10.1016/j.oceaneng.2022.112202.

[4] Shagun Agarwal, Oriol Colomés, and Andrei Metrikine. "Dynamic Analysis of Viscoelastic Floating Membranes Using Monolithic Finite Element Method". In: *Journal of Fluids and Structures* (Jan. 2024). DOI: 10.2139/ssrn.4689746.

[5] Shagun Agarwal, V. Sriram, and K. Murali. "Three-dimensional coupling between Boussinesq (FEM) and Navier–Stokes (particle based) models for wave structure interaction". In: *Ocean Engineering* 263 (2022), p. 112426. ISSN: 0029-8018. DOI: https://doi.org/10.1016/j.oceaneng.2022.112426.

[6] I. Akkerman, J.H.A. Meijer, and M.F.P. ten Eikelder. "Isogeometric analysis of linear free-surface potential flow". In: *Ocean Engineering* 201 (2020), p. 107114. ISSN: 0029-8018. DOI: https://doi.org/10.1016/j.oceaneng.2020.107114.

[7] Alexey Andrianov. "Hydroelastic analysis of VLFS". In: *Repository TU Delft (PhD thesis)* (2005).

[8] Santiago Badia and Francesc Verdugo. "Gridap: An extensible Finite Element toolbox in Julia". In: *Journal of Open Source Software* 5.52 (2020), p. 2520. DOI: 10.21105/joss.02520.

[9] D. Bayraktar Ersan and S. Beji. "Numerical simulation of waves generated by a moving pressure field". In: *Ocean Engineering* 59 (2013), pp. 231–239. ISSN: 0029-8018. DOI: https://doi.org/10.1016/j.oceaneng.2012.12.025.

[10] Jeff Bezanson et al. "Julia: A Fresh Approach to Numerical Computing". In: *SIAM Review* 59.1 (2017), pp. 65–98. DOI: 10.1137/141000671.

[11] J. Bosboom et al. "Wave Kinematics Computations Using Boussinesq Models". In: (), pp. 109–122. DOI: 10.1061/9780784402429.009.

[12] Maurizio Brocchini. "A reasoned overview on Boussinesq-type models: The interplay between physics, mathematics and numerics". In: *Proceedings. Mathematical, physical, and engineering sciences / the Royal Society* 469 (Dec. 2013), p. 20130496. DOI: 10.1098/rspa.2013.0496.

[13] Mainak Chakraborty, V. Sriram, and K. Murali. "Field measurement and analysis of ship generated waves in Hooghly river, India". In: *Applied Ocean Research* 128 (2022), p. 103337. ISSN: 0141-1187. DOI: https://doi.org/10.1016/j.apor.2022.103337.

[14] Oriol Colomés, Francesc Verdugo, and Ido Akkerman. "A monolithic Finite Element formulation for the hydroelastic analysis of Very Large Floating Structures". In: *International Journal for Numerical Methods in Engineering* 124 (Oct. 2022). DOI: 10.1002/nme.7144.

[15] Tatyana Dyakonova and Alexander Khoperskov. "Bottom friction models for shallow water equations: Manning's roughness coefficient and small-scale bottom heterogeneity". In: *Journal of Physics: Conference Series* 973.1 (Mar. 2018). DOI: 10.1088/1742-6596/973/1/012032.

[16] Palaneeswaran Ekambaram and C. Tam. "Sustainable Land Reclamations From Sea". In: Nov. 2007, (). 4th World Project Management Week on Project Management: Driving Growth, Creating Equality.

[17] G. Engel et al. “Continuous/discontinuous finite element approximations of fourth-order elliptic problems in structural and continuum mechanics with applications to thin beams and plates, and strain gradient elasticity”. In: *Computer Methods in Applied Mechanics and Engineering* 191.34 (2002). ISSN: 0045-7825. DOI: https://doi.org/10.1016/S0045-7825(02)00286-4.

[18] R. Ertekin, William Webster, and J. Wehausen. “Waves caused by a moving disturbance in a shallow channel of finite width”. In: *Journal of Fluid Mechanics* 169 (Aug. 1986), pp. 275–292. DOI: 10.1017/S0022112086000630.

[19] *Front Matter*. John Wiley & Sons, Ltd, 2013, pp. i–xix. ISBN: 9781118483565. DOI: https://doi.org/10.1002/9781118483565.fmatter.

[20] T. H. Havelock. “The Propagation of Groups of Waves in Dispersive Media, with Application to Waves on Water Produced by a Travelling Disturbance”. In: *Proceedings of the Royal Society of London. Series A, Containing Papers of a Mathematical and Physical Character* 81.549 (1908), pp. 398–430. ISSN: 09501207. URL: http://www.jstor.org/stable/93014.

[21] Leo Holthuijsen. “Waves in Oceanic and Coastal Waters”. In: *Waves in Oceanic and Coastal Waters, by Leo H. Holthuijsen, pp. 404. Cambridge University Press, January 2007. ISBN-10: . ISBN-13:* (). DOI: 10.2277/0521860288.

[22] Min Woo Kim, Weoncheol Koo, and Sa Young Hong. “Numerical analysis of various artificial damping schemes in a three-dimensional numerical wave tank”. In: *Ocean Engineering* 75 (2014), pp. 165–173. ISSN: 0029-8018. DOI: https://doi.org/10.1016/j.oceaneng.2013.10.012.

[23] G. Manoj Kumar and V. Sriram. “Development of a hybrid model based on mesh and meshfree methods and its application to fluid–elastic structure interaction for free surface waves”. In: *Journal of Fluids and Structures* 99 (2020), p. 103159. ISSN: 0889-9746. DOI: https://doi.org/10.1016/j.jfluidstructs.2020.103159.

[24] Peter Lancaster and Kestutis Salkauskas. “Surfaces generated by moving least squares methods”. In: *Mathematics of Computation* 37 (1981), pp. 141–158. URL: https://api.semanticscholar.org/CorpusID:28401633.

[25] P.A. Madsen and O.R. Sørensen. “A new form of the Boussinesq equations with improved linear dispersion characteristics. Part 2. A slowly-varying bathymetry”. In: *Coastal Engineering* 18.3 (1992). ISSN: 0378-3839. DOI: https://doi.org/10.1016/0378-3839(92)90019-Q.

[26] P.A. Madsen and O.R. Sørensen. “Bound waves and triad interactions in shallow water”. In: *Ocean Engineering* 20.4 (1993), pp. 359–388. ISSN: 0029-8018. DOI: https://doi.org/10.1016/0029-8018(93)90002-Y.

[27] Muthukumar Narayanaswamy. “SPHysics-FUNWAVE hybrid model for coastal wave propagation”. In: *Journal of Hydraulic Research - J HYDRAUL RES* 48 (). DOI: 10.3826/jhr.2010.0007.

[28] United Nations. “Policies on spatial distribution and urbanization have broad impacts on sustainable development”. In: *Population Facts - Department of Economic and Social Affairs* (2020).

[29] Nathan Mortimore Newmark. “A Method of Computation for Structural Dynamics”. In: *Transactions of the American Society of Civil Engineers* (1959). URL: https://api.semanticscholar.org/CorpusID:63410335.

[30] D. H. Peregrine. “Long waves on a beach”. In: *Journal of Fluid Mechanics* 27.4 (1967), pp. 815–827. DOI: 10.1017/S0022112067002605.

[31] Ole R. Sørensen, Hemming A. Schäffer, and Lars S. Sørensen. “Boussinesq-type modelling using an unstructured finite element technique”. In: *Coastal Engineering* 50.4 (2004), pp. 181–198. ISSN: 0378-3839. DOI: https://doi.org/10.1016/j.coastaleng.2003.10.005.

[32] V. Sriram, Q.W. Ma, and T. Schlurmann. “A hybrid method for modelling two dimensional non-breaking and breaking waves”. In: *Journal of Computational Physics* 272 (2014), pp. 429–454. ISSN: 0021-9991. DOI: https://doi.org/10.1016/j.jcp.2014.04.030.

[33] Hideyuki Suzuki. “Overview of Megafloat: Concept, design criteria, analysis, and design”. In: *Marine Structures* 18.2 (2005). Very Large Floating Structures, pp. 111–132. ISSN: 0951-8339. DOI: https://doi.org/10.1016/j.marstruc.2005.07.006.

[34] C.M. Wang and Z.Y. Tay. “Very Large Floating Structures: Applications, Research and Development”. In: *Procedia Engineering* 14 (2011). The Proceedings of the Twelfth East Asia-Pacific Conference on Structural Engineering and Construction, pp. 62–72. ISSN: 1877-7058. DOI: https://doi.org/10.1016/j.proeng.2011.07.007.

[35] Jiakun Wang et al. “Application of facet scattering model in SAR imaging of sea surface waves with Kelvin wake”. In: *Progress In Electromagnetics Research B* 67 (Jan. 2016), pp. 107–120. DOI: 10.2528/PIERB16022804.

[36] Min Zhang and Sebastian Schreier. “Review of wave interaction with continuous flexible floating structures”. In: *Ocean Engineering* 264 (2022), p. 112404. ISSN: 0029-8018. DOI: https://doi.org/10.1016/j.oceaneng.2022.112404.